Building thermal modelling using electric circuit simulation

Author:
Parnis, Gerald

Publication Date:
2012

DOI:

License:

Building Thermal Modelling
Using Electric Circuit Simulation

Gerald Parnis

School of Photovoltaic and Renewable Energy Engineering
University of New South Wales
Sydney, Australia

Master of Engineering by Research
July 2012

ORIGINALITY STATEMENT

I hereby declare that this submission is my own work and to the best of my knowledge it contains no materials previously published or written by another person, or substantial proportions of material which have been accepted for the award of any other degree or diploma at UNSW or any other educational institution, except where due acknowledgement is made in the thesis. Any contribution made to the research by others, with whom I have worked at UNSW or elsewhere, is explicitly acknowledged in the thesis. I also declare that the intellectual content of this thesis is the product of my own work, except to the extent that assistance from others in the project's design and conception or in style, presentation and linguistic expression is acknowledged.

Abstract

This thesis presents a novel approach to building thermal modelling using electric circuits, which is flexible, accurate and transparent. The theoretical framework underpinning this methodology is the analogy between thermal quantities and electrical quantities: the *Electrical Analogy*. Building construction properties and climate data are mapped into electrical components from which a thermal circuit is assembled. The thermal circuit diagram is entered into an electric circuit simulator program, where time and frequency domain simulations are run with the results interpreted in terms of thermal quantities and energy. As a result, the circuit solution or the manipulation and solution of corresponding differential equations are not required; the circuit simulator produces simulation results directly from the thermal circuit.

The thermal modelling of a low energy house is presented in this thesis to illustrate this approach. An existing model implemented in a commercial building simulation program is replicated as a circuit model. The indoor air temperature sequences generated by the two models are compared. For a second modelling comparison, a simple manual model is applied to the low energy house. This manual model consists of equations for calculating estimates of average temperatures, heating and cooling loads and the building time constant. The circuit model computations are compared to these manual calculations.

An algorithm for judging the accuracy of representing a construction layer as an n-length RC ladder in a circuit model is provided as an aid for choosing n for layer representations when assembling a circuit model. Additionally, a procedure for lumping multiple orientations of the building envelope (of equivalent construction) including orientation-specific irradiance sequences into a single *lumped wall* and single irradiance sequence is given. This procedure can significantly simplify a thermal circuit while providing equivalent modelling accuracy to the corresponding unlumped circuit.

The building time constant is discussed in terms of circuit model-based estimations and its characterization of thermal inertia. Finally, the affinity of this modelling methodology with Building Physics is highlighted throughout the thesis. In addition to producing accurate simulation results, this modelling methodology has educational possibilities in terms of elucidating and teaching Building Physics.

Acknowledgements

Nomenclature

The following tables contain symbols used in Chapters 3-6.

Symbol	Description	Units
A	Area	m^2
A_{s_x}	Area of surface type s at orientation x	m^2
A_w, A_{s_total}	Total glazing area, Total area of surface type s	m^2
ach	Infiltration/Ventilation rate (air changes per hour)	
c	Specific heat	$J/kg \cdot ^{\circ}C$
c_p	Constant pressure specific heat of air	$J/kg \cdot ^{\circ}C$
C	Thermal capacitance	$J/^{\circ}C$
C_T	Total lumped (apparent) thermal capacitance	$J/^{\circ}C$
C_{eff}	Effective thermal capacitance	$J/^{\circ}C$
$Cv(RMSE)$	Coefficient of variation of the root-mean-square error	
f	Frequency	h^{-1}
f_B	Corner frequency	h^{-1}
f_{s_x}	Fraction of total area of surface type s at orientation x	
$F_{i\text{-}j}$	View factor: from i to surface j	
$G_{incident}$	Incident irradiance averaged across all glazing	W/m^2
$G_{incident,x}$	Irradiance at orientation x	W/m^2
$G_{incident,Lumped\_s}$	Cumulative lumped irradiance on surface type s	W/m^2
h_{wind_x}	Wind-based convection coefficient at orientation x	W/m^2
h_{conv_s}	Lumped wind-based convection coefficient for surface type s	W/m^2
$h_{gnd\_}$	Ground radiative heat transfer coefficient	W/m^2
$h_{sky\_}$	Sky radiative heat transfer coefficient	W/m^2
$|H(f)|$	Magnitude transfer function	
k	Thermal conductivity	$W/m \cdot ^{\circ}C$
MBE	Mean Bias Error	
n	Order of RC ladder. Number of resistor, capacitor pairs.	
P	Period	h
$\dot{q}_{solar,\,gain\_x}$	Solar gain flux due to glazing at orientation x	W/m^2
$\dot{q}_{solar,\,gain\_lump}$	Cummulative solar gain flux due to all glazing	W/m^2
$\dot{Q}_{solar,\,gain}$	Cummulative solar gain due to all glazing	W
$\dot{Q}_{solar\_absorb\_s}$	Cummulative radiant flux absorbed by surface type s	W
$Q_{heating}$	Heating load	kWh
$Q_{cooling}$	Cooling load	kWh
R	Thermal resistance	$^{\circ}C/W$
R_T	Net thermal resistance between indoors and outdoors	$^{\circ}C/W$
sM	Specific Mass	kg/m^2
$SHGC$	Solar Heat Gain Coefficient	
t	time	s, h
T	Temperature	$^{\circ}C \; or ^{\circ}K$
V	Voltage	V
Vol	Air volume	m^3
x	Construction layer thickness	m

Greek Letters	Description	Units
α	Absorptivity	
$\mathit{\Delta}$	Difference	
ε	Emissivity	
ρ	Air density	kg/m^3
σ	Stefan-Boltzmann constant	$W/m^2 \cdot K^4$
τ	Building/Circuit time constant	h
θ	Outer surface tilt: angle to horizontal	$^\circ$

Subscripts	Description
d	Daily
dp	Dew point (temperature)
g	Glazing
gnd	Ground
h	Hours
i	Construction layer
in	Indoor
s	Seconds
si	Inner surface
sip	Structural Insulated Panels
so	Outer surface
t	Total Resistance or Capacitance of an RC ladder
T	Total lumped (net) Resistance or Capacitance of a house
wf	Window frames
$windows$	Both window frames and glazing
y	Yearly
N	North
E	East
S	South
W	West
H	Horizontal

Contents

1 Introduction

According to Amory Lovins [1]:

> *"Buildings (excluding industrial processes inside) use 69% of U.S. electricity, 36% of direct natural gas, 40% of all energy (as of 2005)"*

> *"Buildings emit 38% of fossil-fuel CO2 (60% in UK)"*

> *"Buildings have the slowest turnover of any major kind of capital stock: often 50–100 yr"*

A more recent statement taken from a report by The Royal Academy of Engineering, UK [2] includes a lower, yet still very significant estimate of carbon emissions attributed to buildings in the UK:

> *"The UK goal now is to achieve 80% reduction in carbon emissions by 2050. Yet buildings presently account for some 45% of carbon emissions and it has been estimated that 80% of the buildings that we will be occupying in 2050 have already been built."*

The Centre for International Economics (CIE) reported lower figures for Australia in 2007: commercial and residential buildings together accounted for 19% of Australian energy consumption and 23% greenhouse gas (GHG) emissions [3]. The Australian Academy of Science (AAS), who endorse the latest IPCC 4th assessment report on climate change, have emphasized the importance of energy efficiency both in new building construction and for retrofitting efficiency measures to existing building stock [4]. The AAS points out that most of old building stock has an effective zero star energy efficiency rating and that 40% of Australian homes currently have no ceiling insulation [4]. Retrofitting insulation into existing uninsulated homes would result in significant savings to householders, abatement of 2.4 million tonnes of GHG per annum, reduced electricity prices through delayed infrastructure spending and increase in GDP of $894 million over 2008-30 [4]. The AAS also suggest a more aggressive national energy standard for new buildings: 7 star by 2015 and 9 star by 2020 [4]. Presumably this is partially motivated by the recent trend of building larger (air-conditioned) homes, predicted to continue to grow in the future, contributing to increasing domestic building energy consumption [5].

Add the issues of energy security, population growth and quality of life, to the economic and environment costs (including pollution) of energy production, distribution and consumption and it becomes apparent that energy consumption significantly impacts everyone. Despite these significant impacts, the use of energy tends to be taken for granted or largely ignored in our daily lives. This lack of awareness of energy consumption and its impacts, in addition to the abundant supply of relatively cheap energy in the past, has meant that the building

design has not taken into account energy consumption and performance. Building design is changing in this regard (albeit at a slow pace), with governments invoking mandatory performance targets and other incentives to motivate energy efficiency in building design [2, 4-6]. Part of this change is the need to incorporate *Building Engineering Physics* into building design, construction and maintenance [2]. The Royal Academy of Engineering, UK give the following definition and motivation for Building Engineering Physics [2]:

> *"Building engineering physics is a relatively new scientific discipline which investigates the areas of natural science that relate to the performance of buildings and their indoor and outdoor environments. The field deals principally with the flows of energy, both natural and artificial, within and through buildings."*

> *"Building engineering physics comprises a unique mix of heat and mass transfer physics, materials science, meteorology, construction technology and human physiology necessary to solve problems in designing high performance buildings."*

> *"The need for professionals in the construction industry to be well versed in building engineering physics has never been higher with the global concerns to address the sustainability of the built environment."*

The second of the above quotes emphasizes the multi-disciplinary nature of Building Engineering Physics (herein *Building Physics*), suggesting that it impinges on the domains of *all* persons involved in the building industry: planners, architects, builders, engineers and owners. As such, it is prudent that all professionals have varying degrees of exposure and awareness of Building Physics.

In this thesis, a building thermal modelling methodology is presented that encourages an understanding of Building Physics. The method is robust, flexible and transparent. Using this methodology requires a minimum knowledge of electric circuits (e.g. Ohm's Law) while the *Electrical Analogy* provides a framework for understanding Building Physics. The methodology employs a commercial electric circuit solving program (*Micro-Cap*) that includes the thermal circuit diagram as the user interface from which thermal simulations are directly executed. The thermal circuit diagram is an intuitive and simple interface for model construction and it is commonly used in thermal research for illustrating properties such as heat flow paths.

The user has complete control over the complexity and detail of a building model. A simple building model can be initially assembled at an early design stage with course simulation results generated. At a later time, more detail and complexity may be added to the model enabling finer simulation results to be produced. Unlike other building simulation packages,

this methodology is data driven: there is no programming language to learn. Climate and construction property data are entered as electrical component values for circuit components such as resistors and capacitors. While manipulating or assembling the thermal circuit, the user manipulates thermal quantities such as thermal resistances or thermal capacitances. This proximity to physical thermal quantities re-enforces Building Physics concepts and relationships during building model manipulation.

Briefly, the research aims of this thesis are:

(i) to investigate the utility of using RC circuits and a commercial circuit solving program for building thermal modelling.

(ii) to show the accuracy, flexibility and transparency of this modelling methodology.

(iii) to show the affinity this methodology has with Building Physics thus highlighting its educational potential.

SPICE (Simulation Program with Integrated Circuit Emphasis)
Although this methodology does not require the *use* of programming language, a programming language forms the basis of the simulation engine utilized when executing thermal simulations. *SPICE* [7] is an electric circuit simulator engine that includes a textual specification (language) of how electric circuit components are input to the engine to run a simulation. Micro-Cap [8] is one of many commercial electric circuit simulator programs that provide a high level user-interface for specifying electric circuit models in terms of screen icons of electric circuit components (e.g. a resistor). In this thesis, Micro-Cap is used to construct electric circuits modelling houses from which circuit simulations are run to obtain thermal simulation results. For much of this thesis, the mention of Micro-Cap when discussing electric circuit simulation or building model simulation is arbitrary: *any* implementation of SPICE could run the circuit simulations and produce the results presented in this thesis. Some parts of the descriptions of thermal models implemented as electric circuits using Micro-Cap are specific to the Micro-Cap circuit simulator program: for example, user-defined current sources in section *4.3.6.*

Thesis Overview
In Chapter 2, a brief summary of the history of building thermal analysis, including the early use of the Electrical Analogy predating digital computers, is presented. A review is then given of the dominant modelling techniques that are currently used in building simulation programs as well as techniques that are common in research domains. The building time constant is a modelling computation that is investigated in this thesis and in this chapter its treatment in the literature is discussed. A suitable modelling representation for the sky and ground temperatures and solar radiation was required and the models chosen from the literature are described.

In Chapter 3, the modelling methodology in this thesis is described and compared to the techniques presented in Ch. 2. This includes examples of how thermal quantities are represented as electrical circuit components and how a wall layer is represented in a thermal circuit. The affinity of this methodology with Building Physics is discussed. The electrical circuit time constant is described and the technique for computing it is given as a means of computing the building time constant from a thermal circuit model of a building.

The modelling methodology in this thesis is described in detail in Chapter 4 in the context of the modelling example discussed throughout the balance of the thesis. The transient thermal model of a low energy house as implemented in a commercial building simulation program (IDA ICE: Indoor Climate and Energy) is replicated as a circuit model. The assembly of the circuit model is described in detail. Simulation results (indoor temperature sequences) of these two transient models are compared and presented with the aim of validating the circuit model. A description of how ventilation and heating/cooling are modelled using an electric circuit in Micro-Cap is given.

In Chapter 5 more detailed simulation results for the circuit model of the low energy house are presented. The necessity to mimic the original IDA model is removed and the ground temperature and sky temperature representations of the circuit model are changed to new representations previously described in Ch. 2. Three types of simulation results are presented: (i) monthly average indoor temperatures, (ii) heating/cooling load computations and (iii) building time constant and frequency response. These computations are made for the circuit model with parametric variations: with and without solar input, varying the sky temperature, varying the thermal mass and varying the infiltration rate. Circuit model results are interpreted in terms of the thermal performance of the low energy house and observations concerning the building time constant in relation to thermal inertia are made.

In Chapter 6, a simple model for making manual thermal calculations is presented and applied to the low energy house. This steady-state model is developed from fundamental physical principles in equation form. Although the Manual model makes simplifications and has limitations, its physical grounding and transparency provides a good basis for comparison between the simulation results of the circuit and Manual models. This comparison suppliments the circuit modelling validation of Chapter 4. The circuit model of Ch. 5 is modified to reflect the simplifications of the Manual model of the low energy house. Most of the simulation computations of Ch. 5 are repeated using these two new models, with the results presented and compared.

2 Literature Review

2.1 Modelling Methodologies

Building thermal analysis has a lengthy history: the Fourier Continuity Equation (Eqn. 2) first appeared in 1822 while some basic energy concepts date back over 200 years [9]. The wall transmittance or *U-value* (W/m^2.°C), the outward steady-state heat flux ("flow") (W/m^2) per degree of temperature difference across a wall, was first presented in 1868 [10]. Shavit [11] documented a history of building analysis and simulation over the previous 100 years (from publication: 1995) that included many thermal studies and new concepts dating before 1940. These include: an early description of the heat transfer coefficient of building material (1908), the first attempt to define time constants of rooms and buildings (1912), a study that included the measurement and comparison of heat gains and losses through various elements of a building (1932), and a study quantifying a building cooling load that included the use of "the concept of *time lag*" (1935).

Shavit cites a paper by Paschkis [12] in 1942 as the first publication describing how the electrical analogy could be used to analyse and quantify thermal behavior in buildings. Modelling using the electrical analogy involves mapping construction properties and climate data into electrical component values and interpreting electrical modelling results in terms of building properties, energy, and climate. Shown in Table 2.1 below, the analogy between thermal and electrical quantities, is the basis from which a thermal circuit is constructed using electrical component values. Shavit lists many studies during the 1950s and early 1960s that used electric circuit representations (thermal circuits) to model thermal properties of phenomena such as walls, enclosures and heat pump processes [11].

Thermal			Electrical		
Temperature	T	$°C$	Voltage	V	V
Heat Transfer Rate	$\dot{Q}$	W	Current	I	A
Thermal Resistance	R	$°C/W$	Electrical Resistance	R	Ω
Thermal Capacitance	C	$J/°C$	Electrical Capacitance	C	F
Steady Heat Conduction $\dot{Q} = kA\dfrac{\Delta T}{x} = \dfrac{\Delta T}{R}$			Ohm's Law		$I = \dfrac{\Delta V}{R}$
Thermal Capacitance Heat Flow Rate		$\dot{Q} = C\dfrac{dT}{dt}$	Current through Capacitor		$I = C\dfrac{dV}{dt}$
Heat Balance			Kirchhoff's Current Law		

Table 2.1: Thermal-Electrical Analogy; Quantities, Symbols and Typical Units Are Shown [9, 13-15]

Circuit diagrams were either solved (i) using electric circuit analysis techniques involving mathematics and simple "calculating-machine solutions" or (ii) by implementing the circuit diagram as an actual electrical circuit ("analogues" or analog computer) [16, 17]. Correspondingly, voltage and current values at circuit nodes were either (i) calculated/computed or (ii) measured. These nodal values were then mapped to thermal equivalent quantities allowing the user to deduce thermal qualities of the modelled

phenomena [16, 17]. In the discussion following Nottage and Parmalee's paper [16], Achenbach raised an important point that is relevant today:

> *"Analogue solutions have an important advantage particularly for those who are not mathematically inclined in that it is not even necessary to write the circuit equations, let alone solve them, when using an analogue of this kind. The results come out as direct physical measurements."*

In the 1960s, analog computers were superseded by the advent of digital computers allowing users to specify and solve the governing heat balance equations when modelling thermal dynamics. Compared to analog computers at this time, early digital computers required much more time to solve comprehensive thermal analysis problems [11]. This motivated research into building thermal analysis techniques that are computationally efficient and suitable for use in conjunction with limited digital computing power.

Today, researchers commonly present a thermal circuit diagram mostly comprised of symbols that are similar to electric circuit symbols as a starting point of a model description from which heat balance equations are derived, based on electric circuit principles such as Kirchhoff's Current Law [15, 18]. The heat balance equations are then either solved analytically (if possible) as is commonly the case for simplified *Lumped Model* techniques [18, 19] or computed solutions are derived using techniques such as *Finite Difference Methods* or *Response Function Methods* [20, 21]. These latter techniques are the theoretical basis of commercial or public domain building simulation programs [15, 20, 22] and were developed when common computing power was as limiting factor, necessitating the use of algorithms that are computationally economical [21] [23]. The response function method is sometimes presented as two distinct methods: *Time* Domain Methods *(Response Factors, Conduction Transfer Functions*) and *Frequency* Domain Methods (*Periodic Response Factors*, the *Admittance* Method) [24] [20] and this is done in the sections that follow.

Descriptions of these techniques often begin with the physical laws that govern one dimensional heat conduction through a single (homogenous) layer wall shown in Eqns. 1 and 2 below [15, 20, 25, 26].

$$\dot{Q}_{conduction}(x,t) = -kA\frac{dT}{dx} \qquad (1)$$

Eqn. 1 is *Fourier's law of heat conduction* [13] where $\dot{Q}_{conduction}(x,t)$ is the rate of heat transfer (W) at depth x (m) at time t (seconds), k is the *constant* thermal conductivity of the wall material (W/m.°C), A is the area of the wall (m^2) and $T(x,t)$ is the temperature at wall depth x metres at time t seconds. At steady state, the rate of conductive heat transfer is constant throughout the wall and can be calculated from the difference in temperature *(ΔT)* and

depth *(Δx)* between any two depth positions in the wall, for example the inner and outer wall surfaces.

Eqn. 2 is the one-dimensional heat conduction equation [13] (also referred to as the "Fourier Equation" [20, 27] or the "Fourier Continuity Equation" [15, 24]), where α is the thermal diffusivity of the wall (m²/s), a measure of how quickly heat spreads through the wall construction material.

$$\frac{\partial^2 T}{\partial x^2} = \frac{1}{\alpha}\frac{\partial T}{\partial t} \qquad\qquad \text{Steady State Solution: } T(x) = ax + b \qquad (2)$$

Here, *a* and *b* have no significance other than to indicate that at steady-state, the temperature of the wall varies linearly with depth only, between the two surface temperatures. Cengel [13] derives Eqn. 2 from Eqn. 1 using basic calculus and a heat-balance argument applied to a thin slice of a single layer wall.

Exact (analytic) solutions to Eqns. 1 and 2 are possible for a single layer wall with simple boundary conditions such as: the outdoor temperature is assumed to be either increasing linearly or a purely sinusoidal of one frequency [28]. Disregarding the limitations of these conditions, Iu and Fisher [25] point out that once multi-layer wall constructions are considered then numerical methods are required.

Each of the four mentioned methods (Response Function: Time and Frequency Domains, Finite Difference Method, Lumped Models) provide solutions to Eqns. 1 and 2 that governing the conductive heat flow through a building envelope and these methods are briefly described in the sections that follow.

Both the time domain and frequency domain versions of the Response Functions methods require many mathematical manipulation of Eqns. 1 and 2 before the response functions are generated. The following cursory description is based on the presentations by many authors [15, 20, 26, 29] and illustrates the complexity of these solutions techniques. A Laplace Transform is applied to Eqns. 1 and 2 and the relationship between temperature and heat flow at the inner surface of a single layer is expressed in terms of the temperature and heat flow at the outer surface in the form of a *transmission matrix* (Appendix A contains an example). This is then generalized for a multi-layer wall by multiplying consecutive transmission matrices corresponding to each layer. The resulting matrix is then rearranged to produce a matrix-based system of equations describing the *heat flows at both surfaces* in terms of *both surface temperatures*, in the Laplace domain as shown below in Equation 3:

$$\begin{bmatrix} \dot{Q}_1(0,s) \\ \dot{Q}_n(L,s) \end{bmatrix} = \begin{bmatrix} -A(s)/B(s) & 1/B(s) \\ -1/B(s) & D(s)/B(s) \end{bmatrix} \begin{bmatrix} T_1(0,s) \\ T_n(L,s) \end{bmatrix} \qquad (3)$$

The symbol s indicates time *(t)* transformed into the Laplace domain while $\dot{Q}_1(0, s)$ is the heat flow at the *outer* surface of an *n*-layer wall, $\dot{Q}_n(L, s)$ is the heat flow at the *inner* surface and $T_1(0, s)$, $T_n(L, s)$ are the corresponding surface temperatures. The matrix elements are the *Transfer Functions* (also called "s-transfer functions" [30]) and these are "complicated transcendental hyperbolic functions" [15] which the *Time Domain* and *Frequency Domain* Methods approximate differently as briefly described below.

2.1.1 Time Domain Methods

The two principle methods of this category are (Thermal) Response Factors and Conduction Transfer Functions. Response Factors are time series of values at a surface of interest, which result from a unit impulse being applied to the opposite surface. For example, using Eqn. 3, the application of a triangular pulse of one degree temperature change (a mathematically convenient "unit excitation") at the outer surface results in a continuous response (curve) of the heat transfer rate at the inner surface of the multi-layer wall. The response is discretized into hourly values, forming a time series of values that are used as multipliers (coefficients) of an infinite series calculation based on the present and past surface temperature values at hourly intervals.

The original presentation of the Response Factors method [31] was later augmented with a further transformation (*z-transform*) [23] in order to improve (five-fold) the computation efficiency lacking in the original method due to the length of the Response Factors series [32]. This came to light when the Response Factors method was applied to multi-layered walls [23]. This improved technique is called the Conduction Transfer Function (CTF) method and is "widely" used in building simulation programs (BLAST, TRNSYS, EnergyPlus) [32] while DOE-2 and BLAST are examples of building simulation programs that are based on Response Factors [32].

Spitler and Fisher provide a succinct commentary on methods based on Response Factors and Conduction Transfer Functions *[33]*:

> *"Historically, they have been seen as a computationally feasible alternative to the heat balance approach, so called because it relies on a set of heat balances at each surface. Since both response factors and transfer functions are representations of an infinite series, they are necessarily approximations. They tend to differ in the number of excitation and response terms and in the nature of the excitation pulse. In general, there is a trade-off between the accuracy of the calculation and the computational requirements. In fact, many of the developments reported in the literature are aimed at improving the speed and/or accuracy of the calculation."*

> *"The CTF coefficients bear no obvious physical relationship to the wall thermal response."*

8

"Unlike the CTFs, the response factors do provide some insight into the steady periodic response to a steady periodic unit sol-air temperature pulse"

2.1.2 Frequency Domain Methods

Two methods from this category are Period Response Factors and the Admittance Method. The underlying assumption of these methods is that the time series (e.g. hourly) of the weather data (temperature, solar, etc) can be approximated as a limited number of terms from the Fourier series representation: a steady (constant) term and a finite sum of sinusoidal functions of various periods[20].

Typically the fundamental frequency of the Fourier series has a period of 24 h with other harmonics of the series having periods of 12 h, 6 h, etc and smaller, diminishing amplitudes [20]. The Admittance Method uses a Fourier series consisting of one sinusoidal function with a 24 h period for its representation of temperature and heat flows [10]. For the Periodic Response Factors (PRF) technique used in cooling load computations, the outdoor temperature and solar radiation are combined into a sol-air temperature assumed to be sinusoidal while the indoor temperature is constant [34]. The PRF values are obtained in two manners: using both Response Factors and CTFs [33] or using a procedure called Frequency Domain Regression (FDR) more recently presented by Chen and Wang [35]. Duska et al [34] made a cooling load calculation comparison using Thermal Response Factors (TRF), CTFs, PRFs from CTFs, PRFs from FDR and the Admittance Method. The resulting heat flux computations started out varying by approximately 0.75 W/m^2 while at the end of the 24 h cycle the variation was approximately 0.25 W/m^2. In his conclusion he stated:

"Coefficients for the TRF, CTF and PRF techniques should be carefully revisited and those already published [by ASHRAE] should be used with caution." [34]

This highlights a difficulty with these methods: users relying on sequences of coefficients as the basis of heating or cooling load computations must take the accuracy on faith. There is little correspondence between these sequences of values and the physical or climatic phenomena being modeled.

In the case of the Admittance Method, both the heat flows and temperatures at both indoor and outdoor surfaces are assumed to be purely sinusoidal functions with a period of 24 h [34] [10]. Urbikan and Davies [10] describe the historical development of the Admittance Method and point out four limitations. (i) The assumption of steady-cyclic indoor conditions only occurs after "a few days of near-repetitive weather conditions" and is unrealistic. (ii) Using the single 24 h harmonic for all input values, limits the accuracy but using additional higher frequency harmonics of the climate data and "transmittance" and "admittance" values would increase the computational effort significantly. (iii) The

Admittance Method assumes that all resistances and capacitances are *static* values throughout a simulation and (iv) it cannot process input data in real-time.

A more detailed variation of the admittance method, allowing for the study of advanced control strategies of HVAC systems in addition to thermal and energy analysis of a building, is presented by Athienitis et al [36]. An admittance matrix of the form of Eqn. 3 (commonly significantly larger size) derived from a thermal circuit ("network model") of a building is the basis of this detailed method. The method involves various mathematical operations including: (i) inverting the admittance matrix evaluated at chosen frequencies, (ii) performing a least squares complex interpolation on the resulting transfer functions obtained at the chosen frequencies [36] and (iii) computing the discrete Fourier transform of the weather data [37]. The methodology is flexible, allowing for the use of both simple and detailed models of a building. A detailed model of a simple house including long wave radiant heat transfer among indoor surfaces is presented [36].

2.1.3 Finite Difference Method

Eqns. 1 and 2 express relationships between the conductive heat transfer rate through a wall layer and the first and second partial derivatives of temperature with respect to depth position and time. That is, how $\dot{Q}_{conduction}(x,t)$ is related to the manner that *T(x, t)* changes with time and depth position in the wall layer. The Finite Difference Method (FDM) approximates solutions to these functions by replacing these differential equations with algebraic equations. This is done by dividing up both time *(t)* and depth *(x)* into a finite series of points at which solutions to $\dot{Q}_{conduction}(x,t)$ and *T(x, t)* are found by replacing derivative expressions with easily calculated difference expressions [13].

For example, the FDM formula for an approximation of $\dot{Q}_{conduction}(x,t)$ at the depth position x_c and at time t_c is shown in Equation 4 below, based on known values of temperature $T(x_1, t_c)$ and $T(x_2, t_c)$ on either side of the depth position of interest x_c : $x_1 < x_c < x_2$.

$$\dot{Q}_{conduction}(x_c,t_c) = -kA\frac{dT}{dx}(x_c,t_c) \approx -kA\frac{\Delta T}{\Delta x} = -kA\frac{T(x_1,t_c)-T(x_2,t_c)}{x_1-x_2} \qquad (4)$$

Here, a linear approximation of the partial derivative with respect to wall depth *(x)* is made using a difference calculation involving $T(x_1, t_c)$ and $T(x_2, t_c)$. The smaller the distance between x_1 and x_2, the more accurate this approximation is. This is done at a finite number *(n)* of wall depth positions resulting in *n* such linear equations approximating the continuous heat transfer rate throughout the depth of the wall layer. This is done at every time step t_i (shown above for one time step t_c).

As in the case of Response Function Methodologies, *boundary conditions* modelling the heat transfer occurring at surfaces must be specified. For example, external surface convection resistances model the resistance mediating the heat transfer rate between the outdoor air

and outer wall layers. These can be static values that do not change with time or equations based on, for example, time-varying wind speed and direction [20].

Some comments from the literature about the Finite Difference Method follow.

> *"In principle, the method is accurate especially at high construction element layering resolutions and low time intervals but the large number of simultaneous calculations renders the method computationally demanding especially at time intervals relevant to plant and control system simulations."* [21]

> *"Numerical techniques have the advantage of being conceptually simple and amenable to both linear and nonlinear boundary conditions."* [15]

> *"The generality of these [Finite Difference] methods allow their direct application to the spectrum of target domains – building heat transfer, HVAC psychometric processes, …"* [20]

> *"When it comes to the realistic testing of design prototypes, the numerical method [Finite Difference Method] has no master …"* [20]

2.1.4 Lumped Models

This fourth category of modelling methodology is prevalent in research domains and as was the case of the previously described methods, development occurred in the context of limited available computing power. The basic strategy of this methodology is to represent building elements (or complete zones) in as few thermal circuit elements as possible (lumping) when assembling a thermal circuit of a building. Electric circuit analysis techniques are applied to the simple circuit in order to derive the differential equations directly from the circuit diagram. Such analysis techniques include the use of Kirchhoff's Current and Voltage laws and nodal/mesh analysis [18] [38]. These first order ordinary differential equations (*not* Eqns. 1 and 2) have time *(t)* as the one independent variable and are solved analytically [18, 19] or using an automated equation solving program such as MATLAB [39]. These few equations can be solved analytically because of the simplifications in the lumping process. In comparison to the previous methods described, this method simplifies the problem complexity at the model construction phase as opposed to the computation phase. The resulting computations are simpler and therefore can be made with greater accuracy. These models are sometimes referred to as "Simple Models" in the literature.

Various configurations and orders of circuit models of single zone rooms or buildings have been proposed: 3 resistors and 1 capacitor [40, 41], 4 resistors and 2 capacitors [42], 3 resistors and 2 capacitor components (3R2C) [18, 19, 21, 43, 44], and many resistors and 3 capacitors [38]. Gouda et al [21] derived the component values of their 3R2C circuit using an

nonlinear optimization scheme that resulting in the "best" component value assignments when compared to a 21R20C benchmark circuit solution. The solution of the 21R20C circuit was obtained by solving the corresponding differential equations using the Simulink component of MATLAB [45]. In general, as the number of components increase, complexity of these ("simple") Lumped Models increases in terms of component value assignments, equation derivation and equation solution techniques.

> *"Potential advantages of simplified thermal models include reduced computing overheads, shorter coding, analytical solution of the state equations and easier verification."* [21]

The main drawback to these models is the question of accuracy due to the simplifications made at the thermal model construction phase including simplifications to boundary conditions (surface interactions) [21] [9, 38]. Of the general modelling methodologies presented, the Lumped models provide the most accessible insights into Building Physics due to their simplicity and the connection between a thermal circuit diagram, equation derivation and resulting computations. Unfortunately these insights can be limited due to the simplifications entailed in the model and presented in the thermal circuit diagram. As well, when complexity is added to a lumped model to improve accuracy, often the changes are grounded in numerical efficiency/accuracy and not physical considerations [21]. The methodology presented in this thesis and introduced in the next chapter, builds on the positive aspects of Lumped Models in terms of elucidating Building Physics.

2.1.5 Discussion
Building Physics, Physical Correspondence
The previous brief description of Response Functions methods skimmed the surface of the complex mathematical procedures involved. Most of these procedures and the resulting computation formulas (series) have very little *physical* correspondence with the exception of some aspects of Periodic Response Functions [33]. This is not surprising since the methods were motivated by the early limitations of available computing power and "*emerged in response to the need to introduce dynamic considerations into manual methods*" [20]. That is, the methods were not *directly* motivated by the physical properties of buildings and climate. Therefore, Building Physics is not illuminated by these techniques and a user is more likely to be either preoccupied with the mathematical procedures involved or likely to use a simulation program based on these methods as a black box with the computation techniques remaining a mystery.

The Finite Difference Method (FDM) provides some insight into Building Physics simply because it is a method for solving *any* first or second order (partial) differential equation including Eqns. 1 and 2. *Further* insight into Building Physics can be gained by deriving the FDM linear approximations to Eqns. 1 and 2 using a procedure based on discretizing the depth of the wall and applying a heat balance argument at each discrete segment of the wall

depth [13]. For example, this procedure sheds light on the interaction of surface dynamics with heat flows through the wall. Unfortunately, the affinity of FDM with Building Physics is hidden from the user of building simulation programs based on FDM since the only related input the user *may* provide to the simulation process is the required accuracy or time step size *(Δt)* and degree of discretization of the wall depth *(n)*.

Of the four methodologies briefly discussed here, the Lumped Models methodology provides the most accessible insights into Building Physics due to the simplicity of the models and the connection between a thermal circuit diagram, equation derivation and resulting computations. The insights can be limited due to the simplification and lumping process which includes the removal of model representations of thermal processes. For example, convective and radiative heat transfer are both non-linear heat transfer processes active on the outer surfaces of a building that are often approximated using a single static heat transfer coefficient *($h_{combined} = h_{rad} + h_{conv}$)* [13]. When implemented as such, the distinction between and the (non-linear) nature of, these two fundamental heat transfer processes vanishes. Also, lumping simplifications can result in thermal circuits that do not *directly* correspond to the physical configuration of the building [18].

Accuracy
Gouda [21] points out that during the 1960s/1970s, the Response Factor methods led to "substantial" computing efficiencies that were "crucial" at the time, but less significant in the last decade (1990s), given recent levels of commonly available computing power. Gouda also states that the accuracy of these methods are questionable at time steps less than one hour as required for "fully dynamic plant simulations". A report by Duska et al [34] highlighted the potential difficulty with the various Response Function methods concerning accuracy: coefficients that result from the complex mathematics used to solve Eqns. 1 and 2 can be used blindly with their accuracy difficult to confirm. Urbikan and Davies [10] cataloged the shortcomings of the Admittance Method (a Frequency Doman Response Function Method). Three out of four of these impact the accuracy of this method.

In general, the Finite Difference Method does not impose accuracy limitations on the resulting linear approximations to Eqns. 1 and 2: the accuracy of an implementation can always be improved by choosing a finer resolution of discretization of time and wall depth (smaller and more numerous slices). The method includes a tradeoff between accuracy and computing load: improving the accuracy increases the computing load. This tradeoff *was* a serious consideration in the early implementations of this method but is less of a constraint today with relatively high levels of computing power commonly available.

Authors of papers describing Lumped Models often do not make significant claims in terms of accuracy of their models compared to large building simulation programs, since the primary aim of these models is to reduce the model complexity and the resulting analysis and computations. These models are often suggested to be appropriate for the early stages

of design or planning where high accuracy is not demanded [18, 46]. Accuracy is commonly a shortcoming of these models, but is generally an accepted one.

Summary

With current high levels of computing power commonly available and continuing to rise, the motivation for complex approximations to the solutions to Eqns. 1 and 2 is vanishing. Related to this is the concern that the Finite Difference Method (FDM) is computing-intensive: the concern is diminishing and will continue to diminish as computing power increases. This makes FDM particularly attractive as the basis of a simulation program: accuracy can be increased by the user parametrically (e.g. reduce the time step) to match the available (increasing) computing power.

In the literature, thermal circuit models are used to describe thermal phenomena and/or to derive "simple" Lumped Models. As the basis for a simulation methodology, the thermal circuit is used primarily in Lumped Models where it is of central importance. The physical justifications for the lumping (simplifications) as well as the derivation of the governing differential equations is done via the circuit diagram. This is the source of the unique affinity between Building Physics and the Lumped Models. Again, the utility of reduced computing loads of the Lumped Models is rapidly reducing in significance while other positive attributes remain: simpler verification, short implementation times [21]. The major drawback being accuracy of these models. Note that simulations are *never performed directly* from a thermal circuit diagram of a Simple Model.

In terms of accuracy, the FDM method is the most promising while in terms of affinity with Building Physics, the Lumped Model category exceeds the rest. Described in the next chapter, the methodology in this thesis inherits the best of these two methodologies.

2.2 The Building Time Constant

A detailed investigation of the building time constant as a useful output of thermal analysis using circuit models is presented in this thesis. The building time constant (τ) can be generally thought of as a measure or indication of the *thermal inertia* of a building. Specifically, τ indicates the response time of the thermal mass of a building to temperature changes such as an outdoor temperature swing. It is the basis of estimating the indoor air temperature response to a sudden and constant change in outdoor temperature [47]. Additionally, τ has been used as an input parameter for heat demand prediction in residential buildings [48] [49] and as a parameter in estimating useful solar gains in a building [50]. Catalina et al state:

> *"The higher the time constant of the building is, the larger fraction of solar gains can be used in winter and slower it responds to sudden changes."* [48].

Knowing τ enables the prediction of a indoor temperature *(T_{indoor})* of a building in response to a sudden drop or increase in outdoor temperature *($T_{outdoor}$)* [47]. For the case of no internal gains or artificial cooling, if both the indoor and outdoor air temperatures are initially $T_{indoor}(0) = T_{outdoor}(0) = T_0$ and a constant *signed* step change in outdoor temperature occurs $T_{outdoor}(t) = T_0 + T_{step}$ *(t > 0)*, then the indoor temperature response can be predicted as [47]:

$$T_{indoor}(t) = T_{outdoor} - T_{step} \cdot e^{\frac{-t}{\tau}} \qquad \text{where: } T_{step} = T_{outdoor} - T_0 \qquad (5)$$

In Chapter 6, the circuit response to an outdoor temperature step change is determined using Micro-Cap and this response is compared to the corresponding response curve defined by Eqn. 5 above.

There are many calculation procedures for τ of varying complexity [47, 51, 52] with some calculations based on experimental data such as: Δt, the growth/decay period; $T_{indoor}(0)$, $T_{indoor}(\Delta t)$, the indoor temperature at the start and end of the decay period; and $T_{outdoor}$, the constant outdoor temperature throughout the period. With these known values, Eqn. 5 can be used to solve for τ. Of the formulas presented by Antonopoulos [47],

$$\tau = R_T C_T \qquad (6)$$

is *not* based on experimental temperature data and is the formulation adopted by the ISO [51]. Here, R_T (°C/W) is the *net* thermal resistance between the inside and outside air and C_T (J/°C) is the simple summation of all the heat capacities of the of the building construction (Eqn. 6.1 includes a more detailed description). Antonopoulos [53] refers to C_T as the *apparent* thermal capacitance of a building in contrast to the *effective* thermal capacitance (C_{eff}). Antonopoulos characterises C_{eff} as the thermal capacitance that

> *"determines the amount of thermal energy which may be stored within a structure."* [53]

In contrast,

> *"The summation of specific heats of all building elements into a lumped apparent thermal capacitance C_a [C_T] is a rough approximation [to C_{eff}], because the ability of structural elements to store heat is different when these are distributed in the building or considered together in forming a unified volume."* [53]

Antonopoulos [47] reports that Eqn. 6 *can* lead to overestimations of τ by more than 100% due to the discrepancy between C_T and C_{eff}. This is not confirmed in this thesis and Eqn. 6 is used in Ch. 6 to generate τ values that are compared to circuit computed τ values.

Antonopoulos [54] also found that indoor mass ("*i.e. interior partitions and furnishings*") has a considerable effect on the computation of the building time constant and on the thermal delay of a building. One would expect the significance of this effect to be based on how the indoor mass total compares to the building envelope construction mass total. Indoor mass is not investigated in this thesis.

The electric circuit theory supporting the computation of the building time constant using electric circuits is presented in Chapter 3.

2.3 Modelled Components

Thermal models of buildings require climatic inputs and often require assumptions to be made in the form of parametric values. For the low energy house modelled in this thesis (introduced in Ch. 4), a base infiltration rate was required (independent of additional manual or mechanical ventilation/infiltration). Although many climatic inputs to simulation models of buildings are directly available from climate data files such as IWEC [55], some inputs are not available. These include: ground temperature, sky temperature and solar irradiance values for surfaces at various orientations (e.g. a wall). Computations of hourly sequences of these three climatic inputs were required when running simulations using the circuit models of this thesis. Each computation of an hourly sequence is based on a component model (e.g. ground temperature model) chosen from the literature. Details of the literature search for each of the three component models and base infiltration rate are presented in this section.

2.3.1 Base Air Infiltration Rate

As mentioned previously, a base infiltration rate that approximates the average air-tightness of a recently constructed house in Sydney, Australia is required. Unfortunately there is very little precise information concerning the average infiltration rates of existing and new buildings in Australia:

> *"Information concerning the actual air tightness, infiltration and air change rates is probably the least known subject matter of building performance in Australia. (2007)"* [56]

More recently, the same author reported the situation as unchanged:

> *"At present, there is no institutionalised scientific program on air leakage performance for Australian construction."* [57]

The Tasmanian government published a report [58] in 2003 making a similar statement and which summarized studies of "*natural*" infiltration rate estimates of homes in various Australian cities. One study reported 3 rates: Canberra: 0.44 ach, Sydney and Hobart: 0.55 ach and Melbourne: 0.57 ach. A second study found infiltration rate of Melbourne houses to be 0.33 ach. A third study found infiltration rates as more varied: 0.2 – 2.3 ach in Sydney dwellings. These cited studies took place between 1985 and 1991 and the report acknowledges

> *"Because so many new residential buildings are being constructed in Australia following 'energy efficient' construction methods it is highly likely that infiltration rates in some new dwellings may well be below levels considered essential for reasonable air quality."* [58]

It is assumed that "natural" refers to normal pressure: 2.5 Pa. The low energy house modelled in this thesis (Chs. 4, 5) is assumed to be a recent construction of simple design made from good insulating materials. Taking this and the incompleteness of infiltration data of new residential buildings in Australia into account, the base infiltration rate used in the circuit models of this thesis was chosen to be 0.33 ach (normal pressure: 2.5 Pa).

2.3.2 Ground Temperature

A suitable model for the ground temperature throughout the year is required for modelling conductive heat transfer between the indoors and ground. Although the Kusuda model [59] of ground temperature is somewhat dated, recent research and modelling involving ground temperatures at varying depths [60, 61], are based on this model. As well, TRNSYS adopted this model as the basis for a system subroutine (Type 77): "Simple Ground Temperature Profile" [62].

Kusuda [59] presented an equation for modelling ground temperature at varying depths throughout the year which for ground surface temperature ($x = 0$) reduces to:

$$T_{gnd\_surface}(t) = T_{mean} - T_{amp} \cdot cos\ [2\pi/8760 \cdot (t - Phase)] \qquad (7)$$

Kusuda used the more accurate earth temperature cycle period of 8766 h or 365 ¼ days which is here rounded down to 365 days to match the length of the IWEC Sydney outdoor temperature data sequence [55].

In Eqn. 7, t is in days, T_{mean}, T_{amp} are the average and amplitude of the surface temperature and *Phase* is the phase angle of the surface temperature cycle. Kusuda determined the values of the latter three parameters by performing least-squares fitting to earth temperature cycles of monthly averages from various locations in the US.

Kusuda [59] also investigated the correlation between each of the air and ground surface temperature model parameter values of T_{mean}, T_{amp}, and *Phase*. He concluded that $T_{mean\_gnd\_surface}$ can be "reasonably well estimated" using T_{mean_air} and $T_{mean\_gnd\_surface}$ can be "approximated" with "somewhat less accuracy" by $T_{amp\_air\_monthly\_avg}$, while $Phase_{air}$ and $Phase_{gnd\_surface}$ "do not show a definite correlation". The correlation graph between the 2 sets of Phase values shows a tight clustering around the $y = x$ line but no definite linear relationship. In the absence of other data, $Phase_{air}$ of the monthly average air temperature cycle is used to model $Phase_{gnd\_surface}$. This is the approach suggested by TRNSYS [62].

2.3.3 Sky Temperature

A suitable model for the sky temperature throughout the year is required for modelling radiative heat transfer between the outer surfaces of a building envelope and the sky.

Duffie and Beckman [63] point out that sky temperature is not significant when investigating solar collector performance but

> " ... is critical in evaluating radiative cooling as a passive cooling method."

The low energy house presented in Chapter 4 has a flat unobstructed roof (maximum sky exposure) with relatively large surface area compared to the walls. Therefore it is probable that the radiative heat transfer with the sky is a significant when modelling heating/cooling energy requirements and thermal performance of this house.

The IDA ICE [64] model of the low energy house used in this thesis includes the simple formulation of the sky temperature as a direct dependency on the outdoor temperature:

$$T_{sky} = T_{outdoor} - 5 \qquad (8)$$

Aubinet and the Canadian Ministry of Natural Resources[65] suggest this relationship between sky and outdoor temperature is valid for cloudy (overcast) skies only with clear skies being cooler. The IEA [66] documents the use of this relationship based on "personal communication" but also state that more sophisticated models are available.

Zhi-lei et al [67] and Sani [68] developed building simulation models that included the modelling of sky temperature as:

$$T_{sky} = T_{outdoor} - 12 \qquad\qquad (9)$$

Both authors do not specify cloudy or clear skies and presumably use Eqn. 9 for all sky conditions.

Pandey et al [69] investigated numerous models of clear sky emissivity that depend on dew-point temperature (T_{dp}). The summary table from this paper is repeated below with T_{dp} in °C.

Equation	Reference
$\varepsilon_{sky} = 0.8004 + 0.00396T_{dp}$	Bliss [70]
$\varepsilon_{sky} = 0.787 + 0.0028T_{dp}$	Clark and Allen [71]
$\varepsilon_{sky} = 0.734 + 0.0061T_{dp}$	Berdahl and Fromberg [72]
$\varepsilon_{sky} = 0.770 + 0.0038T_{dp}$	Berger et al [73]
$\varepsilon_{sky} = 0.711 + 0.0056T_{dp} + 0.000073T_{dp}^{2}$	Martin and Berdahl [74]

Table 2.2: Clear Sky Emissivity Equations from Pandey[69]

The sky emissivity is then used to derive the sky temperature from the outdoor temperature:

$$T_{sky} = T_{outdoor} \times \varepsilon_{sky}^{1/4} \qquad \text{with } T_{sky}, T_{outdoor} \text{ in °K} \qquad (10)$$

Duffie and Beckman [63] choose Martin and Berdahl's emissivity formula (ε_{sky_M+B}: row 5 of Table 2.2) and add a minor adjustment resulting in the emissivity and sky temperature formulations shown in Eqns. 11 and 12 below.

$$\varepsilon_{sky\_D+B} = \varepsilon_{sky\_M+B} + 0.013cos(15t) \quad \text{with } t: \text{ daily hour number from midnight} \qquad (11)$$
$$T_{sky} = T_{outdoor} \times \varepsilon_{sky\_D+B}^{1/4} \qquad (12)$$

Type 15 of TRNSYS [62] adds 2 modifications to the Duffie and Beckman sky emissivity formula (Eqn. 11) resulting in a formulation for sky temperature that models *both* clear and cloudy skies (Eqn. 13) shown below.

$$\varepsilon_{sky\_TRNSYS\_1} = \varepsilon_{sky\_D+B} + 0.00012 \times (pressure - 1000)$$
$$\varepsilon_{sky\_TRNSYS\_2} = \varepsilon_{sky\_TRNSYS\_1} + (1 - \varepsilon_{sky\_TRNSYS\_1}) \times f_{cloud} \times \varepsilon_{cloud}$$
$$T_{sky} = T_{outdoor} \times \varepsilon_{sky\_TRNSYS\_2}^{1/4} \qquad (13)$$

Where *pressure* is the atmospheric pressure (Pa), $\varepsilon_{cloud} = 0.9$ and f_{cloud} is a value between 0 and 1 indicating the degree of cloud cover. Both *pressure* and f_{cloud} are hourly values available in climate data files such as IWEC [55].

Figures 2.1 and 2.2 below show the sky temperature sequences for 20 days in January and July calculated using Sydney IWEC climate data and the following Equations: 8, 9, 10-Bliss, 12 and 13. Of the four clear sky temperature sequences *not* shown in Figs. 2.1, 2.2, the sequences of Clark and Allen, Berger et al and Berdahl and Fromberg are below the Bliss sequence (Eqn. 10-Bliss) and above the Duffie and Beckman sequence (Eqn. 12) while the Martin and Berdahl sequence is roughly equivalent to the Duffie and Beckman sequence. Where the sky temperature sequences of Duffie and Beckman and TRNSYS overlap, this indicates durations of clear skies with $f_{cloud} = 0$ (no cloud cover) of Eqn. 13. For example, this occurs in the neighbourhood of hour 4584 of Fig. 2.2.

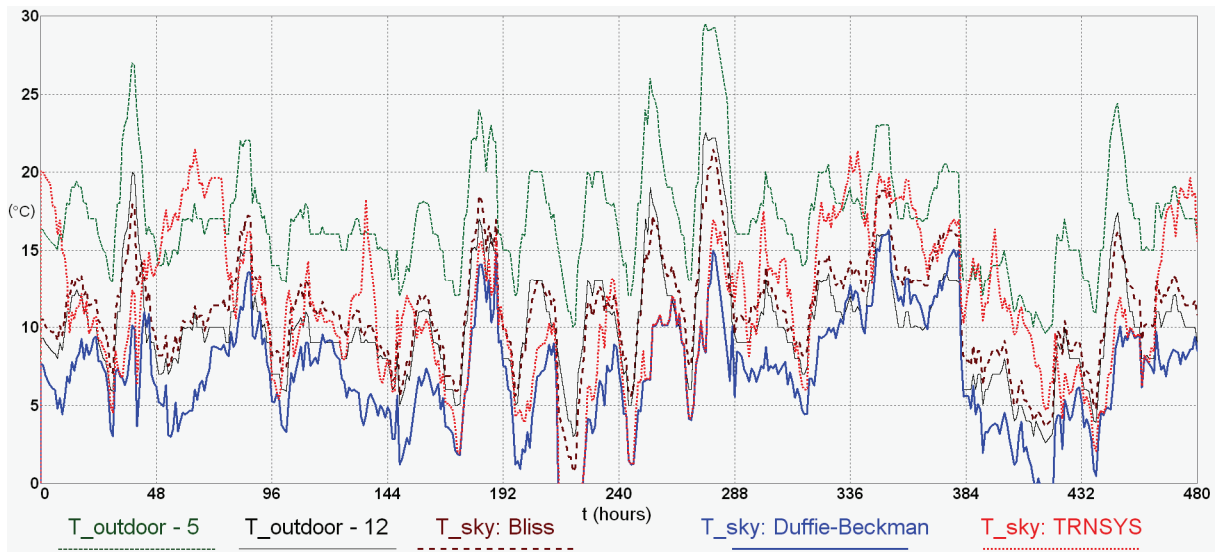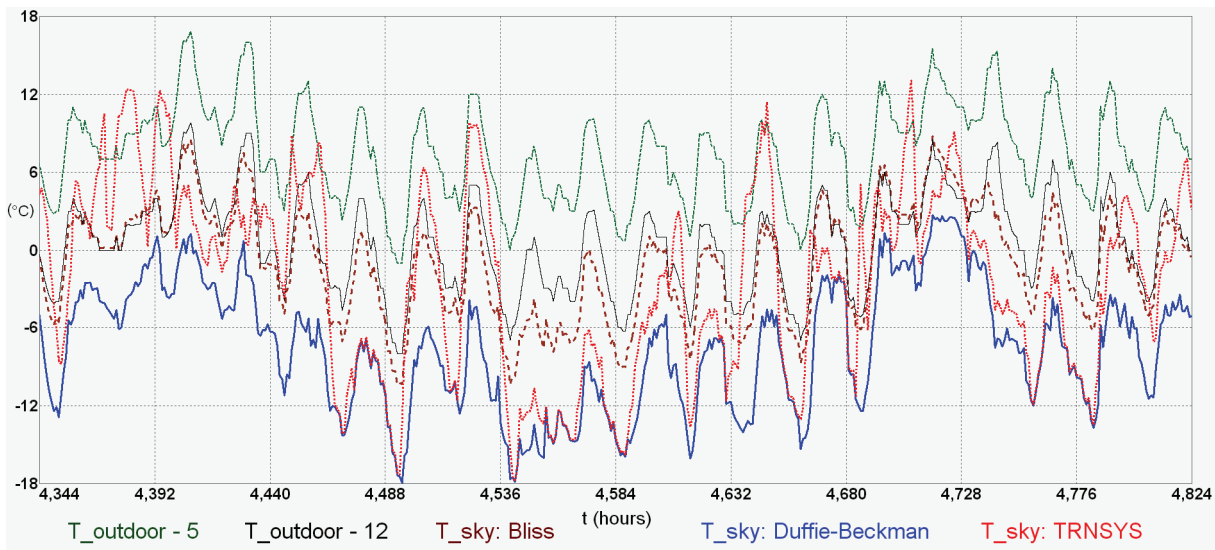**Figure 2.1**: Sequences of Sydney Sky Temperature Models for Jan 1-20.

Figure 2.2: Sequences of Sydney Sky Temperature Models for July 1-20.

Of the sky temperature models presented here, it is likely that the most accurate is the TRNSYS model (Eqn. 13) due to the fact that it models both clear and a cloudy sky conditions whereas the others are either specifically clear sky models (Table 2.2) or directly based on

20

outdoor temperature only (Eqns. 8, 9). At the time of choosing a replacement model for the IDA ICE sky temperature model (Eqn. 8) for the low energy house model described in Chs. 4 and 5, the TRNSYS model was not known to the author. As a result, the Bliss formula [70] for sky emissivity and resulting T_{sky} formula (Eqn. 10) was chosen since it produced a sky temperature sequence that is roughly "average" amongst the various sequences besides the TRNSYS sequence. It is the most conservative choice of emissivity formulas reported by Pandey et al [69] in terms of resulting T_{sky} (warmest) and this T_{sky} formulation correlates with Eqn. 9: $T_{sky} = T_{outdoor} - 12$. For IWEC Sydney climate data, the yearly average sky temperature is 5.94°C using the Bliss model and 6.17°C using the TRNSYS model.

Regardless of the shortcomings of the choice of the Bliss model over the TRNSYS model, this choice achieves two aims. Firstly, it illustrates the ease by which a new model component can be integrated into a Micro-Cap circuit model (shown in Ch. 5). Secondly, by changing the sky temperature model from $T_{sky} = T_{outdoor} - 5$ (Eqn. 8: IDA ICE) to the Bliss model (Eqn. 10: Bliss) which correlates with $T_{sky} = T_{outdoor} - 12$, a sensitivity analysis based on roughly a 7 degree drop in sky temperature is facilitated.

2.3.4 Solar Radiation

The methodology used to incorporate solar radiation into the circuit models of this thesis is based on the simple building simulation tool of Nielsen [18] with some modifications and omissions. This model falls into the Lumped Model category previously described in section 2.1.4. A thermal circuit diagram reproduced from Nielsen's paper is shown in Figure 2.3 below. All of the mass of a house construction is lumped into one capacitor component (C_w) while the heat capacity of the indoor air makes up the second capacitor component (C_i) of this model. *Only* solar gain through glazing (Q_{sun}) is considered in this model and the total solar gain through all glazing is divided amongst two heat sources, connected separately to the two capacitors $(W_w + W_a = 1)$. The two heat sources model solar radiation absorbed by the indoor surfaces and by the indoor air.

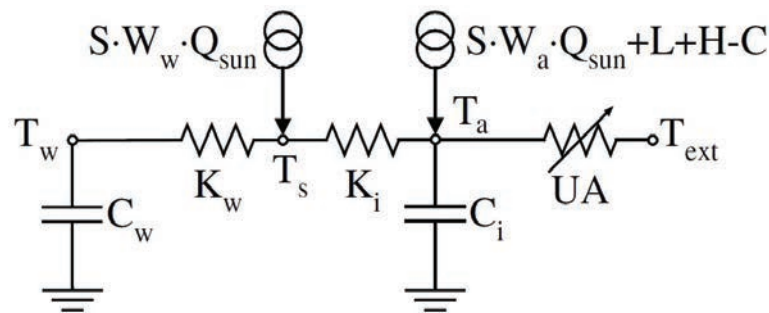**Figure 2.3**: Thermal Circuit of Nielsen's Lumped Model [18].

Nielsen's computation of total transmitted solar gain (Q_{sun}) through glazing is based on summing three solar gain components for glazing at each orientation: direct beam solar gain, diffuse solar gain and ground reflected solar gain. Each of these solar gain components are based on the corresponding hourly irradiance computation at each orientation. The

three hourly irradiance sequences are computed from hourly direct normal and hourly diffuse horizontal, irradiance sequences available in climate files such as Sydney IWEC [55]. The diffuse irradiance sequence computation uses the Perez Diffuse Sky Model [75, 76]. Computation details of the three irradiance sequences are given in Appendix B.

Each of the three solar gain components are computed from the glazing area, the corresponding irradiance sequence and the corresponding solar heat gain coefficient *(SHGC)*. The *SHGC* for direct beam irradiance varies with angle of incidence *(θ)* of the sun for a particular orientation. Nielsen uses the model of Karlesson and Roos [77] to determine the *θ*-dependent *SHGC* for a particular glazing type. This results in a *SHGC* for direct beam solar gain computations that varies with time, location and orientation. The *SHGC* for the diffuse and ground reflected solar gain computations are taken to be constants and based on the *SHGC* quoted by the glazing manufacturer which specifies gain for direct beam solar radiation normal to the glazing *(SHGC$_0$: θ = 0°)* [78]. Computation details of the *SHGC* for the three solar gain components as applied to the low energy house modelled in this thesis using the Karlesson-Roos model are given in Appendix C.

Nielsen also applies correction factors to the direct solar gain computation that take into account "far" and "near" shading due to landscape/buildings and overhangs.

The following modifications to Nielsen's methodology are included in the methodology used to incorporate solar radiation in the circuit models of this thesis. The houses modelled in this thesis are assumed to be completely unobstructed: no correction factors are applied to incident solar radiation. Solar radiation absorbed by the *opaque* envelope of a house *is* included in the circuit models (glazing and window frames are modelled as having no capacitance). All solar radiation transmitted by the glazing (solar gain) is absorbed by the floor: direct absorption of solar gain to the indoor air is ignored and the floor is assumed to not reflect any portion of the transmitted solar radiation.

Unrelated to the treatment of solar radiation, the thermal circuit shown in Fig. 2.3 does *not* have a *direct* physical correspondence to a building. There is no difficulty with the four nodal temperatures T_w, T_s, T_a, T_{ext}: average temperature of the construction mass, average temperature of the inner surfaces, the indoor air temperature and the outdoor air temperature respectively. The difficulty arises when considering the three conductances (W/°K, the inverse of thermal resistance): K_w, K_i and UA. These are defined by Nielsen [18]: K_w is the "conductance between the heat capacity in constructions and internal surfaces", K_i is the "conductance between the internal surfaces and indoor air", and UA is the "conductance to external environment" including infiltration/ventilation. Unlike the latter two conductances, Nielsen points out that K_w is not well defined and provides the formulation shown below.

$$K_w = \sum_{i=1}^{N} \frac{A_i}{r_{eq,i}} \qquad\qquad (14)$$

Where A_i is the area and $r_{eq,i}$ is the "equivalent thermal resistance", for internal surface i.

Nielsen does not define $r_{eq,i}$, but states it is based on "the dynamic heat capacity" (it is *not* the standard inner surface resistance). This in itself presents a problem for users wishing to implement this model or understand the physical correspondence. If the heat conduction paths are considered beginning from the outdoor temperature node (T_{ext}) progressing left in Fig. 2.3, an unhelpful physical correspondence results. From the outdoors an envelope with no thermal mass encases a body of air itself encasing all the thermal mass of the building. This picture does not provide a good basis of understanding the Building Physics being modelled. Not uncommon to Lumped Models, Nielsen states that the model structure of Fig. 2.3 was "chosen in order to simplify the calculations and increase the calculation speed" [18]. This contrasts with the circuit models of this thesis presented in Chapters 4 and 5 that clearly illustrate the heat flow paths between outdoors and indoors passing through construction materials containing *both* thermal capacitance and resistance (a more realistic representation of building layer materials).

3 Modelling Methodology

In Chapter 2, the dominant modelling techniques currently used in building simulation programs were briefly reviewed. In this chapter the modelling methodology in this thesis is presented. A general theoretical description is given followed by a detailed treatment of the Thermal-Electrical analogy in terms of mapping thermal phenomena to electrical component values. Chapter 4 continues the description of this analogy in the context of modelling a low energy house.

The methodology produces transient models for thermal building simulation based on RC circuits specified using the graphical user interface of an electric circuit solving program. The solver generates time domain and frequency domain simulation output directly from the circuit diagram. In terms of the modelling categories discussed in Ch. 2, this methodology is an amalgamation of FDM models and Lumped Models giving the user complete control over model complexity and accuracy. This is further discussed in this chapter. In this thesis, frequency domain output is presented in terms of the Bode plot, a graph displaying the relative magnitude of the indoor temperature response to a change in outdoor temperature at a particular frequency. This is done at a wide spectrum of frequencies and is also referred to as *the frequency response*.

As previously discussed, the analogy between electric circuit theory and thermal engineering theory has a long history and is documented in many textbooks [9, 13, 79, 80]. This thermal-electrical analogy, summarized in Table 2.1, is the theoretical basis of thermal modelling using electrical circuits. Most thermal circuit symbols originate from electric circuit diagrams and this indicates the centrality of this analogy.

3.1 Description of Methodology

The modelling methodology in this thesis employs the Thermal-Electrical analogy throughout the model design and simulation stages and thereby gain advantages over the previous methodologies. The starting point of a model design, the thermal circuit, is the actual model. The circuit is directly compiled by the electric circuit simulator (Micro-Cap) with results generated in the electrical domain that are interpreted in the thermal domain. This bypasses the step of generating and solving differential equations to produce simulation results, common in other modelling methodologies. The user-focus is the thermal circuit diagram which encourages physical understanding since circuit components directly represent physical properties (e.g. thermal capacitance, thermal resistance). The thermal circuit diagram is the obvious user interface choice for thermal modelling since it has a long history of usage in thermal modelling design and presents information in an organized and transparent manner. This is further discussed in Chapter 4.

Modelling with electric circuits and Micro-Cap solves Eqns. 2.1 and 2.2 (Fourier's law of heat conduction, heat conduction equation) using the Finite Difference Method in two manners. Firstly, the circuit simulator (Micro-Cap) models (computes) the time variable *(t)* with the

user able to specify the time step size before running a simulation. The time step choice can be made before each simulation, but is generally done less frequently. The choice can be made by trial and error using the basic guideline that decreasing the time step size results in increased accuracy and computation load.

The modelling of the wall depth variable *(x)* is achieved in a different manner. There is no independent variable in the electrical domain that is analogous to the wall layer depth variable *(x)* of Eqns. 2.1 and 2.2. The electrical modelling of wall depth is achieved by dividing the resistance and capacitance of a wall layer into n discrete elements forming an nth-order RC ladder circuit representation of the wall layer. The choice of n is made by the user and this can be viewed as the degree of lumping of the capacitance in the wall layer representation. Therefore the previously described Lumped Models category is consistent with this modelling methodology: the user is able to specify as simple or complex a model that includes any order of lumping. A low order (e.g. 1 capacitor) representation of a wall layer can be initially specified and at a later time, replaced with a higher order and more accurate representation (RC ladder) in a straightforward manner (Fig. 3.1). This is an example of the flexibility of this methodology. The RC ladder representation of wall layers is discussed in Chapter 4 and a strategy for choosing n is presented in Appendix A.
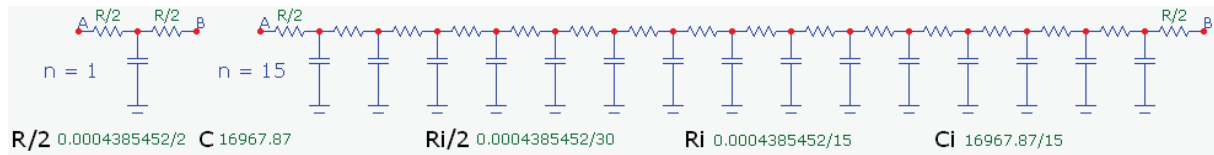
Figure 3.1: Single Wall Layer Models: Single Order and 15th Order (Increased Accuracy)

The single-order *(n = 1)* RC ladder shown above in Fig. 3.1 has the significant limitation of only being able to generate a maximum time lag of 6 h between indoor and outdoor peak temperatures. This is a consequence of the maximum phase angle between voltage and current through a single RC circuit (Fig. 3.4) being 90˚. Lumped Models based on a single capacitor are not uncommon [40, 41, 81]; one such model is presented in Ch. 6.

The time variable *(t)* of Eqns. 2.1 and 2.2 is modelled by the Micro-Cap simulation engine with the user able to specify the resolution of simulation time (time-step size). At each time step, circuit components are evaluated and current and node voltages are determined based on these values. This is an example of the discretization of time *(t)* using the finite difference method, while the RC ladder representation of a wall layer is an example of the discretization of a wall layer depth *(x)*. In the example 15th order model representation of a 300 mm wall layer shown in Fig. 3.1 above, each node from A to B of the RC ladder represents positions at 20 mm intervals of layer depth: A (0 mm), 10, 30, 50, ... , 290, B (300 mm). These nodes provide points within a wall layer where temperature and heat transfer rate may be easily monitored during a simulation.

Boundary conditions can be specified in a direct manner with no accuracy limitations placed on the user. Surface resistances modelling convective and radiative heat transfer can be specified either as simple static values or as time-varying algebraic expressions of node voltages (temperatures) enabling non-linear relationships to be modelled accurately as shown in Eqn. 4 below. Surface resistance modelling is further described in the section that follows and in Chapter 4. Solar radiation input is also modelled in direct and intuitive manner without the need to transform solar radiative heat transfer into an equivalent ambient temperature ("Sol-air" temperature) that some response function modelling methods require [25, 31-34]. A current source component modelling the absorbed solar heat transfer is connected to the corresponding circuit node (e.g. an outer wall surface).

Basic modelling functionality provided by most established building simulation programs includes heating/cooling load computation as well as indoor air temperature sequence generation over a specified time period. This functionality is achieved using the methodology in this thesis with computations made directly from thermal circuit diagrams specified within Micro-Cap by the user. In general, sequences of the transient temperature and heat transfer rate at *any* node of the thermal circuit can be computed, displayed and summed over a time period. This includes nodes *within* the depth of a wall layer. One of the distinguishing strengths of this modelling methodology is the ease by which frequency-based analysis of a building model can be achieved. The frequency response ("Bode" plot) can also be generated directly from the circuit diagram. This contains useful information in itself, but it also enables the direct and simple computation of the "building time constant" described below in section 3.3. Detailed examples of computing the building time constant of a low energy house (including Bode plots) using Micro-Cap are presented in Chapter 5.

3.2 Circuit Model Components

Building modelling using the electrical analogy consists of mapping construction properties and climate data into electrical components, assembling an electric circuit model (Fig. 3.3) and interpreting model results in terms of building properties, energy and climate. The four electrical components used to build an electric circuit model are described in terms of the thermal phenomena that can be modelled. The time constant of an electric circuit is described in relation to the building time constant, in the section 3.3. The specific details of how thermal quantities (e.g. solar radiation) are modelled as electrical components in order to assemble an electrical circuit as a building model are discussed in more detail in Ch. 4.

3.2.1 Resistors

Electrical resistors are used to model the thermal resistance to heat transfer between two physical locations at different temperatures. For example, the value of a resistor used to model the thermal resistance of a wall layer of area *(A)*, thickness *(x)* and thermal conductivity *(k)* is given by Eqn. 1 [13]:

$$R_{layer} = \frac{x}{k \cdot A} = \frac{Rvalue}{A} \qquad (1)$$

Resistor component specifications can be static numerical values or dynamic algebraic expressions enabling a resistance to be defined as a function of node voltages or branch currents (temperatures or heat transfer rates). An example of dynamic resistance is conduction resistance modelling based on variable thermal conductivity where the thermal conductivity of physical materials is taken to vary as a function of temperature [13]. A more accurate expression (compared to Eqn. 1) of layer conduction resistance can be specified in Micro-Cap to reflect this as:

$$R_{layer}(t) = \frac{x}{k(T_{layer}(t)) \cdot A} \qquad (2)$$

where R_{layer} is shown to be a function of time due to the dependence on the variable layer conductivity, itself dependent on the layer temperature implemented in Micro-Cap as a voltage: $k(t) = k(V_{layer}(t))$. The expression $k(t)$ can be *any* algebraic function of circuit node voltages from the circuit representation of the layer (e.g. Fig. 3.1). This time-varying computation of layer conduction resistance is not used in this thesis. All conduction resistances are based on static thermal conductivities and computed using Eqn. 1.

A second example of dynamic resistance is a boundary condition: the precise specification of surface radiation resistance between a horizontal surface B with area A *(m^2)*. Eqn. 3 below defines the rate of heat transfer due to radiation between surface *B* and the sky, expressed in the *form* of Ohm's Law [13].

$$\dot{Q}_{radiation} = \varepsilon\sigma A(T_B^4 - T_{sky}^4) = \frac{T_B - T_{sky}}{R_{radiation}} \qquad (3)$$

where T_B and T_{sky} are the temperatures of surface B and the sky in Kelvin, ε is the emissivity of surface B and σ is the *Stefan-Boltzmann* constant *($\sigma = 5.670 \times 10^{-8}$ W/$m^2 \cdot K^4$)*. The resistance between surface B and the sky due to radiative heat transfer is then defined as [13]:

$$R_{radiation} = \frac{1}{\varepsilon\sigma A(T_B^2 + T_{sky}^2)(T_B + T_{sky})} \qquad (4)$$

For *$A = 50m^2$*, Eqn. 4 is entered as an expression defining a surface resistor component in Micro-Cap as:

*1/(50*0.9*5.67E-8*((V(B)+273.16)^2 + (V(Sky)+273.16)^2)*(V(B)+273.16+V(Sky)+273.16))*   (5)

Note that by using Eqn. 4, the computation of radiative heat transfer between outer surfaces and the sky retains the physically accurate non-linear relationship as opposed to the *linear*

radiation heat transfer coefficient ($h_{radiation}$) commonly used for *approximate* computations of $\dot{Q}_{radiation}$ [13].

Ventilation and infiltration are also modelled as a resistance. For example, if the infiltration rate is known to be *ach* (air changes per hour) then the resistor value is given by Eqn. 6 [41]:

$$R_{infiltration} = \frac{3600}{Vol \cdot \rho \cdot ach \cdot c_p} \tag{6}$$

where *Vol* (m^3) is the indoor volume of the room/building, ρ (kg/m^3) is the air density and c_p (J/kg·°C) the specific heat of air at constant pressure [41]. This resistance is placed between the indoor air node and the outdoor air node in parallel with other resistances (e.g. walls) between these two points. Ventilation and infiltration can be thought of as a heat transfer rate between indoors and outdoors based on the air change rate and the indoor and outdoor air temperature difference. An example of a ventilation resistance component is given in Chapter 4.

3.2.2 Capacitors

Electrical capacitors are used to model the thermal capacitance of a building element such as a wall layer. Because the unit of *modelled* time (t_h) is hours and the unit of *real* time (t_s) is seconds, the thermal capacitance of an element is reduced by a factor of 3600 in order for the *real* rate of heat transfer to be computed using modelled time units (hours). The derivation of this scaling is shown below.

$$\dot{Q} = C \frac{dT}{dt_s} \quad \text{with} \quad t_s = t_h \cdot 3600 \quad \text{and} \quad \frac{dt_h}{dt_s} = \frac{1}{3600} \quad \text{we have}$$

$$\dot{Q} = C \frac{dT}{dt_s} = C \frac{dT}{dt_h} \frac{dt_h}{dt_s} = C \frac{dT}{dt_h} \cdot \frac{1}{3600} = \frac{C}{3600} \cdot \frac{dT}{dt_h} \tag{7}$$

This scaling is chosen since climate data usually consists of hourly values and the timescale of interest for building energy simulation is hours. Examples of typical hourly climate data are outdoor temperature, wind speed/direction and solar radiation. Scaling in this manner (1 second *real* time = 1 hour *modelled* time) also results in minimum data changes: only capacitance values are modified (as shown in Eqn. 7). Numerical output from Micro-Cap is not changed, but interpreted as occurring over hours instead of seconds. Without this scaling, all time coordinates of time-varying input and output data would need to be adjusted. For example, a yearly span of hourly solar irradiance input data would need to have the time coordinate changed from: *0, 1, 2, ... 8760 (365 $\times$ 24 hours)* to: *0, 3600, 7200, ... 31 536 000 (seconds).*

The scaled electrical capacitance value used to model a wall layer of area A (m^2), thickness x (m) and made of material with density ρ (kg/m^3) and specific heat c_p (J/kg·°C) is given by Eqn. 8 [14]:

$$C_{layer} = A \cdot x \cdot \rho \cdot c_p / 3600 \qquad\qquad (8)$$

3.2.3 Voltage Source

A voltage source is primarily used to implement a temperature source such as outdoor temperature defined in a weather data file (e.g. IWEC [55]). The Celsius values are used as Volt values with no numerical conversion. A yearly span of hourly temperature values translates into a varying voltage signal defined by $24 \times 365 = 8760$ points with the time coordinate of simulation output interpreted as hours. In general, a voltage source can be a series of *any* values varying over time and need not be feeding a signal (voltage) *directly* into the circuit model. A voltage source can be referenced by a second component such as a resistor, resulting in the resistance value being a user-defined function of the voltage at each time step. For example, the outer surface resistance of a wall or window is dependent on wind speed and direction. This dependency is modelled by the window surface resistance value being a function of a voltage source. The voltage source itself is a user defined data sequence of hourly values that are a function of wind speed, wind direction and surface orientation. In this case, the voltage source is *not* functioning as a temperature source but as a source of hourly values that the varying surface resistance is based on.

3.2.4 Current Source

A current source is used to model the rate of heat transfer from sources such as solar radiation, heating or internal gains. Heat transfer rate values (W or W/m^2) are used directly as Ampere values in a current source connected to the appropriate node in an electric circuit. Like all electrical components, the value of a current source can be a time varying signal, the value of which, at each time step, is based on a node voltage or voltage source value. Such a current source can be used to define a heater as shown in the circuit fragment of Figure 3.2 below. The component value of the heater current source is a function of the difference between a wall *surface* node voltage and a *setpoint* node voltage, mimicking a temperature sensor and setpoint temperature.
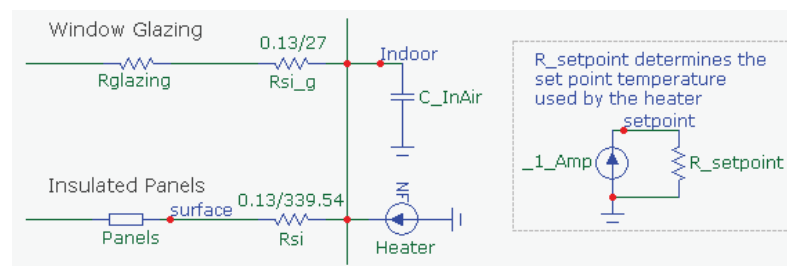
Figure 3.2: Circuit Fragment With Heater Component Defined in Terms of *surface* and *setpoint* Node Voltages

More details of this heater implementation are given in section 4.3.7.

Example Thermal Circuit
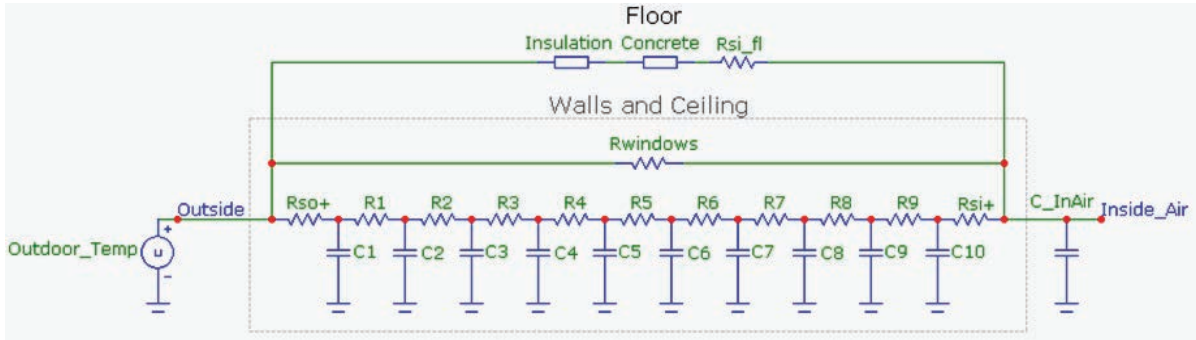
Figure 3.3: Example Thermal Circuit Model of a Single Zone House

Figure 3.3 above illustrates a thermal circuit implemented as an electric circuit in Micro-Cap. The 10th order RC ladder representation of the (lumped) single layer walls and ceiling is explicitly shown while the ladder representations of the insulation and concrete floor layers are encapsulated in a "macro" which can be expanded. A sequence of hourly outdoor temperature values define the voltage source *(Outdoor_Temp)* driving the circuit. Solar input is not included in this circuit.

3.3 RC Circuit Time Constant

Well established electric circuit theory [82] includes detailed analysis of simple resistor-capacitor (RC) circuits: for example, a single resistor with a capacitor in series (Fig. 3.4), charging or discharging from an initial to a final capacitor voltage level. For this simple electric circuit, $\tau = RC$ is the circuit time constant and this characterizes the rate at which voltage across the capacitor grows or decays in response to an input voltage step change.
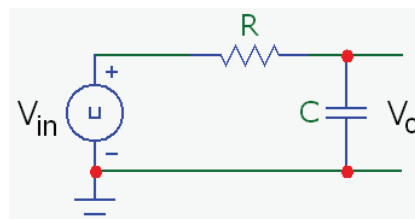
Figure 3.4: A Simple RC circuit

The electrical analogy of RC circuits can be applied to a building thermal circuit model: the indoor air temperature response can be estimated based on a step change in outdoor temperature. Modelling in this manner assumes that a building responds like an aggregate capacitance (lumped) with thermal resistance between the indoor and outdoor air. There are many calculation procedures for the building time constant *(τ)* of varying complexity as discussed in the previous chapter. The simplest is analogous to $\tau = RC$ of an electrical RC circuit (Fig. 3.4): the product of the net thermal resistance R_T, between indoor and outdoor air and the lumped thermal capacitance, C_T (see section 6.1).

Electric circuit theory [82] provides a further technique (shown below) for computing τ of a circuit assumed to behave like a simple RC circuit, based on the Bode plot of the *magnitude transfer function |H(f)|* of a circuit.

$$|H(f)| = \left|\frac{T_{indoor}}{T_{outdoor}}\right| = \frac{1}{\sqrt{1+\left(f\middle/f_B\right)^2}} \qquad \text{where} \quad f_B = \frac{1}{2\pi\tau} \quad \text{and} \quad \tau = \frac{1}{2\pi f_B} \qquad (9)$$

Eqn. 9 is expressed in terms of temperatures, whilst *|H(f)|* of an electric circuit is computed from voltages. Bode plots are graphs illustrating the frequency response of a circuit, with *|H(f)|* plotted on the vertical axis and f plotted on the horizontal axis. The frequency $f = f_B$, where $|H(f_B)| = 1/\sqrt{2} \approx 0.707$, can be found on the Bode plot by identifying the frequency where $T_{indoor} = 0.707 \times T_{outdoor}$. The value of τ is then determined from f_B using Eqn. 9.

Independent of the building time constant, the Bode plot of a circuit model is a useful tool for thermal analysis providing the frequency response of the building in graphical form. Bode plots can be generated for any circuit models (*not* only circuits assumed to behave like simple RC circuits: Fig 3.4) and can illustrate the degree of thermal inertia of a building in response to a wide spectrum of outdoor temperature changes. As an example of this approach, Bode plots generated by Micro-Cap from the building circuit model of a low energy house and the corresponding computations of the building time constant are presented in Chapter 5.

3.4 Discussion

In terms of the categories of building thermal modelling previously described in Ch. 2, this methodology is a variation of the Finite Difference Method but can be seen as sharing features of the Lumped Model method. The Micro-Cap simulation engine ensures energy balance relationships are maintained since these are a by-product of electric circuit modelling according to Kirchhoff's current and voltage laws. A description of how this methodology solves Eqns. 2.1. and 2.2 using the Finite Difference Method was given at the start of this Chapter. This methodology is related to the Lumped Model method in that the degree of accuracy of a circuit model representation is *chosen* by the user. All of the lumped models cited in Chapter 2 can be implemented and solved using Micro-Cap. The degree of lumping of building elements is chosen by the user. This is further discussed in Chapter 4

Modelling with electric circuits can accommodate *any* boundary condition including user-defined time-series of numerical values as well as algebraic functions of dynamic circuit node values. These functions include a wide range of non-linear functions defined, for example, in terms of node values representing indoor air temperatures, wall layer temperatures at chosen layer depths or heat transfer rates. This contrasts with other Response Functions methods that include restrictions or assumptions involving boundary conditions. For example, the Admittance Method assumes that indoor and outdoor

temperature variations are sinusoidal with a 24 h period [10]. A second example is the common simplification of assuming static surface resistances (especially common in Lumped Models).

The ability to specifying circuit component values in terms of algebraic functions of any circuit node voltage (temperature), current (heat transfer rate) and the time variable *(t)* is a very powerful and elegant attribute of this modelling methodology using Micro-Cap. The "exact" dynamic representation of outer surface resistance due to heat transfer exchange between a surface and the sky as shown in Eqn. 4 is made possible due to this functionality. Heating/cooling load computations briefly discussed here and described in detail in the chapters that follow, are also based on this functionality. An example of modelling scheduled ventilation based on this functionality is given in section 4.3.5.

In terms of encouraging an understanding of Building Physics, this methodology profits from the fact that the differential equations underpinning the relationships over time between temperature and rate of heat transfer throughout a circuit model are solved *directly* from the circuit diagram. This enables the user to focus on the thermal circuit, heat flow paths and the physical relationships governing heat balance at each node (e.g. Eqn. 4).

A second aspect of this modelling methodology that encourages a understanding of building physics is due to the generic nature of Micro-Cap as a simulation engine. This program makes no assumptions or decisions for the user in terms of thermal modelling. The user has complete control over the accuracy and detail of the thermal model and must decide how each building and environmental component is modelled. This results in a transparent modelling process unlike modelling using building simulation programs employing the modelling techniques discussed in Chapter 2, but also this requires the user to pre-process some environmental and building material data into a form that can be integrated into a circuit model. This pre-processing is typically implemented in a spreadsheet.

This flexibility enables a user to build up the complexity of a model in stages, from a Lumped Model that includes many simplifications. Complexity can be added component-by-component in a straightforward manner and the implications of a step change of increased complexity can be analysed (e.g.: a change from static outer surface resistances to Eqn. 4).

Finally, the electrical analogy that underpins this methodology is direct and concise. The concept of "Sol-air" temperature is not required. Although the use of Sol-air temperature usually results in correct heating and cooling load computations, the concept does not help to illuminate Building Physics. Mapping solar heat transfer into an "equivalent" outdoor temperature blurs the fundamental physical distinction between temperature and energy. Like all heat sources, solar radiation incident on a surface or transmitted through glazing is represented as a current source in a thermal circuit model using this methodology.

4 Thermal Modelling of a House Using Electric Circuits, Micro-Cap

The aim of the next three chapters is to show by example, the soundness of thermal modelling using electric circuit simulation and Micro-Cap, a commercial electric circuit solver program. In doing so, the accuracy, flexibility, transparency and user-control of this modelling methodology is made apparent.

In this chapter, the thermal modelling of a building using this methodology is presented in detail. A single zone, *low energy* house in Sydney is modelled using electric circuits and Micro-Cap generating thermal simulation results which are compared to the equivalent model implemented using a commercial building simulation program (IDA ICE [64], herein referred to as the *IDA model*). The starting point is the IDA model and simulation results. An electric circuit model is assembled, based on information extracted from the IDA model in order to produce simulation results that are compared to the original IDA results. Using the same climatic inputs, boundary conditions and modelling assumptions, the two models should produce similar simulation results. Here, the electric circuit model is constructed to mimic the original IDA model and the resulting circuit model inherits good and bad modelling assumptions made by the IDA model. In Chapter 5, some circuit components of the electric circuit model are modified to produce a "better" circuit model that is used to perform thermal simulations to investigate the thermal performance of the house.

Two points concerning the model construction and comparison are worth making. Firstly, at every step in the circuit model development, a simpler, more approximate (or complex) approach/calculation could have easily been incorporated into the model. Micro-Cap does not impose practical limitations on the accuracy of a thermal simulation model and enables the user to integrate new modelling techniques or building element representation into an existing circuit in a straightforward manner. The latter flexibility is illustrated in Chapter 5.

Secondly, access to the IDA model was limited: (i) only simulation results in the form of indoor temperature sequences were available (heating and cooling loads were not available) and (ii) physical assumptions and parameter values forming the basis of how IDA models ventilation/infiltration and solar radiation were not known. In general, IDA engineering support and reference documentation was not available while some modelling details were either available in a building physical property summary (similar to Appendix D) or gleaned from the Fortran computer source code of the IDA model. This makes the model comparison non-transparent in terms of ventilation/infiltration and solar radiation modelling.

In summary, a Micro-Cap circuit model of the low energy house is developed in order to:

(i) provide evidence that a circuit model is able to generate simulation results that are comparable to a commercial building simulation program

(ii) illustrate how to construct a circuit-based simulation model of a building

4.1 Modelling Example: a Low Energy House in Sydney

The building modelled here is one of the variations of a low energy house design considered by Bambrook et al in their analysis [83] of the low energy house concept for the Sydney climate. The modelling in this study was done using the building energy simulation program IDA ICE [64] and simulation output from this program is compared to the output of the equivalent electric circuit model presented in this chapter. The climate data used in the IDA ICE simulations and all circuit-based simulations is Sydney IWEC climate data (International Weather for Energy Calculations) [55].

The single zone house with 201 m^2 floor area is located in Sydney (latitude 33.86° S and longitude 151.21° E) and oriented North. The North and South facing walls are 56 m^2, each including a 15 m^2 and 7 m^2 double-glazed window respectively. The East and West walls are both 28.2 m^2, each including a 4 m^2 double-glazed window. All window areas include 10% window frame areas. The roof is flat and contains no glazing. The house is unobstructed and fully exposed to solar insolation and there are no blinds or shading devices associated with the windows. The walls and roof of the house are comprised of the same structural insulated panels consisting of thin steel outer layers sandwiching rigid insulation with R-value 6.25. The floor is comprised of a heavy concrete layer (150 mm) followed by rigid insulation (R-value 6.5). These layers are followed by a very heavy soil layer (500 mm) and a ground insulation layer (R-value 2.8) which is an attempt to model the thermal properties of the ground. During close inspection of the input parameters to IDA simulations, it was discovered that the ground insulation layer property values input to IDA were incorrect, resulting in this layer having no capacitance and a lower R-value. Disregarding the question of accuracy, the IDA simulation output was based on these incorrect values and therefore these values were used unchanged in the equivalent circuit model, in order to make a fair comparison.

Appendix D contains a complete listing of the construction element properties of the low energy house modelled using IDA ICE and using electric circuits and Micro-Cap.

4.2 The Equivalent Micro-Cap Circuit Model of the IDA ICE Model

The Micro-Cap circuit model of the low energy house as implemented in the IDA simulation program is shown in Figure 4.1 below. This circuit is used for both simulations that include and exclude solar radiation input. To exclude solar radiation, the three circuit elements modelling solar input *(Irradiance_Frames, Irradiance_SIP, SolarHeatGainFlux_Glazing)* are disabled by simple point and click commands made before running a simulation. The details of this circuit are discussed at length in the section 4.3. Some observations about the circuit modelling interface compared to a commercial building simulation program can be made at this point. The interface is almost identical to thermal circuit diagrams used in standard thermal modelling. Only the current symbol (representing a modelled heat source) is different from the standard heat source symbol of a thermal circuit. Circuit component values (e.g. resistances) can be displayed, although in Fig 4.1, most are not displayed in

order to avoid cluttering the diagram. This diagram not only illustrates the heat flow paths between indoors and outdoors, but also component values (such as the infiltration resistance) explicitly indicate the modelling equation and values used in the calculation. This contrasts the common difficulty of determining building element values and physical relationships (equations) in order to understand the thermal relationships of a building modelled using commercial building simulation software. Circuit components (e.g. resistors, capacitors) can be bundled into "Macros" (generic groups) such as the floor layers shown in Fig 4.1. This enables the user to assemble a model from complex representations of building elements (e.g. walls) while maintaining a relatively simple view of the complete building model. If heat flows or temperature readings from within a building element are required, the user is able to monitor nodes within a macro component. For example, the voltage at the 5th node of a 15th order RC ladder representation of a wall layer can be monitored giving temperature readings over a period of time, of the interior of the wall layer at a depth of 1/3 the wall layer thickness.

Although more physical information is readily available from a circuit model such as Fig. 4.1 (compared to commercial software) not *all* the information can be made available *directly* from a circuit diagram. Hourly climate data driving simulations is not displayed in the circuit diagram but resides in a locally accessible file. For example, in Fig. 4.1 the hourly temperature and wind sequences are data files containing numerical values. In the case of hourly temperature data *(Outdoor_Temp)* this is not significant since the values are taken *directly* from the publicly available weather data files [55]. In the case of hourly varying wind-based convection coefficients, these are a function of surface orientation and the raw wind speed and direction data taken from a weather data file. The computation of the yearly sequence of convection coefficients is made using a spreadsheet implementing Clarke's wind model [20] and transferred to a Micro-Cap data file read by the simulation engine. Solar data is integrated into a circuit model in the same manner. Wind and Solar data pre-processing are discussed in the following section.
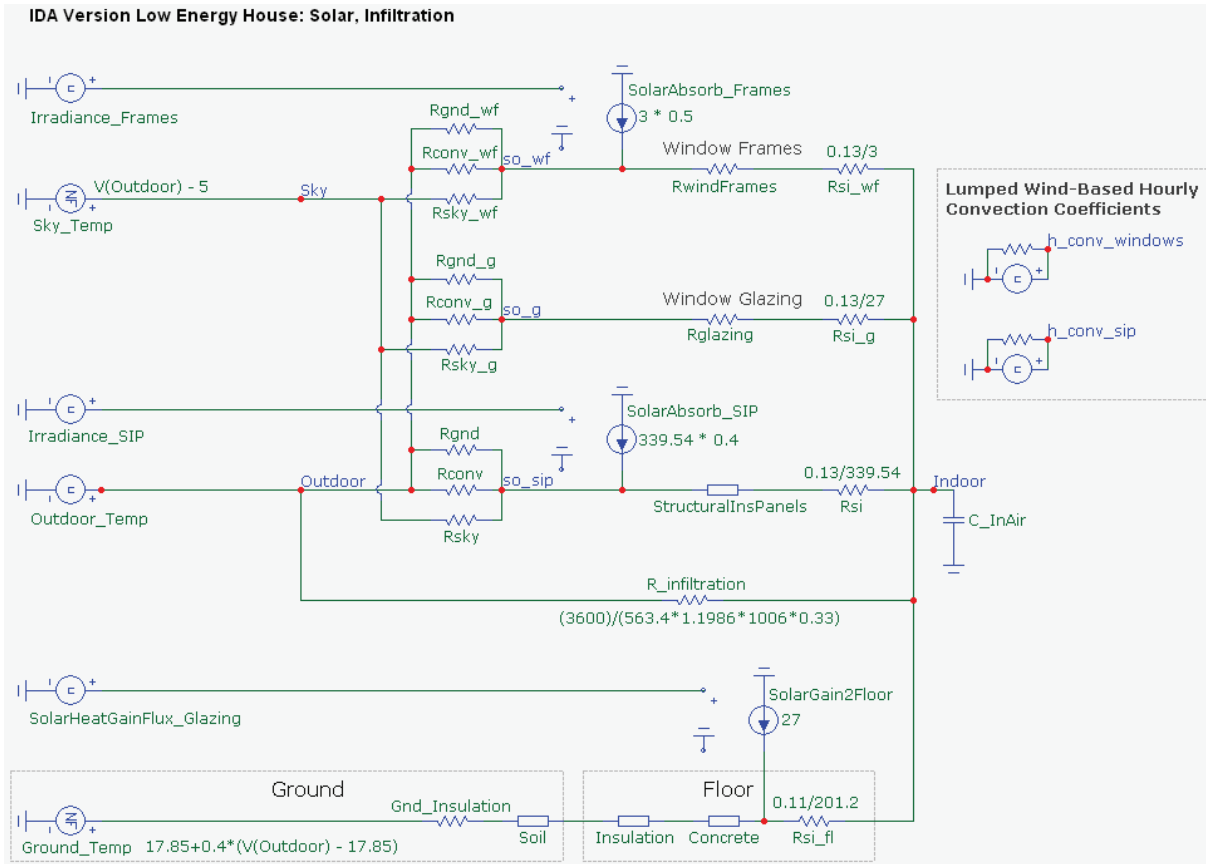
Figure 4.1: Circuit Model of the Low Energy House as Modelled in IDA with Solar radiation Input

4.3 Assembling the Micro-Cap Circuit Model

In this section the equivalent circuit model (Fig 4.1) of the IDA model of the low energy house is described in detail including the integration of solar radiation into the circuit model. Simulation output from the above circuit is compared to output of the equivalent IDA model and presented in section 4.4.

4.3.1 Walls, Floor and Ceiling

The RC ladder representation of the thermal capacitance and resistance of a building layer forms the basis for modelling one-dimensional heat flows through the walls, floor and ceiling of the low energy house, using the Finite Difference Method. RC ladders model the thickness of a layer and thereby provide a discrete solution to the heat diffusion equation (Eqn. 2.2) in terms of the spatial variable *(x)* at various positions within the layer depth, based on the length (order) of the RC ladder (discussed in section 3.1). Micro-Cap solves the resulting differential equations (derived from the circuits) with respect to time (*t*).

The aim of using an accurate RC ladder is not *necessarily* to determine temperature readings at depths throughout a layer, although this is achieved. A more common aim is to accurately solve for the indoor temperature at any time (*t*) taking into account heat transfer lag times through the envelope. Hence, having an accurate solution of heat diffusion through a layer in terms of the spatial variable (x : layer thickness) contributes to the accuracy of calculated

temperature sequences in time for (i) either boundary of the element (e.g. inner surface of a wall) and (ii) the indoor air.

An example of a ladder representation is the floor shown in Fig. 4.2 (an extract from Fig. 4.1). This floor consists of a concrete slab layer followed by a floor insulation layer. Each of these layers is represented by an RC ladder and the complete floor is modelled as a concatenation of these layers as shown below:
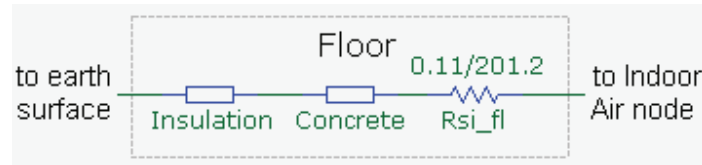
Figure 4.2: Representation of the two Floor Layers of the Low Energy House in Micro-Cap

The rectangles in the above diagram are Micro-Cap macro encapsulations of the RC ladder representation of the layer. These are easily expanded from the main circuit diagram. For example, the expansion of the Concrete layer is a 15th order RC ladder shown in Figure 4.3.
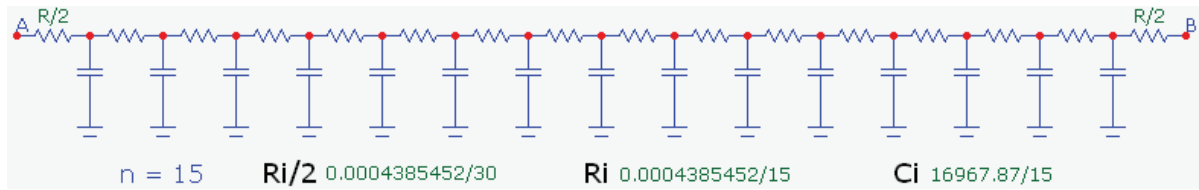
Figure 4.3: Macro Expansion of the Floor Concrete Layer showing the 15th Order RC ladder Representation

In Fig 4.3, $R_i = R_t/n$, $C_i = C_t/n$ and $n = 15$ and where R_t and C_t are the total thermal resistance and capacitance of the layer (concrete).

Order Of RC ladder Representations
The order of an RC ladder representation of a layer is the number (n) of resistor and capacitor pairs making up the ladder. As n increases, the accuracy of the modelling of heat diffusion through the layer improves and approaches the "exact" solution to the heat diffusion equation of the equivalent homogenous slab [9]. This is the basis of the computation of the "error" due to modelling a layer using an nth order RC ladder. A detailed description of a function that evaluates this error *(err)* is given in Appendix A. In addition to n, R_t and C_t, the error evaluation also depends on the period P (inverse of frequency) of both the temperature and heat flux variations required to be modelled. A further discussion and a progression of computations of *err* for increasing orders of RC representation of the Concrete layer of Fig. 4.3 are given in Appendix A.

This error function *(err)* is used to choose n for each layer of the envelope. The target error was 1% for temperature and heat flux variations with period $P = 12\ h$ except for the soil layer which due to a large capacitance value required employing $n = 26$ for a 1% error at $P = 20\ h$.

The order of the RC ladder representation of each layer and the corresponding period P resulting in 1% error is shown in Appendices D and E. Window glazing and frames are modelled in IDA having no thermal capacitance and each were represented as a single lumped resistance for the circuit equivalent and all subsequent circuit models. The steel layers of the structural insulated panels have a very high thermal conductivity allowing the three layers of the structural insulated panels to be modelled as one layer and represented as a single 21st-order ladder. Derivations of all circuit component values of the low energy house model are shown in Appendices D and E. Any *practical* value of n can be chosen for the RC ladder representation of a building layer: Micro-Cap does not impose a limit on n.

4.3.2 Lumping Building Elements

The four walls and the ceiling of the low energy house are constructed from exactly the same materials: structural insulated panels consisting of a layer of rigid insulation sandwiched between two thin layers of steel. This provides the opportunity of lumping the four walls and ceiling into one *lumped wall* separating the indoor air from the outdoor air. Each climatic input (solar, wind) is applied to this one lumped wall surface as one circuit component defined as a (area) weighted summation of the climate data at each orientation. The weighted sum is computed in a spreadsheet and the resulting single yearly numerical sequence is used to define the one climate circuit component. In Appendix F it is shown that this strategy produces equivalent simulation results to the distributed (unlumped) circuit. That is, this lumping stragegy does *not* introduce modelling approximations to the unlumped circuit. This contrasts with the inaccuracies produced by the more extreme lumping and simplifications of the *Lumped Models* described in section 2.1.4.

One drawback is that this lumping removes the ability to generate modelling output related to heat flow paths of specific orientations. For example, it is not possible to determine how much solar radiation enters the house via the east window or wall. Since the analysis of this thesis is only aimed at observations about the indoor temperature and energy consumption of the house, this shortcoming has no impact. As is common practice [13], both the lumped and unlumped circuits combine the inner surface convection and radiative heat transfer coefficients into one static surface resistance (R_{si} in Fig. 4.1), replicating the treatment of inner surface resistances of the IDA model. A more detailed model of these surface resistances, including longwave radiant heat transfer between indoor surfaces (for example: Athienitis et al [36]) can be implemented in the unlumped circuit model (Fig. I.1, Appendix I) but not in the lumped circuit model.

As the four window frames and glazing are also made from the same materials, this lumping strategy was also employed for the window frames and glazing. This lumping has the advantage of reducing the number of heat flow paths between indoors and outdoors. Referring to the indoor air node of Fig. I.1 (Appendix I) and Fig. 4.1 above, the number of heat flow paths between indoors and outdoors is reduced from:

38

5 (SIPs) + 2·4 (window frames, glazing) + 2 (ground, infiltration) = 15 to
3 (lumped SIPs, window frames, glazing) + 2 (ground, infiltration) = 5

Note that these path-counts treat the three parallel outer surface resistance branches of the house envelope as one path.

Circuit component numbers are reduced to a further extent due to multiple components on each path. This makes the lumped circuit significantly easier to understand and modify than the equivalent distributed circuit. This can be seen by comparing the lumped version of the "Reference" circuit shown in Fig. 5.3 (described in Ch. 5) and the equivalent unlumped version shown in Fig. I.1 of Appendix I. As previously mentioned, radiant exchanges between indoor surfaces *can* be modeled using the unlumped circuit. This would result in *C(6,2) = 15* additional resistor components placed between the 6 inner surface nodes of the unlumped circuit.

All circuits presented in this thesis besides the circuit of Fig. I.1 employ this lumping strategy.

In addition to the lumping of the capacitance and the resistance of the building elements, some pre-processing of orientation-specific wind and solar radiation based data sequences is required. In the case of wind, instead of using hourly surface convection coefficients for each orientation (*N*: north, *E*: east , *S*: south, *W*: west, *H*: horizontal; see Fig. I.1), a lumped hourly convection coefficient sequence is calculated as the *area-weighted* average of the five convection coefficients at each time step *t* (hour). The definition of the lumped convection coefficient of the outer surfaces of the structural insulated panels (SIP) is shown in Eqn. 1 below.

$$h_{conv\_sip}(t) = f_{sip\_N} \cdot h_{windN}(t) + f_{sip\_E} \cdot h_{windE}(t) + f_{sip\_S} \cdot h_{windS}(t) + f_{sip\_W} \cdot h_{windW}(t) + f_{sip\_H} \cdot h_{windH}(t) \ (1)$$

where: $f_{sip\_N} = \dfrac{A_{sip\_N}}{A_{sip\_total}}$, $f_{sip\_E} = \dfrac{A_{sip\_E}}{A_{sip\_total}}$,   etc.

and: $A_{sip\_total} = A_{sip\_N} + A_{sip\_E} + A_{sip\_S} + A_{sip\_W} + A_{sip\_H}$, $f_{sip\_N} + f_{sip\_E} + f_{sip\_S} + f_{sip\_W} + f_{sip\_H} = 1$

Here, A_{sip_N} is the area of the Structural Insulated Panel surface on the Northern wall. Similarly, the lumped convection coefficient of the outer surfaces of both the window glazing and window frames is shown in Eqn. 2 below.

$$h_{conv\_windows}(t) = f_{w\_N} \cdot h_{windN}(t) + f_{w\_E} \cdot h_{windE}(t) + f_{w\_S} \cdot h_{windS}(t) + f_{w\_W} \cdot h_{windW}(t) \qquad (2)$$

where: $f_{w\_N} = \dfrac{A_{w\_N}}{A_{w\_total}}$, $f_{w\_E} = \dfrac{A_{w\_E}}{A_{w\_total}}$,   *etc*

and: $A_{w\_total} = A_{w\_N} + A_{w\_E} + A_{w\_S} + A_{w\_W}$, $f_{w\_N} + f_{w\_E} + f_{w\_S} + f_{w\_W} = 1$

In Eqn. 2, A_{w_N} is the window area on the Northern wall and there are no skylights. In both Eqns. 1 and 2, the hourly convection coefficient sequence for each orientation (e.g. $h_{windN}(t)$ for the Northern wall) is derived from an algorithm by Clarke [20]. The algorithm computes the coefficient at each hour as a function of the corresponding surface orientation, wind speed and wind direction with the latter two sequences taken from the climate data file. This is the same approach implemented in the IDA model [84]. The same surface weights for both the Structural Insulated Panel surfaces (f_{sip_x}) and the window surfaces (f_{w_x}) are used to lump irradiance sequences when incorporating solar radiation in the circuit models as described in section 4.3.6.

The convection coefficient sequences (Eqns. 1 and 2) are used for modelling convective heat transfer at the outer envelope surfaces and are further discussed in *Surface Boundaries* in section 4.3.4 below.

4.3.3 Temperature Sources

From the Sydney IWEC weather file, hourly outdoor temperature values spanning a year make up the numerical temperature sequence defining the outdoor temperature (voltage) source component of the circuit model.

A sky temperature (voltage) source is also employed for modelling radiative heat exchange between outer surfaces and the sky as specified below. The IDA model of the low energy house represents the sky temperature as five degrees below outdoor temperature [84]:

$$T_{sky}(t) \ = \ T_{outdoor}(t) - 5 \tag{3}$$

For radiative heat exchange between the outer wall surfaces and the ground, ground temperature is taken to be equal to outdoor temperature [84]:

$$T_{ground\_rad}(t) \ = \ T_{outdoor}(t) \tag{4}$$

The IDA model represents ground temperature as a damped equivalent of the hourly outdoor temperature sequence when modelling ground conduction [84]:

$$T_{ground\_cond}(t) \ = \ T_{out\_avg\_yr} + \ 0.4 \cdot (T_{outdoor}(t) - T_{out\_avg\_yr}) \tag{5}$$

Both of these temperature sequences (Eqns. 3 and 5) are implemented in Micro-Cap as "Function Sources" (NFV) with values defined in terms of the outdoor temperature value at each time step t, according to the above specifications.

4.3.4 Surface Boundaries

Inner surface resistances are static values based on a floor R-value of 0.11 $m^2.°C/W$ and R-values of 0.13 $m^2.°C/W$ for window glazing and frames specified by IDA [85] and consistent with Cengel [13]. The floor R-value is a compromise between the R-value listed in the DesignBuilder [86] materials database (0.10) and the value (0.13) suggested by Cengel [13].

40

Outer surface resistances are dynamic (calculated at each time step) and are based on three parallel heat transfer paths between the outer surfaces and outside environment. The heat transfer coefficient for each path and corresponding surface resistance symbol is shown in Table 4.1 with emissivity $\varepsilon = 0.9$ and the *Stefan-Boltzmann* constant $\sigma = 5.67 \times 10^{-8}$ $W/m^2.K^4$.

Heat Transfer Coefficient	Circuit Formula	Component
Convection: Wind-Based	$h_{conv\_}(t)$	$R_{conv\_}$
Radiation: Ground	$h_{gnd\_}(t) = \varepsilon\sigma(T_{so}^2(t) + T_{outdoor}^2(t))(T_{so}(t) + T_{outdoor}(t))$	$R_{gnd\_}$
Radiation: Sky	$h_{sky\_}(t) = \varepsilon\sigma(T_{so}^2(t) + T_{sky}^2(t))(T_{so}(t) + T_{sky}(t))$	$R_{sky\_}$

Table 4.1: Dynamic Outer Surface Heat Transfer Coefficients; Corresponding Surface Resistance Prefix [13, 84]

In the case of surface to ground radiative heat transfer, ground temperature is taken to be equal to ambient temperature *($T_{outdoor}$)* as specified by the IDA model.

Outer Surface Convection Resistance ($R_{conv\_}$)

A wind-based convection coefficient sequence is derived for each orientation based on orientation and hourly wind speed and direction values from the Sydney IWEC climate data file, using an algorithm specified by Clarke [20]. These hourly values are combined (using a spreadsheet) into one lumped convection coefficient sequence based on Eqns. 1 and 2 to specify the convective heat transfer at the outer surfaces of (i) the structural insulated panels (walls, ceiling): $h_{conv\_sip}(t)$ and (ii) the windows: $h_{conv\_windows}(t)$. Window frame and glazing surfaces have the same convection coefficient sequence, since the total frame and glazing area is distributed amongst the four orientations in exactly the same ratios: frames and glazing have the same f_{w_N}, f_{w_E}, f_{w_S} and f_{w_W} values from Eqn. 2 (for all windows, the frame area is 10% of total window area). Lumped dynamic convection resistances are derived from convection coefficients as shown in Table 4.2.

Surface	Convection Resistance
Structural Insulated Panels	$R_{conv}(t) = \dfrac{1}{A_{sip\_total} \cdot h_{conv\_sip}(t)}$
Window Frames	$R_{conv\_wf}(t) = \dfrac{1}{A_{wf\_total} \cdot h_{conv\_windows}(t)}$
Window Glazing	$R_{conv\_g}(t) = \dfrac{1}{A_{g\_total} \cdot h_{conv\_windows}(t)}$

Table 4.2: Outer Surface Convection Resistance Definitions for 3 Surface Types of the Low Energy House [13]

Outer Surface Radiation Resistance ($R_{gnd\_}, R_{sky\_}$)

The radiation heat transfer coefficients shown in Table 4.1 are listed in terms of temperatures at circuit nodes. These node temperatures are dynamic hourly temperatures (e.g. $T_{so}(t)$) is the outer surface temperature at hour *t* during a simulation). This illustrates

one of the strengths of the SPICE circuit modelling language: resistance and voltage (temperature) values can be defined in terms of other node voltages (temperatures) at each time step. This enables an exact expression, as opposed to a linear approximation, to be defined for surface radiation resistance.

The lumping of radiation surface resistances is achieved in a similar manner to the lumping of convection surface resistances just described. For convective resistance, a lumped convective heat transfer coefficient is computed as an area-weighted average of externally computed (spreadsheet) convection coefficients for each orientation as shown in Eqns. 1 and 2. For radiative resistance, the dependence on surface orientation is simpler and does not require the computation of individual radiation coefficients at each orientation. The relationship between radiative resistance and surface orientation is based on time-invariant view factors ($F_{sky\text{-}surface}$, $F_{ground\text{-}surface}$) that are easily computed for sky and ground radiative exchange at each orientation as shown below in Eqns. 6 through 9 [63].

$$F_{sky\text{-}surface} \ = \ (1 + cos(\theta_{tilt}))/2, \qquad\qquad F_{ground\text{-}surface} \ = \ (1 - cos(\theta_{tilt}))/2 \qquad (6)$$

where θ_{tilt} is the angle between the surface and the horizontal.
For the four vertical surfaces: $\quad \theta_{tilt} = \ 90° \qquad$ and
for the flat ceiling/roof: $\qquad \theta_{tilt} = \ 0° \qquad\qquad\qquad\qquad\qquad\qquad (7)$

Resulting in *equal* view factors for the four orientations of the window glazing and window frame surfaces:

$$F_{sky\text{-}glazing} \ = \ F_{sky\text{-}w.frames} \ = \ F_{ground\text{-}glazing} \ = \ F_{ground\text{-}w.frames} \ = \ 1/2 \qquad (8)$$

As above, the view factors for the structural insulated panels along the four vertical surfaces are ½, while the view factors for the ceiling/roof are:

$$F_{sky\text{-}roof} \ = \ 1 \ \text{ and } \ F_{ground\text{-}roof} \ = \ 0 \qquad\qquad\qquad\qquad\qquad (9)$$

These view factors change the *effective* area involved in the radiative heat exchange and therefore impact the total lumped effected area used in the lumped surface resistance formulas. The lumped radiative surface resistances formulas, based on lumped effective area and the radiative heat transfer coefficients of Table 4.1, are shown in Table 4.3 below.

Surface	Ground ↔ Surface	Sky ↔ Surface
SIP	$R_{gnd}(t) = \dfrac{1}{\sum\limits_{x=N,E,S,W} 0.5 \cdot A_{sip\_x} \cdot h_{gnd\_sip}(t)}$	$R_{sky}(t) = \dfrac{1}{(A_{sip\_H} + \sum\limits_{x=N,E,S,W} 0.5 \cdot A_{sip\_x}) \cdot h_{sky\_sip}(t)}$
Window Frames	$R_{gnd\_wf}(t) = \dfrac{1}{0.5 A_{wf\_total} \cdot h_{gnd\_wf}(t)}$	$R_{sky\_wf}(t) = \dfrac{1}{0.5 A_{wf\_total} \cdot h_{sky\_wf}(t)}$
Window Glazing	$R_{gnd\_g}(t) = \dfrac{1}{0.5 A_{g\_total} \cdot h_{gnd\_g}(t)}$	$R_{sky\_g}(t) = \dfrac{1}{0.5 A_{g\_total} \cdot h_{sky\_g}(t)}$

Table 4.3: Outer Surface Radiation Resistance Definitions for Three Surface Types of the Low Energy House [84]

Surface convection and radiative heat transfer coefficients are commonly estimated as static values and consolidated into a single static *combined* heat transfer coefficient [13]. The dynamic modelling of surface resistances presented here illustrates the flexibility and accuracy potential of Micro-Cap that enables the user to choose the degree of accuracy of the model implementation. This derivation of outer surface resistances *exactly* replicates the implementation of these resistances in the IDA model of the low energy house [84].

4.3.5 Ventilation and Infiltration

Both ventilation and infiltration involve the exchange of "new" air with indoor air. The new air can be either *untreated* outdoor air as is the case for infiltration or the outdoor air *can* be treated (e.g. heated) before being introduced to the indoors, as is the case for ventilation. Infiltration can be thought of as untreated uncontrolled/unwanted ventilation that occurs at a constant rate, 24 hours per day, whereas ventilation is intended and often is not active at the same rate 24 hours per day.

Ventilation and infiltration are represented in a circuit model as individual heat flow paths between indoors and outdoors based on the relative heat content of the air entering the house displacing an equivalent volume of existing indoor air. Infiltration and untreated, constant ventilation are each implemented as a single resistance as described in section 3.2 with the air change rate *(ach)* as one of the parameters in the resistance calculation (Eqn. 3.6). For convenience, this static parameter can be replaced with a reference to a node voltage of a separate minor circuit whose value varies between a low to high air change value. In the infiltration example below, the voltage at node *ach* can vary discretely between 1 and 11 under user-control.
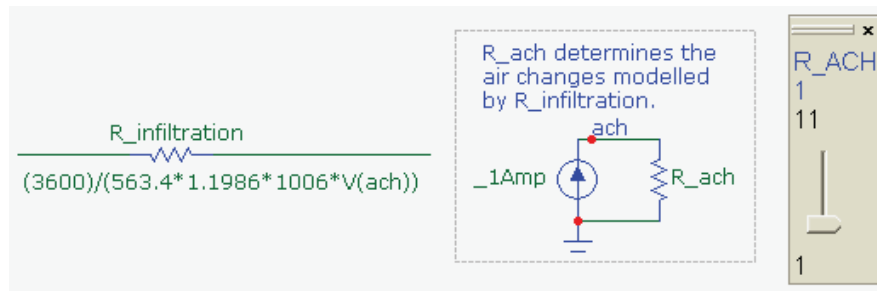
Figure 4.4: Modelling Infiltration Resistance with User-Specifiable Air Change Rate of 1 – 11 ach

In Fig. 4.4, the values shown for the expression of $R_{\_infiltration}$ (Eqn. 3.6), are: $Vol = 563.4\ m^3$, $\rho = 1.1986\ kg/m^3$, $c_p = 1006\ J/kg \cdot °C$ and $ach = V(ach)$. $V(ach)$ can take on the following values: *1,2,3,4,5,6,7,8,9,10,11.*

This example of circuit modelling flexibility shows how the user is able to easily change the modelling scenario (infiltration rate) between simulations and observe the results *without editing* the model.

Ventilation Example

The above expression of $R_{\_infiltration}$ contains two assumptions: (i) the incoming air is untreated outdoor air and (ii) the incoming air is exchanged with the indoor air at a constant rate. This is valid for infiltration, but not generally valid for ventilation. The ventilation example presented here removes the second assumption only: the air exchange does *not* occur at a constant rate while the incoming air remains as *untreated* outdoor air. In order to model *treated* incoming air, the resistance expression in Fig. 4.4 would need to be modified to reflect the temperature difference between the displaced indoor air and the incoming treated air.

The ventilation example is night-time ventilation, active every evening between 8pm and 12am at a rate of 3 ach. When modelling scheduled ventilation, the time variable *(t)* is included in the Micro-Cap expression of the ventilation resistance component. The ventilation resistance equation is shown below in Eqn. 10.

$$R_{night\_ventilation}(t) = \begin{cases} \dfrac{3600}{563.4*1.1986*1006*3} & if \ (t \bmod 24 \geq 20 \ and \ t \bmod 24 < 24) \\ \\ 10^{100} & otherwise \end{cases} \qquad (10)$$

Here, t is the hour number of a simulation, varying between 0 and 8760 for a one year simulation. The upper branch is active during the required time every day and evaluates to 3 ach of infiltration, using the same expression input values as $R_{\_infiltration}$ in Fig. 4.4. The otherwise clause sets the ventilation resistance to 10^{100} Ω, effectively shutting off the ventilation. The ventilation resistance component expression of Eqn. 10 is entered in Micro-Cap as:

IF (t MOD 24 >= 20 AND t MOD 24 < 24) , 3600 / (563.4*1.1986*1006*3), 10^100)

With additional logic, this can be easily modified to restrict the ventilation activation to summertime only.

Ventilation was not implemented in both the IDA and circuit models of the low energy house and is not investigated in this thesis. Infiltration was implemented in the IDA model as well as in the equivalent circuit model and other circuit models presented in this thesis as shown in Fig 4.4 above. Simulation results of circuit models including infiltration modelling at various rates are presented in Chapter 5. The base infiltration rate is taken to be 0.33 ach. The modelling details and assumptions related to the implementation of infiltration in the IDA model was not available. Therefore it is improbable that this implementation of infiltration in circuit models mimics the implementation of infiltration in the original IDA model.

4.3.6 Solar Radiation

The methodology used to incorporate solar radiation into the circuit models of this thesis is based on the simple building simulation tool of Nielsen[18] with some modifications and omissions. As is the case with the modelling of all thermal energy sources in a circuit model, heat transfer from solar radiation is modelled using a current source. One year of hourly direct normal and diffuse horizontal irradiance levels from the Sydney IWEC weather file are the basis from which hourly incident irradiance (W/m^2) levels $(G_{incident,orientation}(t))$ are derived for each orientation of the low energy house envelope *(N, E, S, W, H)*. This derivation takes into account surface orientation, date and time of day (details are given in Appendix B).

The envelope is made up of three surface types with unique solar properties [85] [84]: structural insulated panels (SIP), window frames and window glazing. For each surface-type, an hourly *lumped* incident irradiance data sequence is computed using spreadsheets based on $G_{incident,orientation}(t)$ and the area distribution of the surface type amongst the orientations. This is a weighted average of $G_{incident,orientation}(t)$ at each orientation as employed in the derivation of the lumped wind-based surface convection coefficients (Eqns. 1 and 2). For irradiance weighting, the same weights of Eqns. 1 and 2 are used and these are summarized in table 4.4. This table also includes the definitions of the glazing weights (f_{g_x}) in row 3, used in the derivation of the lumped solar gain through glazing. For example, there are structural insulated panels on the North, East, South, West and Horizontal (roof) orientations of the house. The lumped incident irradiance sequence on the structural insulated panels, shown in the circuit diagram (Fig. 4.1) as *Irradiance_SIP*, is defined as:

$$G_{incident,Lumped\_sip}(t) = f_{sip\_N} \cdot G_{incident,\,N}(t) + f_{sip\_E} \cdot G_{incident,\,E}(t) + f_{sip\_S} \cdot G_{incident,\,S}(t) + f_{sip\_W} \cdot G_{incident,\,W}(t) + f_{sip\_H} \cdot G_{incident,\,H}(t) \qquad (11)$$

where:
$$f_{sip\_N} + f_{sip\_E} + f_{sip\_S} + f_{sip\_W} + f_{sip\_H} = 1$$

and where the weights of Eqn. 11 are defined in the first row of Table 4.4 below.

Surface	North $f_{surface\ N}$	East $f_{surface\ E}$	South $f_{surface\ S}$	West $f_{surface\ W}$	Horizontal $f_{surface\ H}$	Total Area
Structural Insulated Panels	$\dfrac{A_{sip\_N}}{A_{sip\_total}}$	$\dfrac{A_{sip\_E}}{A_{sip\_total}}$	$\dfrac{A_{sip\_S}}{A_{sip\_total}}$	$\dfrac{A_{sip\_W}}{A_{sip\_total}}$	$\dfrac{A_{sip\_H}}{A_{sip\_total}}$	$A_{sip\_total} = \sum\limits_{x\in\{N,E,S,W,H\}} A_{sip\_x}$
Window Frames	$\dfrac{A_{wf\_N}}{A_{wf\_total}}$	$\dfrac{A_{wf\_E}}{A_{wf\_total}}$	$\dfrac{A_{wf\_S}}{A_{wf\_total}}$	$\dfrac{A_{wf\_W}}{A_{wf\_total}}$	----	$A_{wf\_total} = \sum\limits_{x\in\{N,E,S,W\}} A_{wf\_x}$
Glazing	$\dfrac{A_{g\_N}}{A_{g\_total}}$	$\dfrac{A_{g\_E}}{A_{g\_total}}$	$\dfrac{A_{g\_S}}{A_{g\_total}}$	$\dfrac{A_{g\_W}}{A_{g\_total}}$	----	$A_{g\_total} = \sum\limits_{x\in\{N,E,S,W\}} A_{g\_x}$

Table 4.4: Definitions of Surface Weights at Each Orientation for Each Surface Type

The yearly data sequence of hourly values of radiant flux (W) absorbed by the structural insulated panels defines the current component (*SolarAbsorb_SIP* in Fig. 4.5) as [13]:

$$\dot{Q}_{solar\_absorb\_SIP}(t) \quad = \quad G_{incident,Lumped\_sip}(t) \cdot A_{sip\_total} \cdot \alpha_{sip} \qquad \alpha_{sip} = 0.4 \qquad (12)$$

Using a similar derivation, the yearly data sequence of hourly values of radiant flux (W) absorbed by the opaque window frames is defined as [13]:

$$\dot{Q}_{solar\_absorb\_frames}(t) \quad = \quad G_{incident,Lumped\_wf}(t) \cdot A_{wf\_total} \cdot \alpha_{wf} \qquad \alpha_{wf} = 0.5 \qquad (13)$$

where the absorptivities (α) of the two surface types are shown above [84].

The hourly solar gain due to glazing is derived in a similar manner to the incident irradiance of the opaque surfaces. Before making an area-weighted average of solar gain due to glazing at each orientation, a Solar Heat Gain Coefficient is applied to the incident irradiance, resulting in an hourly Solar Heat Gain Flux sequence at each orientation x: $\dot{q}_{solar,gain\_x}(t)$ (W/m^2). Details of the derivation of these sequences are given in Appendix C.

Again, these four Solar Heat Gain Flux sequences due to glazing at each orientation are combined into one lumped Solar Heat Gain flux (W/m^2) as an area-weighted average of each sequence:

$$
\begin{aligned}
\dot{q}_{solar,gain\_lump}(t) = \quad & \dot{q}_{solar,gain\_N}(t) \cdot f_{g\_N} \; + & \text{North} \\
& \dot{q}_{solar,gain\_E}(t) \cdot f_{g\_E} \; + & \text{East} \\
& \dot{q}_{solar,gain\_S}(t) \cdot f_{g\_S} \; + & \text{South} \\
& \dot{q}_{solar,gain\_W}(t) \cdot f_{g\_W} & \text{West} \qquad (14)
\end{aligned}
$$

where each of the weights f_{g_x} is the fraction of the total glazing at orientation x shown in the 3rd row of Table 4.4 above. The above lumped Solar Heat Gain flux sequence defines the *SolarHeatGainFlux_Glazing* circuit component in Fig. 4.1.

The hourly sequence of values forming the basis of the current source component for Solar Heat Gain (W) due to glazing is [13]:

$$\dot{Q}_{solar,gain}(t) \quad = \quad \dot{q}_{solar,gain\_lump}(t) \cdot A_{g\_total} \qquad (15)$$

All of the solar gain transmitted through the glazing is assumed to be absorbed by the floor. This solar heat gain source and the two current sources modelling solar heat absorbed in the opaque envelope are included in the thermal circuit diagrams of the IDA-equivalent circuit model (Fig. 4.1).

User-defined Current Source in Micro-Cap
Micro-Cap does not include a current source component defined from a sequence of current values. Therefore, it is necessary to define a voltage source based on the current value

sequence and use this source to drive a voltage controlled current source ("IofV"). Fig. 4.5 below shows the voltage source *Irradiance_SIP* driving the current source *SolarAbsorb_SIP*. The *Irradiance_SIP* component contains the hourly sequence of lumped irradiance values (W/m^2) for the structual insulated panels (SIP). The *SolarAbsorb_SIP* current source generates the hourly sequence of total Radiant Flux (W) absorbed by all of the SIP and includes multiplication factors of the total area *(A$_{sip\_total}$ = 339.54 m^2)* and the absorptivity *(α_{sip} = 0.4)* of the SIP (see Eqn. 12).
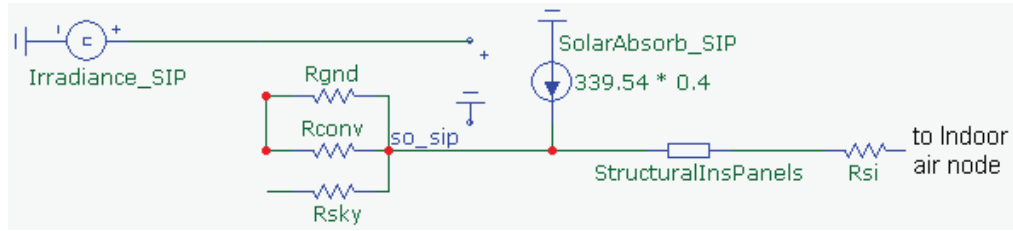
Figure 4.5: Circuit Fragment of the Voltage Controlled Current Source Modelling Incident Irradiance on SIP

The thermal quantity modelled by the current source in Fig. 4.5 is in Watts:

$$\dot{Q}_{solar\_absorb\_SIP}(t) \ = G_{incident,Lumped\_sip}(t) \cdot A_{sip\_total} \cdot \alpha_{sip} \qquad (16)$$

As was the case with infiltration, no documentation pertaining to how IDA implements solar radiation modelling, including assumptions, was available and the formulas involved could not be deduced from the Fortran source code of the IDA model. Therefore the methodology used to incorporate solar radiation in the circuit model was chosen, based on the simple building simulation tool of Nielsen[18] with some modifications and omissions. The assumptions made and techniques used to incorporate solar radiation into the equivalent circuit model of the low energy house probably differ from the IDA modelling of solar radiation, contributing significantly to the simulation output discrepancies shown in Figures 4.11 and 4.12.

4.3.7 Heating/Cooling

Heating and cooling are simulated in a circuit model using a current source connected to the circuit node requiring temperature manipulation. The value of the current source can be based on modelled temperatures throughout the circuit using an algebraic expression of circuit node voltages. This enables the implementation of a thermostat-based switched heater/chiller dependent on the temperatures at different points (nodes) of the house (circuit).

The application of heating/cooling modelling described here and in Ch. 5 is determining the thermal energy required for maintaining the indoor temperature at a setpoint temperature over a period of time. One application not analysed in this thesis is an embedded slab (floor) heater simulated by applying a heater current source to a node within the concrete floor macro (Fig. 4.2) at the required depth. The depth is approximated by selecting the

appropriate node in the RC ladder of the concrete floor layer (Fig. 4.3). Another potential use of heating modelling not analysed is testing the efficacy of a particular rated heater in meeting a setpoint temperature requirement. Scheduled activation can be achieved by referencing the global time variable t in the conditional portion of the current source specification (Eqn. 17) in a similar manner to the implementation of night time ventilation resistance (Eqn. 10) of 4.3.5.

An overview of the modelling configuration for determining the thermal energy required to maintain a setpoint temperature indoors is described, with specific energy calculations illustrated in Chapter 5. A standard space heater is modelled as a current source with a value based on the difference between the *setpoint* and inside wall *surface* temperatures. As shown in Fig. 4.6 below, the current source is applied directly to the indoor air node and is switched on and off based on this difference.
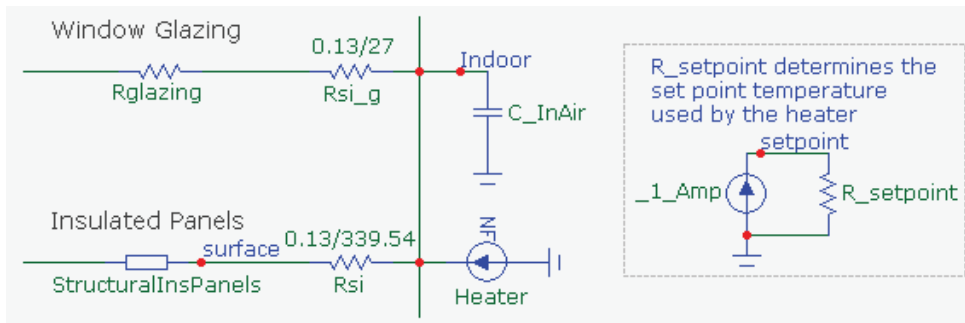
Figure 4.6: Circuit Fragment Showing Heater Component; User Specifiable Setpoint Temperature via *R_setpoint*

Energy usage rather than heater power rating is sought and therefore an expression for the current source was found using *trial-and-error* that minimized the current (heater) activation when $T_{indoor} > T_{setpoint}$ while ensuring the indoor temperature did not drop below the setpoint. Simple On-Off switching logic cannot be used as the current source expression since Micro-Cap will fail to converge during simulation. A less sudden transition is required. For 0 ach infiltration and no solar input, the following current source expression (Eqn. 17) was found to converge producing the required behaviour as illustrated in Figure 4.7:

$$\dot{Q}_{heater} = \begin{cases} 900(T_{setpoint} - T_{indoor} + 1.2\,)^4 - 1400(T_{setpoint} - T_{indoor} + 1.1\,) & if \ T_{surface} < (T_{setpoint} + 0.2\,) \\ 0 & if \ T_{surface} \geq (T_{setpoint} + 0.2\,) \end{cases} \quad (17)$$

This is an example of a simple PID (Proportional, Integral, Derivative) controller [87] with the current value as a function of the difference between $T_{setpoint}$ and T_{indoor}, when T_{indoor} drops below $T_{setpoint}$. From this perspective, the heater current source performs a correcting function.

The heater current source component expression (Eqn. 17) is entered into Micro-Cap as:

(V(surface)<(V(setpoint) + 0.2))*(900*(V(setpoint)- V(Indoor) + 1.2)^4 - 1400*(V(setpoint) - V(Indoor) + 1.1))

Figure 4.7 below illustrates the effect that the heater current source has on the indoor temperature response of the low energy house for March modelled in Micro-Cap. The heater has no effect (shut off) when the indoor temperature is above $T_{setpoint} = 20°C$.
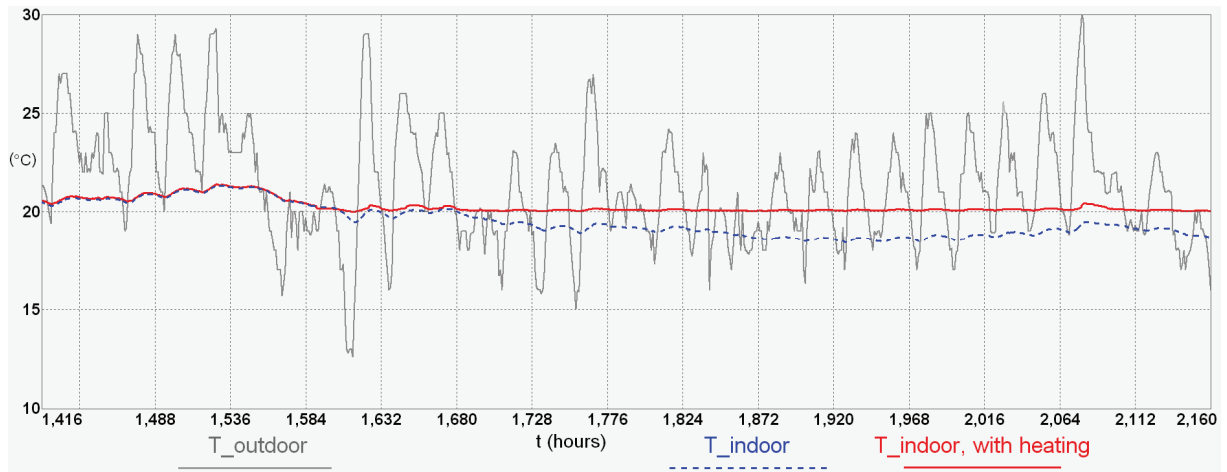
Figure 4.7: March Indoor Temperature Response, 0 ach, No Solar, With/Without Heating, $T_{setpoint} = 20°C$

Once the required indoor temperature response is modelled (Fig. 4.7), the total thermal energy required over a time period is determined by integrating the current value over the period using Micro-Cap. In this case, the March heating load is computed by integrating the heater component output over March. Calculation examples of thermal energy requirements over 1 month for a set point temperature are given in Chapter 5.

Reversing the current source component enables the same strategy to be used to determine cooling loads as shown in Figure 4.8 below.
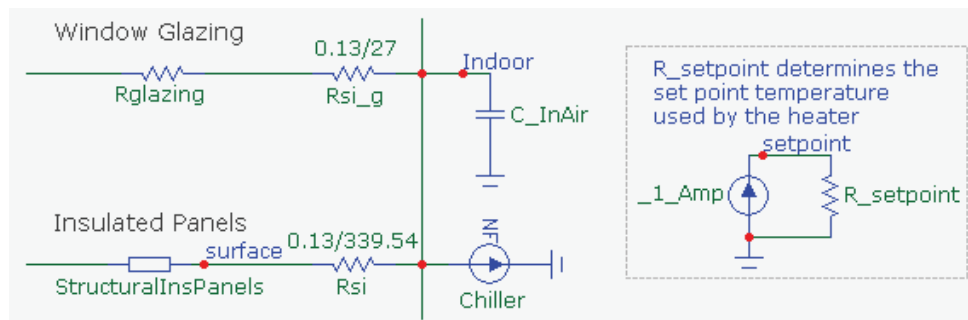
Figure 4.8: Circuit Fragment Showing Chiller Component; User Specifiable Setpoint Temperature via $R_{\_setpoint}$

Note that no artificial heating or cooling was active during all simulations discussed in the following section. Results of circuit simulation involving artificial heating and cooling are presented in Chapters 5 and 6.

4.4 Comparing IDA and Micro-Cap Simulation Output

The results of comparing the indoor temperature sequences generated by the IDA model and the Micro-Cap circuit model (Fig. 4.1) are presented in this section. The purpose of this comparison is to provide evidence that thermal modelling of a building using electric circuits and Micro-Cap is as effective as modelling using a commercial building simulation package. As mentioned previously, this is a high level, non-transparent comparison due the fact that the details underpinning the IDA implementation of items such as thermal mass, infiltration and solar insolation were not taken into account during construction of the corresponding circuit model since they were not fully known.

The monthly average indoor temperatures of year-length simulations of the low energy house in Sydney modelled using IDA and using the equivalent Micro-Cap circuit (Fig. 4.1) are shown in Table 4.5 below. These simulations had no infiltration and no solar input. As is the case for all simulation results presented in this section, no artificial heating or cooling is active.

The average monthly indoor temperatures are shown as well as the Mean Bias Error (MBE) and the Coefficient of Variation of the Root-Mean-Squared Error (Cv(RMSE)) of the Micro-Cap model approximation to the IDA hourly indoor temperature sequences for each month. The US Dept of Energy suggests that both statistical measures be considered when comparing 2 data sequences [88].

| Month	Avg IDA	Avg Micro-Cap	MBE	Cv(RMSE)
Jan	20.552	20.593	0.202%	0.638%
Feb	21.190	21.180	-0.048%	0.517%
Mar	20.119	20.133	0.067%	0.485%
Apr	17.979	18.003	0.134%	0.660%
May	15.654	15.673	0.122%	0.577%
June	13.606	13.635	0.215%	0.681%
July	**12.302**	**12.287**	**-0.129%**	**1.006%**
Aug	12.901	12.902	0.008%	1.153%
Sep	14.154	14.159	0.033%	0.850%
Oct	17.239	17.256	0.095%	1.103%
Nov	18.178	18.163	-0.083%	0.665%
Dec	19.447	19.429	-0.090%	0.713%
Yearly	16.919	16.927	0.046%	0.748%

Table 4.5: Monthly Average Indoor Temperatures from IDA and Circuit Models Compared

A graph of the hourly indoor temperature response for the two models is shown in Figure 4.9 for Sydney in July, a month with one of the higher Cv(RMSE) values and a mid MBE value. MBE values of ±10% and Cv(RMSE) values of 30% are considered acceptable values when calibrating a building simulation model to actual empirical temperature/energy data from the corresponding building [88]. Although the comparison here is between the output sequences of two simulation programs, the MBE and Cv(RMSE) values suggest excellent correlation.

50
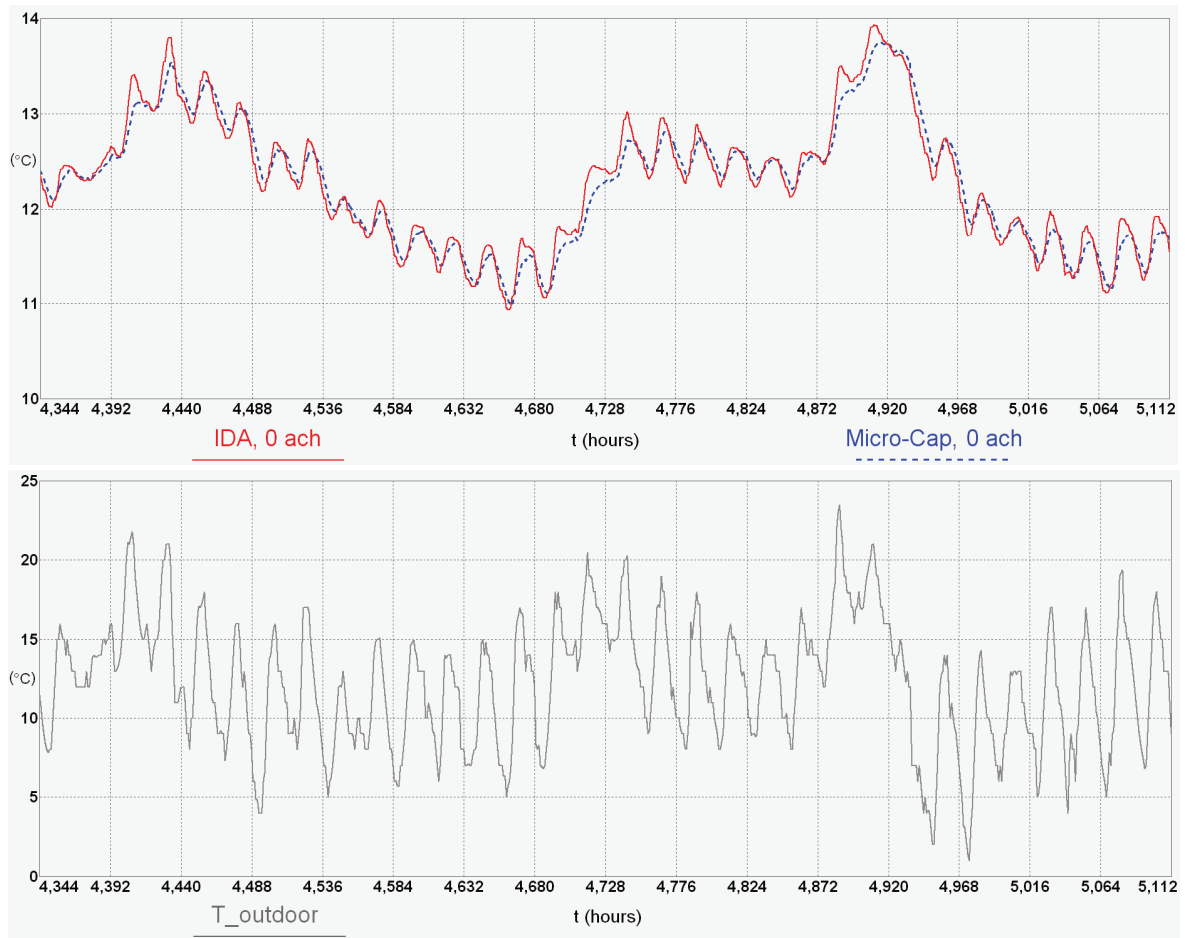
Figure 4.9: July Indoor, Outdoor Temperature Sequences for Circuit and IDA Models, 0 ach, no Solar

Introducing infiltration to this comparison proved to be less successful. With the infiltration rate of the IDA model set at 1 ach, the indoor temperature sequences generated by the IDA model and equivalent circuit model were compared for varying circuit model infiltration rates near 1 ach (0.5 – 2 ach). At many hourly points of the indoor temperature sequences, there is significant discrepancy ($>$1°C) as shown in Fig. 4.10 below for the circuit model with 1.2 ach ventilation.
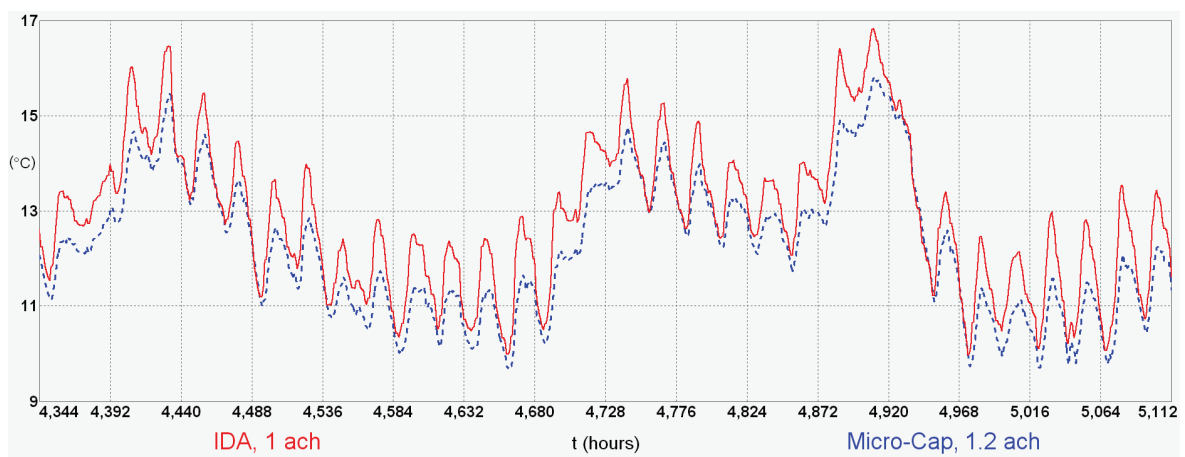
Figure 4.10: July Indoor Temperature Sequences for Micro-Cap 1.2 ach and IDA 1 ach Models, no Solar

51

The indoor temperature response of the circuit model with 1.2 ach infiltration is shown here since it had a lower Cv(RMSE) value than the sequence for 1.0 ach and it was found to be the best fit for the solar and infiltration case shown next. For IDA simulations with 1 ach infiltration only (no solar input), circuit model sequences for infiltration rates greater than 1 ach and less than or equal to 2 ach were better fits to IDA-generated sequences compared to the circuit model with 1 ach infiltration.

A significant amount of time was spent, without success, searching the IDA Fortran source code for the modelling details and assumptions related to the implementation of infiltration and solar input in the IDA models. For example, details such as the heat transfer formulas used and the base infiltration level, assumed by IDA in addition to infiltration rates specified by an IDA user, could not be determined. As no IDA program documentation was on hand, the implementation of infiltration as described in section 3.2 was employed in the circuit models of this thesis.

IDA and Circuit Models with Solar Insolation and Infiltration Included
As was the case with infiltration, no documentation pertaining to how IDA implements solar insolation modelling (including modelling assumptions) was available. Therefore a modelling strategy was needed to be chosen and this was presented in section 4.3.6.

For each month, averages of hourly indoor temperatures and statistical measures of how well the hourly Micro-Cap indoor temperature sequence approximates the corresponding IDA sequence are shown in Table 4.6 below.

Month	Avg IDA	Avg Micro-Cap	MBE	Cv(RMSE)
Jan	27.005	26.509	-1.838%	3.359%
Feb	27.348	27.056	-1.069%	2.668%
Mar	26.103	26.275	0.657%	2.388%
Apr	23.349	23.537	0.804%	3.746%
May	20.599	20.359	-1.162%	5.030%
June	17.571	17.536	-0.199%	4.853%
July	16.834	16.880	0.275%	5.891%
Aug	18.537	18.900	1.957%	5.461%
Sep	19.938	20.263	1.627%	4.561%
Oct	23.295	23.472	0.763%	3.262%
Nov	24.498	23.951	-2.232%	4.468%
Dec	25.739	25.093	-2.507%	4.123%
Yearly	22.542	22.461	-0.359%	4.064%

Table 4.6: Monthly Avg Indoor Temperature Comparison, IDA and Circuit Models; Solar, Infiltration Included

The infiltration rate of 1.2 ach was chosen as it resulted in the best (minimum) yearly Cv(RMSE) value (4.064%). It is plausible that 0.2 ach is the base infiltration rate used by IDA which when added to the 1.0 ach infiltration rate gives a total of 1.2 ach. Without knowing the technical details of the IDA implementation of infiltration and solar radiation input, it is

fruitless to speculate on the source of the discrepancies between the two models owing to the complexity of the computations involved.

Nonetheless, the indoor temperature sequence produced by the circuit model does *follow* the corresponding IDA sequence reasonably well (given the computations involved) as shown in Figures 4.11 and 4.12. The degree of correlation is significantly less than the Micro-Cap-IDA comparison involving no infiltration and no solar insolation (Table 4.5, Fig. 4.9).
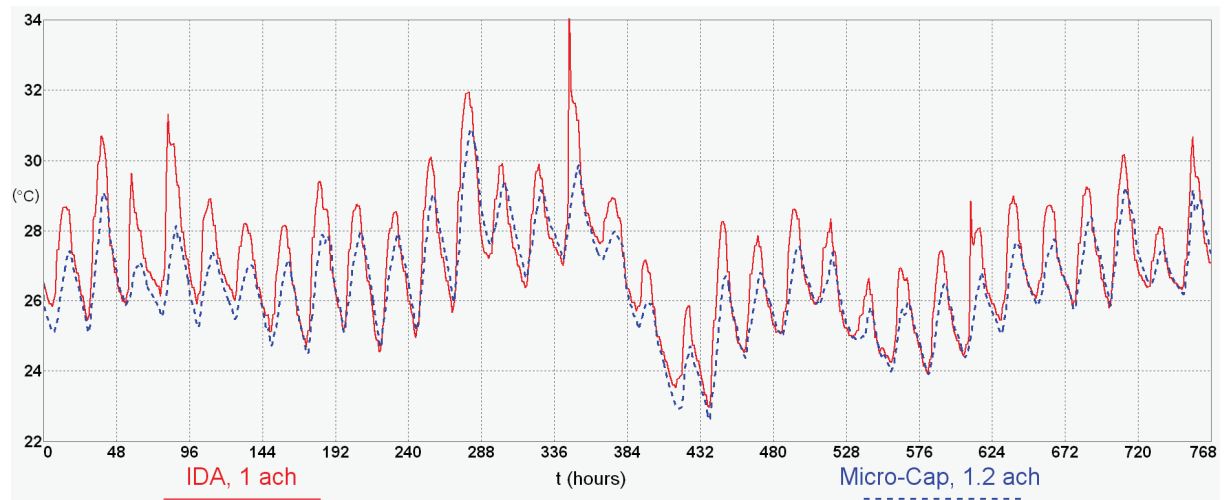
Figure 4.11: January Indoor Temperature Sequences, Micro-Cap (1.2 ach), IDA (1 ach) Models; Solar Included
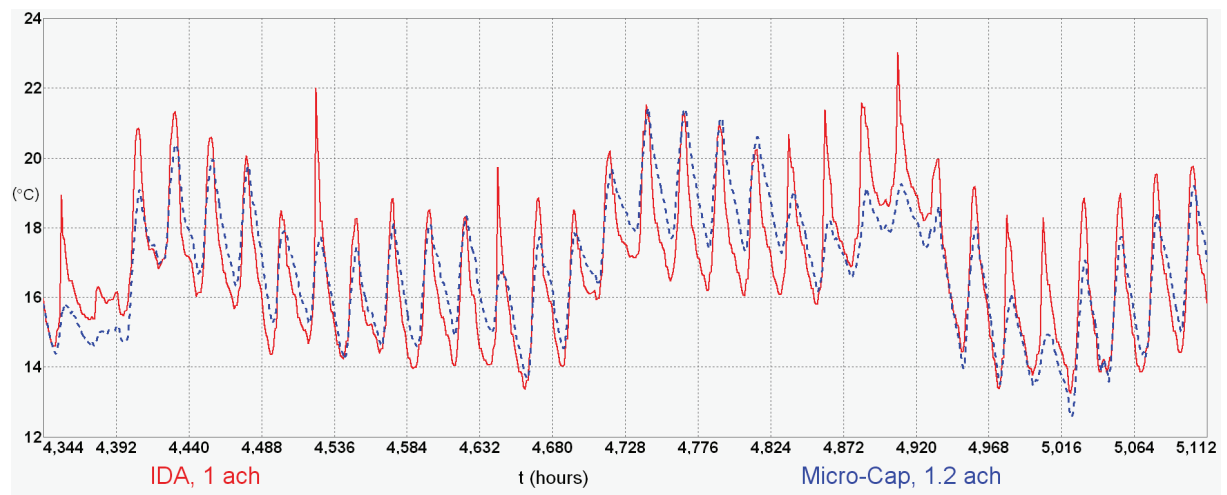
Figure 4.12: July Indoor Temperature Sequences, Micro-Cap (1.2 ach), IDA (1 ach) Models; Solar Included

53

4.5 Chapter Summary

The low energy house was originally modelled using IDA and the circuit model was designed to mimic the IDA implementation (i.e. use the same modelling assumptions) in order to verify the Micro-Cap circuit simulation output. For simulations involving no infiltration and no solar input, the comparison results summarized in Table 4.5 and illustrated in Fig. 4.9 show excellent agreement with the maximum monthly *|MBE| = 0.22%* and maximum monthly *Cv(RMSE) = 1.15%*.

For simulations involving infiltration and solar input, the results summarized in Table 4.6 and displayed in Figs. 4.11 and 4.12 do not suggest the same agreement. This either (i) casts some doubt on the accuracy of either model or (ii) indicates that elements of the IDA model were not accounted for in the equivalent circuit model due to the lack of transparency of the IDA model. Referring again to the 2 sequences of Figs. 4.11 and 4.12 it can be seen that at various time spans, the IDA sequence contains significantly larger (and sharper) amplitude temperature swings of approximately the same (daily) frequency compared to the circuit model sequence. For a house with significant thermal mass, this response is unexpected and casts some doubt on the accuracy of the IDA model. From Table 4.6, the maximum monthly statistical comparison values are: *|MBE| = 2.51%* and *Cv(RMSE) = 5.89%*. Both of these pairs of values are well within the MBE threshold of 10% and Cv(RMSE) threshold of 30%, considered acceptable values for building simulation model calibration [88]. This calibration is between a simulation model and empirical data, whereas the comparison here is between the outputs of two simulation models. One would think the threshold values should be lower for this type of comparison.

Taking into account the lack of available technical information about the implementation of solar radiation and infiltration of the IDA model and the complexity of the computations involved, the agreement between the IDA and circuit models is reasonably good. The difficulty in determining the physical assumptions employed in the IDA modelling of infiltration and solar radiation is symptomatic of the non-transparent nature of large building simulation programs that often hide physical properties/relationships from the user. In Chapter 6 a simple transparent model is presented and used to suppliment the verification of the circuit modelling methodology presented here with more varied simulation output considered (e.g. heating loads).

5 Building Analysis and Parametric Study

In this chapter, further simulation results generated by circuit models of the low energy house are presented in order to illustrate the *analysis potential* of modelling using thermal circuits and Micro-Cap. Although not an exhaustive thermal analysis of the low energy house, the intention of this chapter is to show that the methodology in this thesis can produced detailed and useful results.

The starting point is the circuit model presented in the previous chapter (Fig. 4.1). With the necessity to mimic the IDA model of the low energy house removed, components of this (IDA-equivalent) circuit model that were based on questionable assumptions of the original IDA model, are modified. These components are the sky and ground temperature models as defined by the IDA model. Incorporating new sky and ground temperature models into the IDA-equivalent circuit model forms the "Reference" circuit model used to generate circuit simulation results presented in this chapter. The simulation results presented in this chapter are more detailed than those presented in Chapter 4 and include:

(i)   monthly average indoor temperatures

(ii) monthly heating and cooling loads

(iii) frequency response of the house

The above computations are made using the Reference circuit and variations in order to observe how changing a modelling parameter impacts simulation results. For example, the impact of changing the sky temperature of the IDA model (Eqn. 4.3) to the Bliss clear sky model [70]. Other parameters varied are: infiltration rate, thermal mass/envelope resistance and solar input. The impact of using a simpler ground temperature model for the Reference circuit is not investigated.

5.1 Modifying the IDA Circuit Model

The IDA circuit model (Fig. 4.1) is based on replicating the model of the low energy house and climate as implemented in the IDA ICE building energy simulation program [64]. In this section, a *Reference* circuit model (Fig. 5.3) is assembled, by changing the modelling of the sky and ground temperature of the IDA model. Note that once a new modelling strategy for a component is determined, integration into the circuit model is straightforward.

5.1.1 Sky Temperature
As discussed in section 2.3.3, the Bliss [70] clear sky temperature model was chosen as a conservative and more realistic alternative to the basic IDA sky temperature representation (Eqn. 2.8). It is a cooler temperature sequence than the IDA sequence, but it is the warmest of the group of clear sky temperature models discussed by Pandey [69], some of which are shown in Figs. 2.1 and 2.2. Although this model assumes clear sky conditions throughout the

year, choosing the warmest of this group of clear sky models minimizes the inaccuracy of this assumption.

Since the original sky temperature of the IDA model is: $T_{sky} = T_{outdoor} - 5$ and the Bliss sky temperature model approximately coincides with: $T_{sky} = T_{outdoor} - 12$, this change in sky model represents an overall drop in sky temperature of approximately 7°. The impact of this change on the monthly average temperatures and heating/cooling loads is investigated in the sections that follow. The low energy house has large, horizontal and unobstructed roof area, suggesting the impact could be significant.

The Bliss sky temperature model is based on the outdoor and dew point temperatures (Eqn. 2.10-Bliss). The hourly temperature sequence is calculated in a spreadsheet, copied to a Micro-Cap user data file and referenced by the T_{sky_Bliss} voltage component of the Reference circuit model of Fig. 5.3 below.

5.1.2 Ground Temperature

The IDA model of the ground consists of a ground temperature source that is roughly a damped version of outdoor temperature, behind very large thermal mass and insulation layers (Ground Insulation and Soil) and is shown in Figure 5.1 below.
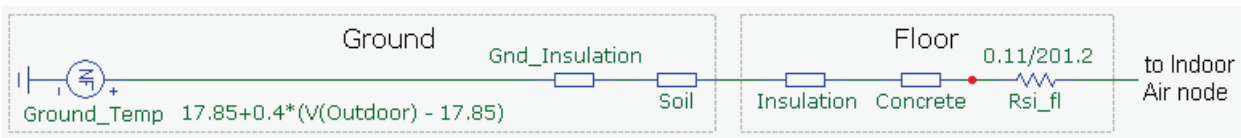
Figure 5.1: Extract of IDA Circuit Model; Implementation of Ground and Floor

This was the *intended* modelling of the ground. The *actual* modelling of the ground in the IDA model incorrectly implemented the ground insulation *(Gnd_Insulation)* as a thermal resistance only (see Fig. 4.1). The IDA ground model does not treat the ground as a temperature source acting directly on the insulation below the floor. Moreover, immediate hourly deviations in outdoor temperature immediately impact the ground temperature (damped by a factor of 0.4).

Instead of modelling the ground temperature as a temperature source behind insulation and thermally massive soil layers shown in Fig. 5.1 above, a simpler ground temperature representation is used: a single ground temperature source models the ground surface temperature directly beneath the insulated floor. Using the three components of the yearly outdoor temperature sequence (T_{mean_air}, $T_{amp\_air\_monthly\_avg}$, $Phase_{air}$) as estimates to the unknown corresponding ground surface temperature components as discussed by Kusuda [59], an equation for the ground surface temperature is derived. A least-squares fitting of the monthly average outdoor temperatures derived from the Sydney IWEC hourly climate data to Eqn. 2.7 was implemented using a spreadsheet, resulting in the following equation:

56

$$T_{gnd\_surface}(t) = 17.86 - 4.94 \sin [2\pi/8760(t - 3.49 + 1.57)]$$
$$= 17.86 - 4.94 \sin [2\pi/8760(t - 1.92)] \qquad \text{the phase in degrees is: -109.1°} \qquad (1)$$

Eqn. 1 was also obtained as the fundamental frequency of a Fourier decomposition of the Sydney IWEC hourly outdoor temperature data for one year, implemented in a spreadsheet.

The ground temperature equation (Eqn. 1) *directly* defines the Micro-Cap voltage source *Tgnd_Kusuda* modelling ground surface temperature in Figure 5.3 below: there is no hourly data file driving this voltage source as implemented for the *Outdoor_Temp* voltage source.

The yearly temperature sequences of this version of the Kusuda ground model (Eqn. 1) and the soil-insulation boundary of the original IDA model as generated by Micro-Cap are shown in Fig. 5.2 below.
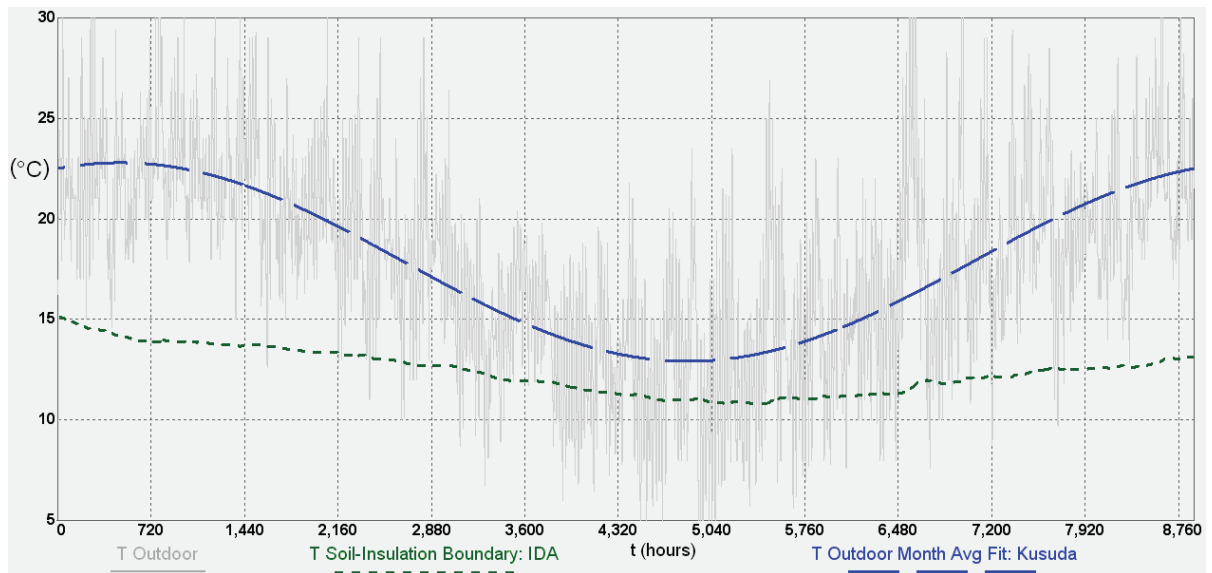
Figure 5.2: Yearly Temperature Sequences of Outdoor, Kusuda Ground Surface, IDA Soil-Insulation Boundary

5.1.3 The Reference Circuit Model

The Reference circuit model incorporating the sky and ground temperature modelling changes to the IDA circuit model is shown in Figure 5.3 below. It is used as a base model for analysing the thermal performance of the low energy house with parametric variations. For simulations with no solar input, the three circuit elements of Fig. 5.3 modelling solar input are disabled before running the simulation *(SolarAbsorb_Frames, SolarAbsorb_SIP, SolarGain2Floor).*
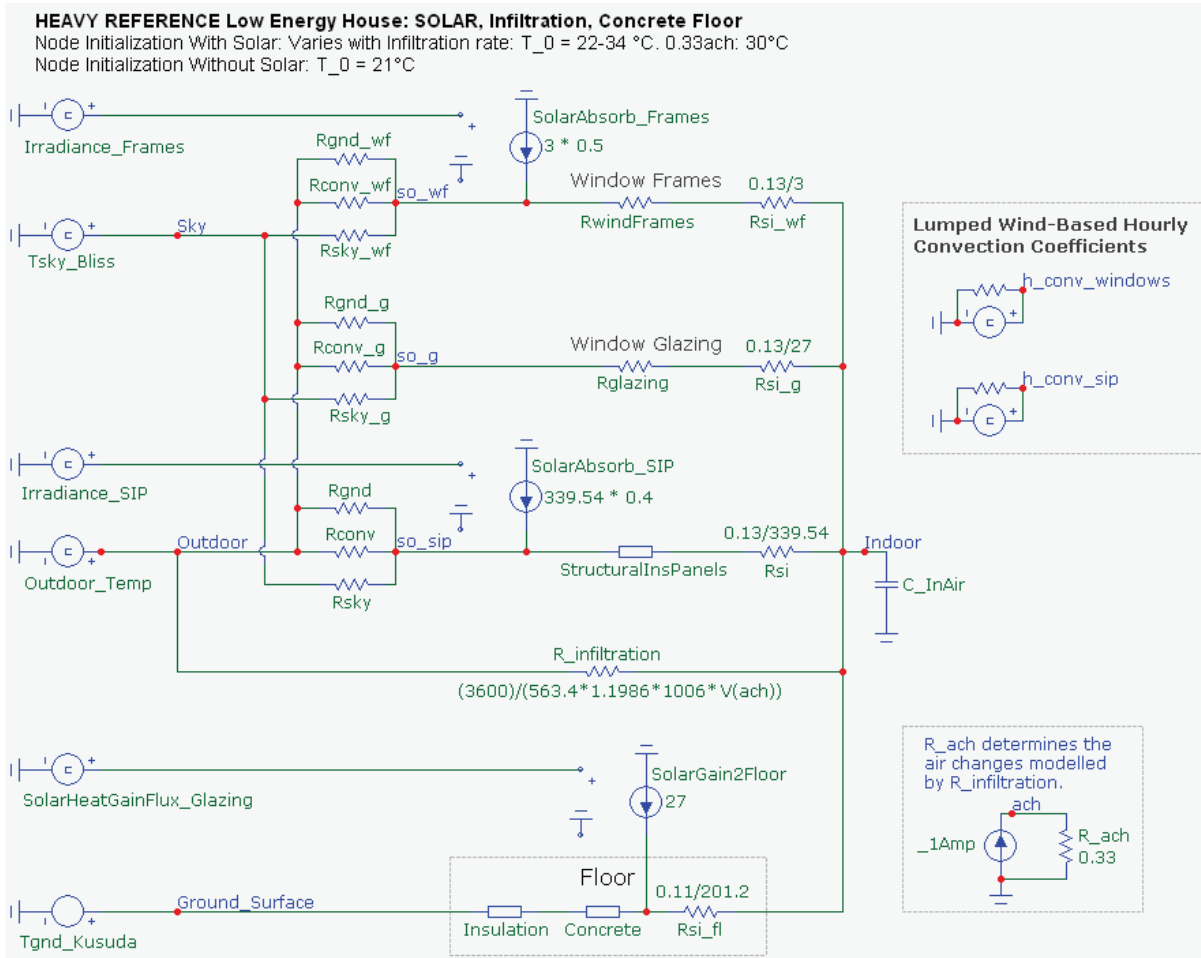
Figure 5.3: Reference Circuit Model of the Low Energy House

5.2 Parametric Variations of the Reference Circuit

In this chapter, physical and climatic parameters of the Reference circuit are modified and circuit simulation results are presented in order to observe the general significance of a parameter. These are typical "what-if" type scenarios implemented in a circuit model as a component change and can form the basis of a sensitivity analysis commonly used to determine optimal parametric values of a building [89]. The physical and climatic parameters investigated in this chapter are listed below.

(i) *Solar Insolation*. The thermal performance of the low energy house is investigated with and without solar insolation. Models having no solar input are unrealistic to the extent that a fully shaded house has *some* solar input due to diffuse and reflected solar radiation.

58

However, models with no solar input are useful to investigate how the house reacts to outside temperature variations only. For this climatic variation, the simulation results of the same circuit with and without solar components enabled are compared.

(ii) *Infiltration*. The base (reference) infiltration rate is 0.33 ach. The infiltration rate of a circuit is varied by modifying the *ach* value of the $R_{\_infiltration}$ component in a circuit model. (e.g. Fig. 5.3).

(iii) *Sky Temperature*. As discussed previously, the Reference circuit model is based on the original IDA circuit model and includes a change in the sky temperature model from $T_{sky}(t) = T_{outdoor}(t) - 5$ to the clear sky temperature model of Bliss[70]. The Bliss model is approximately 12°C below the outdoor temperature: $T_{sky}(t) \approx T_{outdoor}(t) - 12$ and is dependent on $T_{outdoor}(t)$ and $T_{dewpoint}(t)$. The impact of this overall approximate drop of 7° is investigated by comparing results of simulations repeated with the Reference sky temperature component *Tsky_Bliss* replaced with the original IDA sky temperature component (*Sky_Temp*, Fig. 4.1).

(iv) *Thermal Mass*. The low energy house contains significant thermal mass in the floor and to a lesser extent in the walls and ceiling. To investigate the significance of thermal mass, two variations of the Heavy Reference house are modelled: a Medium version a the Light version. These variations differ from the Reference version in floor, wall and ceiling construction as shown in Table 5.2, resulting in buildings with less thermal mass and less envelope resistance. All other physical characteristics are identical. For example, all three buildings have 260mm insulation (R-Value 6.5) below the floor.

The metric *Specific Mass (sM)* [90] is used to categorize buildings as Heavy, Medium or Light:

$$sM = total\ mass \div total\ floor\ area\ (kg/m^2) \qquad (2)$$

The definition of these categories, the Specific Mass values and construction variations of the Light, Medium and Heavy houses are shown in Tables 5.1 and 5.2 below. The Building Time constant *(τ;* described in section 2.2) computed using a circuit model is also shown below for these houses with a base infiltration rate of 0.33 ach.

Category	sM (kg/m²)		Circuit	Walls, Ceiling	Floor with R-value 6.5 Insulation Below	sM (kg/m²)	τ (hr)
Light	< 150		Light	Uninsulated 20mm Timber	20 mm Timber	41	1.6
Medium	150 – 400		Medium	SIP: 40 mm Insul, R-Value: 1.0	42 mm Concrete	153	14.6
Heavy	> 400		Heavy	SIP: 250mm Insul, R-Value: 6.25	150 mm Concrete	412	99.3

Tables 5.1, 5.2: Categorization of the Weight of a Building [90] and Reference Circuit Construction Variations

Note that the categorization using Specific Mass does not depend on the net thermal resistance (R_T) between indoors and outdoors whereas the building time constant is based on this and the thermal capacitance of the building.

The circuit model for the Light version of the low energy house is shown in Appendix G. Herein, when discussing thermal mass, the *Reference* building/circuit/model is also referred to as the *Heavy* building/circuit/model.

5.3 Monthly Average Indoor Temperature

5.3.1 Reference Circuit Averages

Monthly average indoor temperatures as computed by the (Heavy) Reference circuit with and without solar input are shown below in Table 5.3.

Month	$T_{outdoor}$	No Solar Input						With Solar Input					
ACH →	---	0	*0.33*	1	3	5	10	0	*0.33*	1	3	5	10
Jan	22.03	20.29	*20.77*	21.22	21.64	21.77	21.89	33.89	*29.99*	26.74	24.20	23.43	22.77
Feb	22.86	20.81	*21.48*	22.03	22.46	22.59	22.71	34.04	*30.39*	27.38	24.91	24.18	23.56
Mar	21.30	19.53	*20.12*	20.62	21.03	21.14	21.22	34.05	*29.98*	26.57	23.74	22.89	22.15
Apr	18.66	17.01	*17.52*	17.94	18.31	18.43	18.54	31.13	*27.03*	23.67	20.95	20.15	19.45
May	15.93	14.24	*14.77*	15.22	15.59	15.70	15.81	27.11	*23.33*	20.29	17.87	17.17	16.58
June	13.37	11.84	*12.40*	12.83	13.14	13.22	13.29	22.57	*19.68*	17.25	15.18	14.55	14.00
July	12.29	10.27	*10.93*	11.46	11.89	12.02	12.14	22.89	*19.45*	16.59	14.24	13.55	12.96
Aug	13.57	10.87	*11.72*	12.44	13.04	13.23	13.39	26.02	*22.02*	18.69	15.92	15.10	14.38
Sep	15.27	12.41	*13.25*	13.98	14.64	14.86	15.05	27.37	*23.42*	20.15	17.47	16.68	16.02
Oct	18.37	15.71	*16.69*	17.46	18.02	18.16	18.26	30.65	*26.69*	23.43	20.72	19.91	19.19
Nov	19.75	17.17	*17.96*	18.63	19.21	19.39	19.56	30.76	*27.07*	24.07	21.68	20.99	20.40
Dec	21.19	19.00	*19.74*	20.34	20.81	20.95	21.06	31.45	*28.10*	25.37	23.13	22.45	21.86
Yearly	17.85	15.73	*16.42*	16.98	17.45	17.59	17.72	29.30	*25.57*	22.49	19.97	19.23	18.58

Table 5.3: Monthly Average Indoor Temperatures (˚C); Reference (Heavy) Circuit With and Without Solar

With no solar input and 0.33 ach infiltration, the Heavy house maintains an average indoor air temperature (herein *indoor temperature*) within the 1.5° span below than the average outdoor temperature. This agreement increases as the infiltration rate increases. *With no solar input*, as the infiltration rate increases, the indoor averages *increase* towards the outdoor averages: the building is less able to hold the heat deficit acquired from the cool sky. *With* solar input, as the infiltration rate increases, the indoor averages *decrease* towards the outdoor averages: the building is less able to hold the solar gain.

The significance of solar energy can be seen from the increase in the monthly averages for the base infiltration rate of 0.33 ach. This 7-11° increase diminishes as the rate of infiltration increases, because an increasing proportion of solar gain is lost through the higher level of heat transfer from the indoors to outdoors. With 0.33 ach infiltration, the addition of solar energy makes the winter indoor temperature very comfortable while causing the house to overheat during the summer. This suggests a need to limit solar input during the summer using shading or blinds.

The following two sections summarize the changes *(Δ)* to circuit computations of monthly average indoor temperatures of the Reference house due to varying (i) the sky temperature and (ii) construction materials (including thermal mass) at various infiltration rates.

5.3.2 The Effect of a Warmer Sky Temperature

The Reference circuit model includes an hourly clear sky temperature sequence derived from the hourly sequences of outdoor and dew point temperatures sequences as defined by Bliss [70]. In terms of the outdoor temperature *only*, it is approximately: $T_{sky}(t) = T_{outdoor}(t) - \Delta T$, with ΔT varying between 10 and 14° and *average(ΔT)* ≈ *12°* whereas the sky temperature expression defined in the original IDA model is: $T_{sky}(t) = T_{outdoor}(t) - 5$.

Switching the sky temperature derivation back to the original warmer derivation of the IDA model results in an increase in the monthly average indoor temperatures listed below in Table 5.4.

Month	$\Delta = T_{in\ avg\ IDA\ Sky} - T_{in\ avg\ Reference}$					
ACH →	0	*0.33*	1	3	5	10
Jan	0.86	*0.62*	0.39	0.19	0.12	0.07
Feb	0.95	*0.64*	0.39	0.18	0.11	0.06
Mar	0.98	*0.66*	0.40	0.18	0.12	0.06
Apr	1.08	*0.73*	0.45	0.21	0.13	0.07
May	1.19	*0.81*	0.49	0.22	0.14	0.08
June	1.30	*0.89*	0.54	0.25	0.16	0.09
July	1.42	*0.96*	0.58	0.27	0.17	0.09
Aug	1.43	*0.96*	0.58	0.26	0.17	0.09
Sep	1.33	*0.90*	0.54	0.25	0.16	0.08
Oct	1.30	*0.88*	0.53	0.24	0.16	0.08
Nov	1.22	*0.82*	0.49	0.22	0.14	0.08
Dec	1.01	*0.67*	0.40	0.18	0.12	0.06
Year	**1.17**	***0.80***	**0.48**	**0.22**	**0.14**	**0.08**

Table 5.4: Differences in Average Temperatures; Reference Circuit and Sky Temperature Variant; With Solar

The effect of the sky temperature change on the average indoor temperature diminishes as the infiltration rate increases. The effect is largest during the winter for all infiltration rates.

For the base infiltration rate of 0.33 ach, lowering the modelled sky temperature by approximately 7° (IDA → Reference) results in roughly a 1° drop in average indoor temperature during the winter months. Had the IDA model used a sky temperature equal to the outdoor temperature, the drop would have been roughly 1.6° during the winter months. This highlights the importance of an accurate sky temperature model when estimating heating loads. For simulations with *no solar input*, a table of average differences with magnitudes similar to the values of Table 5.4 is produced for this sky temperature comparison.

5.3.3 The Effect of Thermal Mass

Table 5.5 below lists the signed difference in circuit-computed monthly average indoor temperatures between the Heavy and Medium houses and between the Heavy and Light houses at various infiltration rates, *with* solar input. Section 5.2 includes a description of the construction materials making up the Medium and Light versions of the (Heavy) Reference house.

Month	Solar: $\Delta = T_{in\_avg\_Heavy} - T_{in\_avg\_Medium}$						Solar: $\Delta = T_{in\_avg\_Heavy} - T_{in\_avg\_Light}$					
ACH →	0	0.33	1	3	5	10	0	0.33	1	3	5	10
Jan	5.78	2.77	0.72	-0.19	-0.27	-0.23	7.92	4.24	1.39	-0.36	-0.64	-0.63
Feb	5.87	3.00	1.03	-0.02	-0.16	-0.16	7.90	4.43	1.75	-0.06	-0.39	-0.45
Mar	7.09	3.86	1.58	0.27	0.05	-0.04	9.75	5.85	2.75	0.53	0.05	-0.19
Apr	7.66	4.27	1.86	0.41	0.15	0.02	10.33	6.36	3.22	0.92	0.38	0.05
May	7.82	4.55	2.18	0.66	0.33	0.13	10.27	6.54	3.60	1.36	0.78	0.34
June	6.61	4.09	2.18	0.80	0.46	0.22	9.01	6.12	3.72	1.68	1.08	0.56
July	7.34	4.38	2.16	0.68	0.36	0.15	9.94	6.54	3.75	1.53	0.92	0.44
Aug	7.68	4.38	1.98	0.49	0.21	0.05	10.63	6.73	3.58	1.18	0.59	0.18
Sep	6.96	3.78	1.52	0.21	0.00	-0.07	9.59	5.79	2.77	0.59	0.12	-0.13
Oct	6.79	3.64	1.45	0.22	0.02	-0.05	9.30	5.51	2.54	0.44	-0.01	-0.22
Nov	5.77	2.86	0.90	-0.09	-0.20	-0.18	7.77	4.27	1.59	-0.15	-0.44	-0.48
Dec	4.86	2.30	0.63	-0.17	-0.24	-0.19	6.76	3.60	1.22	-0.32	-0.56	-0.55
Yearly	6.69	3.66	1.52	0.27	0.06	-0.03	9.11	5.51	2.66	0.62	0.16	-0.09

Table 5.5: Differences in Average Indoor Temperatures; Heavy – Medium, Heavy – Light; With Solar

At the base infiltration rate of 0.33 ach, the change to a Medium and Lightweight construction results in average temperature drops of 3.7° and 5.5° respectively. These average temperature drops are advantageous in the summer but disadvantageous in the winter. When solar input is disabled, these average temperature drops are significantly lower: 1.1° and 1.6° respectively (not shown). The magnitude of these drops decrease as the infiltration rate increases. For a 10 ach infiltration rate the averages for the Heavy and Medium houses are within 0.25° of each other while the averages for the Heavy and Light houses are within 0.65° of each other. At this infiltration rate during the summer months, the averages for the Heavy house are lower than both the Medium and Light houses suggesting the Heavy house is utilizing the cooling due to infiltration and sky temperature more effectively.

Table 5.5 gives no indication of the effect thermal mass has on the daily swings in indoor temperature. Figures 5.4b and 5.5b show the February and June indoor temperature responses for the Heavy, Medium and Light houses with 0.33 ach infiltration and solar input. Because of the significant thermal mass in the Heavy house, the daily indoor temperature swings are significantly less than the swings of the Light house and less than the swings of the Medium house. The variations of daily indoor temperature swings amongst these three houses echo the frequency responses of the three models shown in Fig. 5.9. Note that the bode plots of Fig. 5.9 are based on the frequency response of the houses to outdoor temperature variation only (no solar input, $T_{gnd} = T_{sky} = T_{outdoor}$), whereas the graphs of

Figures 5.4 and 5.5 are the output of simulations *with* active solar input and with versions of T_{sky} and T_{gnd} that depend less directly on $T_{outdoor}$.

For the Heavy house with solar input, the indoor temperature response is a smoothed and damped version of the outdoor temperature variations. If solar input is disabled then this damping effect is significantly increased and the average temperature drops by 7-11°: 7.3° for June (Fig 5.5b). For the Light house in both winter and summer, the amplitude of the indoor temperature swings exceeds the corresponding swings in outdoor temperature. This larger amplitude is due to daily high temperatures occurring when solar irradiance on the large flat roof is at a maximum producing high indoor temperatures. In other words, the light building is very exposed to the outdoor temperature and solar insolation. As infiltration increases the amplitude decreases: the indoor temperature approaches the outdoor temperature. The same effect occurs for the Medium and Heavy models except at low infiltration when the amplitude of the temperature swings are lower, *increasing* with infiltration rate: the indoor temperature sequences approach the outdoor temperature sequence with increasing infiltration.

The higher average temperature of the Heavy house can clearly be seen in Figs. 5.4b, 5.5b: the Heavy curve fluctuates about a higher average compared to the Medium and Light models; more so in the winter. This illustrates that the mass is providing a stabilizing and a heating function. The heating is beneficial in the winter, but a drawback in the summer indicating that in conjunction with thermal mass, there is a need during the summer for passive techniques such as night time ventilation and limiting solar gain using blinds, shading or glazing coatings.

Figure 5.4a: Feb Outdoor and Indoor Temperatures; Reference Circuit and T_{sky} Modification (Solar, 0.33 ach)

Figure 5.4b: Feb Indoor Temperatures; Heavy (Reference), Medium and Light Circuits (Solar, 0.33 ach)
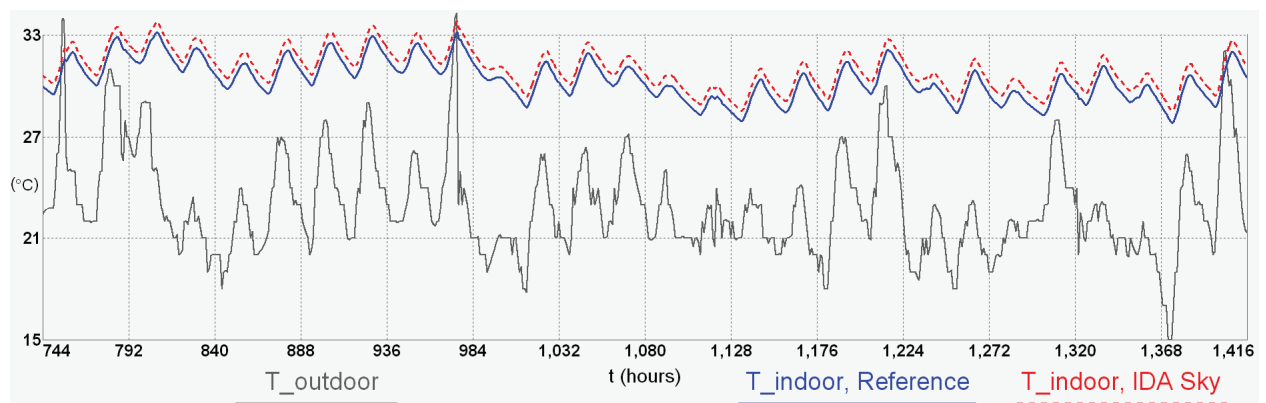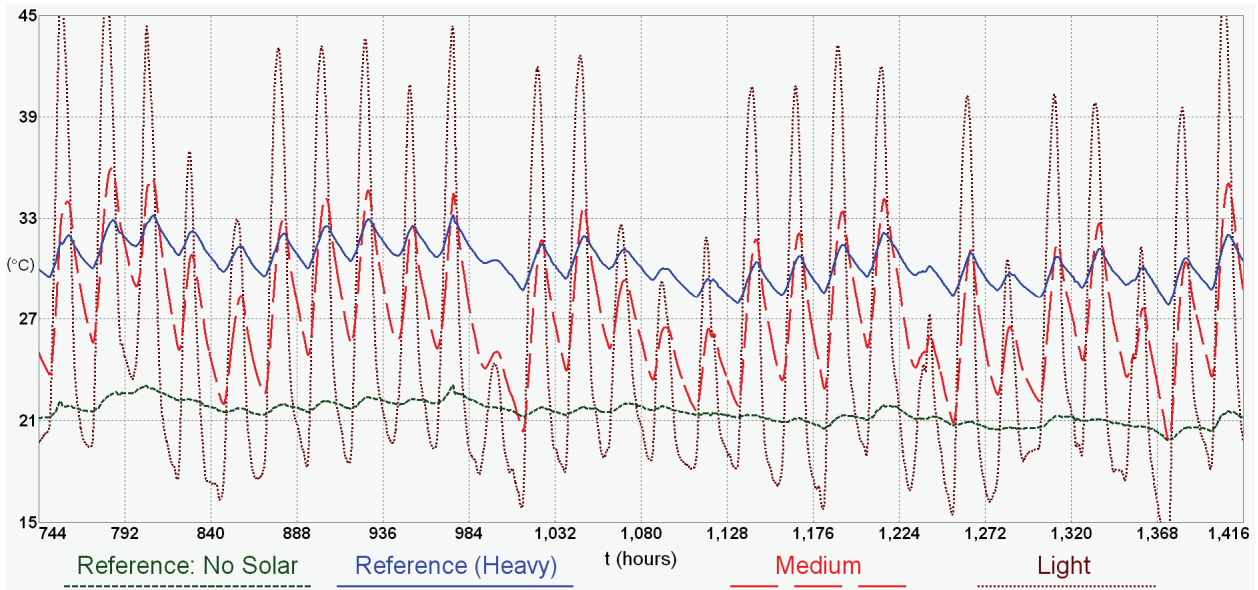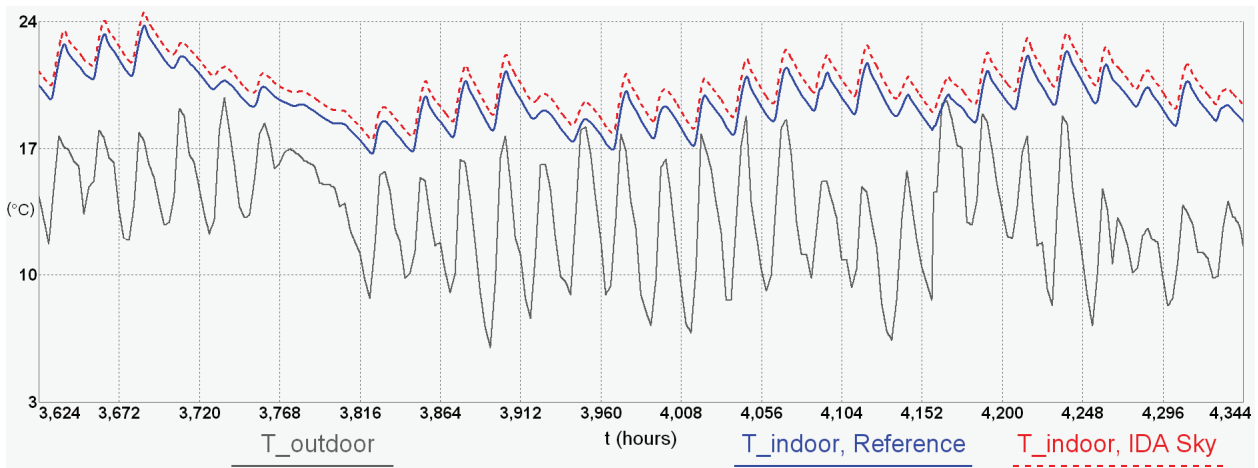

Figure 5.5a: June Outdoor and Indoor Temperatures; Reference Circuit and T_{sky} Modification (Solar, 0.33 ach)
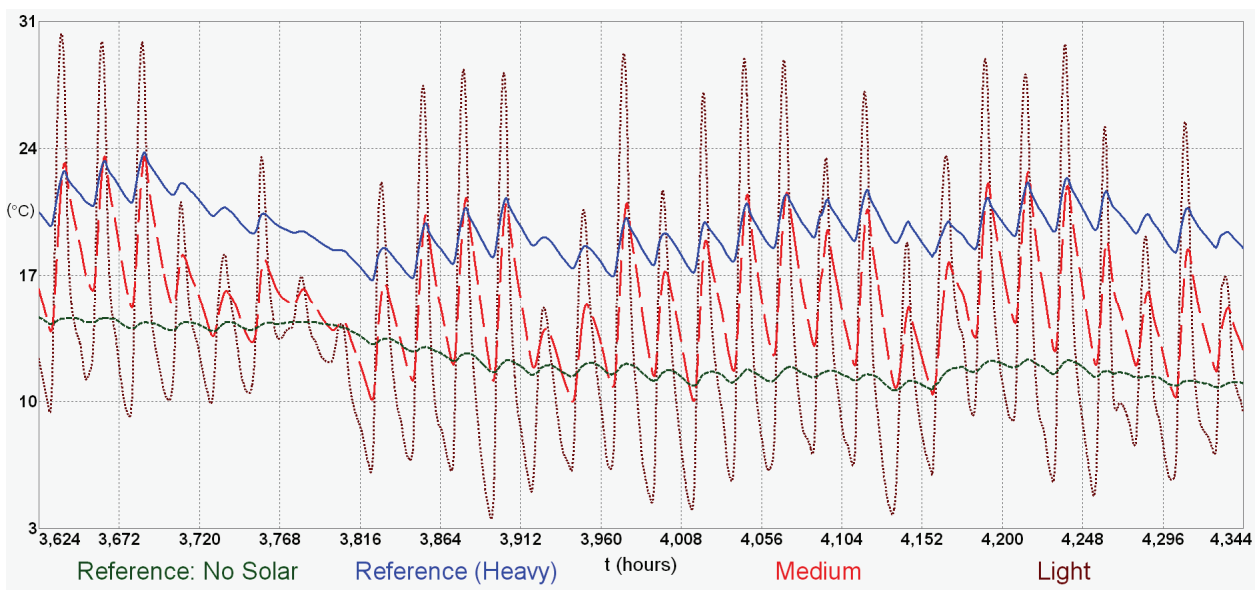

Figure 5.5b: June Indoor Temperatures; Heavy (Reference), Medium and Light Circuits (Solar, 0.33 ach)

5.3.4 Monthly Average Indoor Temperature Observations

• Daily, Monthly and Yearly Average Indoor Temperatures can be simply computed using a building model implemented with electric circuits and Micro-Cap. Hourly and sub-hourly temperatures may also be computed. The accuracy of these computations is limited by the climate data and chosen representations of both the physical properties and climatic elements (e.g. sky temperature).

• Circuit model implementations enable simple "what if" scenarios to be tested in order to investigate the impact of perturbing a physical or climatic property. For example, for the low energy house with and without solar input, dropping the sky temperature by approximately 7˚ resulted in the winter indoor average drop of 1˚ and a smaller drop during other months of the year. This drop decreased as the rate of infiltration increased.

• The average monthly temperatures for all models approach the average outdoor temperatures as the infiltration rate increases. At 10 ach, the monthly average outdoor temperatures of the heavy well insulated house are within 3-6% of the monthly average outdoor temperatures.

• The (Heavy) low energy house is fully exposed to the sun and has significant thermal mass providing beneficial heat storage in the winter but also results in unwanted heat retention in the summer. Large daily temperature fluctuations are damped with the June average temperature just below a comfortable level (19.7˚) while the February average is 30.4˚C. Comparing these averages to those for the same building and infiltration rate with *no solar input* re-enforces this observation. With no solar input, the approximate average for June is an uncomfortable 12.4˚C, while for February it is a comfortable 21.5˚C shown below in Table 5.6. Again, solar input is beneficial in the winter, but detrimental in the summer. The house would benefit from limiting solar input during summer using shading, blinds and/or glazing coatings.

Infiltration →	0.33 ach		10 ach	
	Feb	June	Feb	June
No Solar	21.5	12.4	22.7	13.3
Solar	30.4	19.7	23.6	14.0

Table 5.6: Circuit Computed Monthly Average Temperatures; Heavy Reference Model (˚C)

• Infiltration produces the opposite effect when considered in conjunction with solar input as shown above in Table 5.6. With 10 ach of infiltration, the February and June average temperatures are brought down significantly from 30˚C to 24˚C and from 20˚C to 14˚C respectively. This suggests that a ventilation regime such as night ventilation during the summer would help to counter the effect of solar gain during the summer.

• In addition to providing heat storage the significant thermal mass of the Heavy house reduces the indoor temperature variations compared to the Medium and Light houses (Figs. 5.4b and 5.5b).

5.4 Heating and Cooling Load Calculations

The heating energy required to maintain the indoor temperature at 20°C over June in the low energy house with 0.33 ach infiltration is determined for the Light, Medium and Heavy Reference circuit models with and without solar input. This is also repeated with the Heavy Reference circuit model using the original IDA sky temperature model.

5.4.1 Heating Load Computation

As described in *4.3.7*, in order to simulate a thermostatically controlled heater, a current source with a value expression similar to Eqn. 4.17 is added to the circuit (Fig. 4.6). For a heater, the value of the current source is proportional to the difference between the setpoint temperature and the temperature at the inner surface node of the lumped walls and ceiling (*surface* in Fig. 4.6). When the inner surface node temperature is above the setpoint temperature, the heater current source value is 0 (switched off).

Heating Load Without Solar Input

The June indoor temperature sequences computed using the Reference circuit without solar input and with both the heater active and disabled are shown in Fig. 5.6 below. Also shown in Fig. 5.6 are the heater output and the cumulative integral of heater output for the simulation with the heater active.
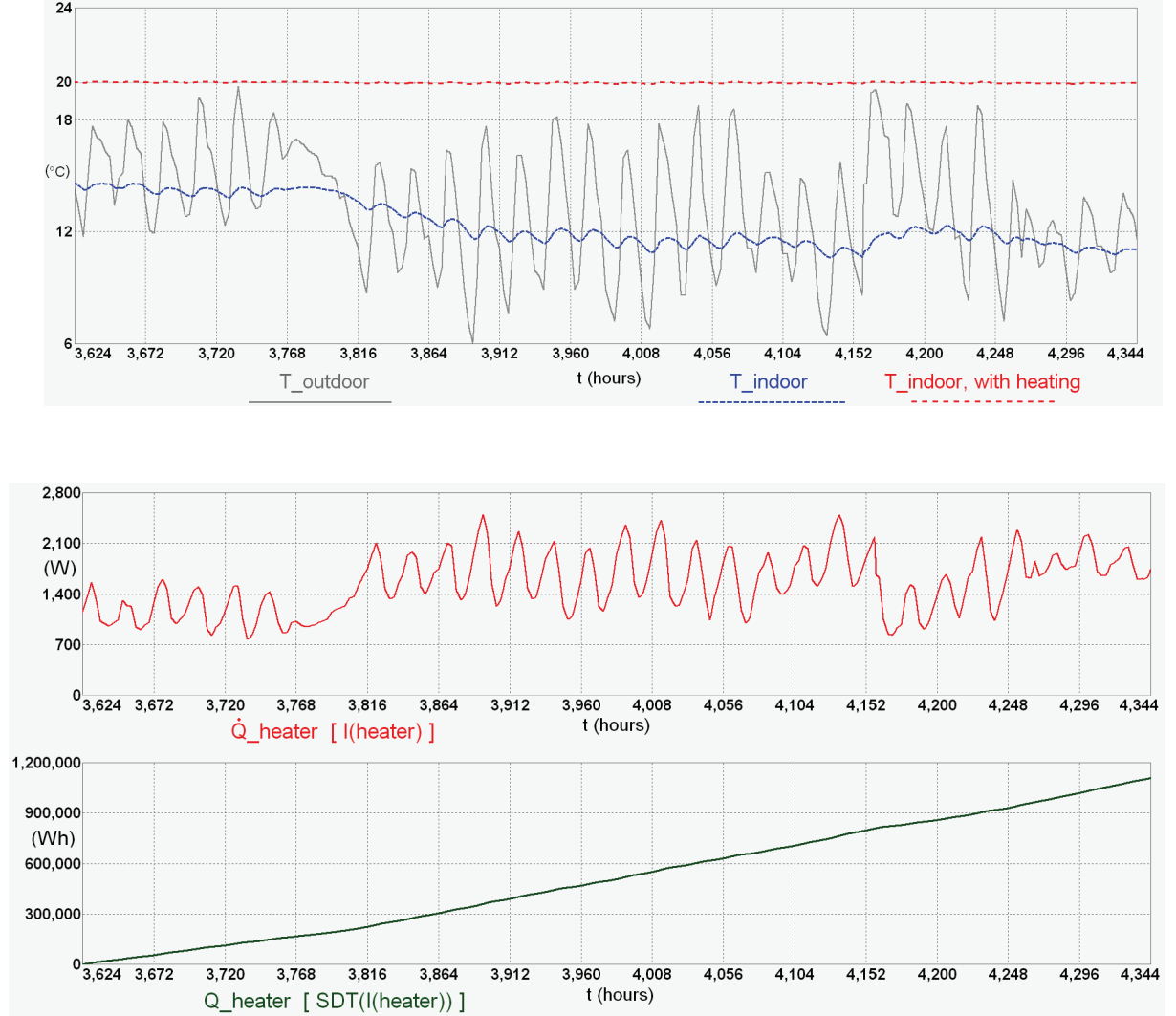
Figure 5.6: June Indoor Temperatures, Heater Output, Cumulative Integral of Heater, $T_{setpoint} = 20°C$, No Solar

From the lower graph of Fig. 5.6, the computed monthly heating load is the final value of the cumulative integral read either from the graph or the numerical output of the simulation run:

$$Q_{heating} = 1105.5 \ kWh$$

For this simulation, the heater is constantly on throughout the month and the resulting average indoor temperature is the setpoint temperature: $T_{in\_avg} = T_{setpoint} = 20°C$.

Heating Load With Solar Input

The June simulation output of the Reference circuit with solar input, 0.33 ach infiltration and the added heater current component is shown in Figs. 5.7a,b below. This illustrates the contribution of solar input to significantly reducing the June heating load.
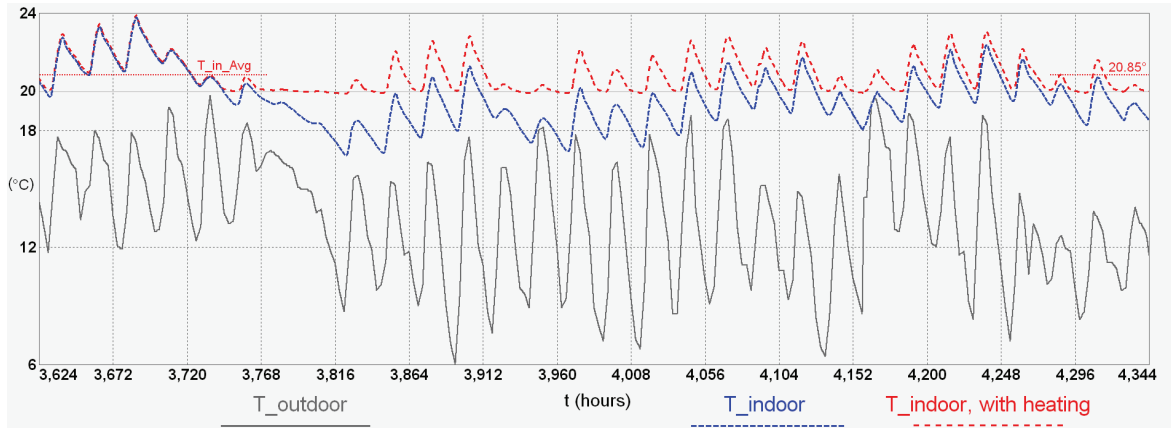
Figure 5.7a: June Indoor Temperatures With and Without Heating, $T_{setpoint} = 20°C$, Solar Input

For this simulation, the heater is not constantly generating heat throughout the month since the indoor temperature without mechanical heating (*T_indoor*, Fig. 5.7a) is often above the setpoint (20°C).
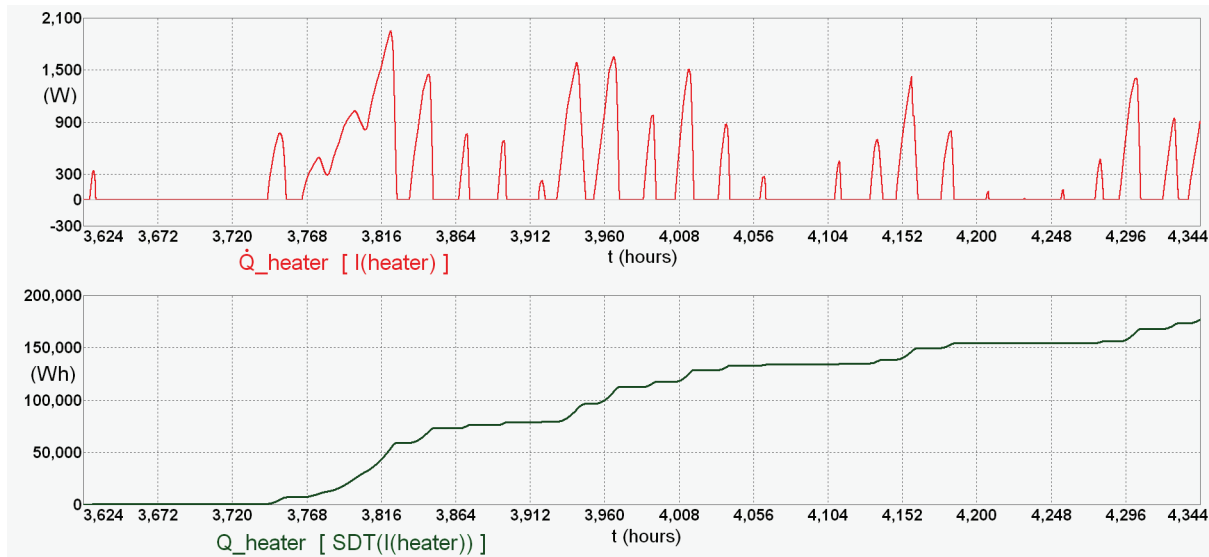
Figure 5.7b: June Heater Output and Cumulative Integral of Heater, $T_{setpoint} = 20°C$, Solar Input

Again, the computed monthly heating load is the final value of the cumulative integral read from the lower graph of Fig. 5.7b:

$$Q_{heating} = 177.98 \ kWh$$

Warm Sky Simulations

To investigate the significance of the clear sky temperature model of Bliss [70], the June heating load simulations with and without solar input are repeated with one change to the Reference circuit: the T_{sky_Bliss} component is replaced with the original warmer sky temperature of the IDA model: $T_{sky\_IDA}(t) = T_{outdoor}(t) - 5$. The resulting heating load computations are shown in column 1 of Table 5.7.

Discussion

Table 5.7 summarizes the circuit-based heating load computations for the Reference (Heavy) house model and three variations of the model with 0.33 ach infiltration and $T_{setpoint} = 20°C$.

	Heavy *T_{sky} : IDA	Heavy Reference	Medium	Light
No Solar	979.5	1105.5	2789.0	7398.1
Solar	94.8	178.0	1613.2	5601.5

Table 5.7: June Heating Load in kWh; Circuit-based Computations, 0.33 ach Infiltration. *$T_{sky\_IDA} = T_{outdoor} - 5$.

The values in this table clearly illustrate the significant contribution of solar insolation to the reduction of the winter heating load. Comparing "Solar" and "No Solar" loads, the Heavy Reference house is most effective at using the solar input to reduce the heating load (84%).

The first two columns of Table 5.7 illustrate the effect of lowering the sky temperature by approximately 7˚ (IDA → Reference). Clearly the increase in heating load is more significant when solar input is considered, illustrating that the choice of sky temperature models can have a significant impact on load calculations.

Table 5.7 illustrates a practical implication of a varying thermal inertia (τ, discussed in section 5.5). As the thermal inertia drops (Heavy→ Medium→ Light) the heating load increases very significantly.

The Medium and Light models listed in Table 5.7 have a different floor, wall and ceiling construction from the Heavy model (Table 5.2), resulting in reduced total thermal mass and reduced envelope resistance. To investigate the significance of the floor construction *only*, the heating load computation is performed for the Heavy Reference circuit with each of the three (Heavy, Medium, Light) floor types: Heavy: Thick Concrete; Medium: Thin Concrete; and Light: Timber. The resulting heating load values are shown in Table 5.8 below.

	Heavy Reference	Medium Floor	Light Floor
No Solar	1105.5	1112.0	1106.3
Solar	178.0	295.0	493.8

Table 5.8: June Heating Load (kWh); Heavy Reference Circuit Computations, Floor Construction Variation only.

Beneath each of these floor types is the *same* thick insulation (R-value: 6.5). Without solar input the change in floor type has an insignificant effect on the winter heating load. When solar input is included, the heavy floor improves the thermal performance due to the increased storage of solar input. The reduction in heating load due to floor construction changes is significantly less than the reduction due to walls and ceiling construction changes (compare Table 5.7, columns 3,4 to Table 5.8, columns 2,3). For a light building and assuming a low infiltration rate, more improvement in thermal performance can be achieved by adding insulation to the envelope compared to adding thermal mass.

5.4.2 Cooling Load Computation

The same technique is used to perform a monthly cooling load computation for the low energy house in February with a 24°C setpoint temperature, solar input and 0.33 ach infiltration rate. The case of no solar input is not considered. The only change to the model is the direction (polarity) of the current source component modelling the chiller (Fig. 4.8).

In Fig. 5.8 below, indoor temperature sequences, chiller heat transfer rate and cumulative chiller energy output are shown for February with solar input, as generated by the Reference circuit. This cooling load computation was repeated for the Light and Medium models as well as for two variations to the Heavy Reference models: (i) using the original warmer sky temperature of the IDA model and (ii) removing the floor insulation. The resulting cumulative chiller energy output for the Reference circuit and these four variants generated by Micro-Cap are shown in Fig. 5.8 below; resulting cooling load computations are listed in Table 5.9 below. T_{indoor} and $\dot{Q}_{chiller}$ are shown for the Reference model only.
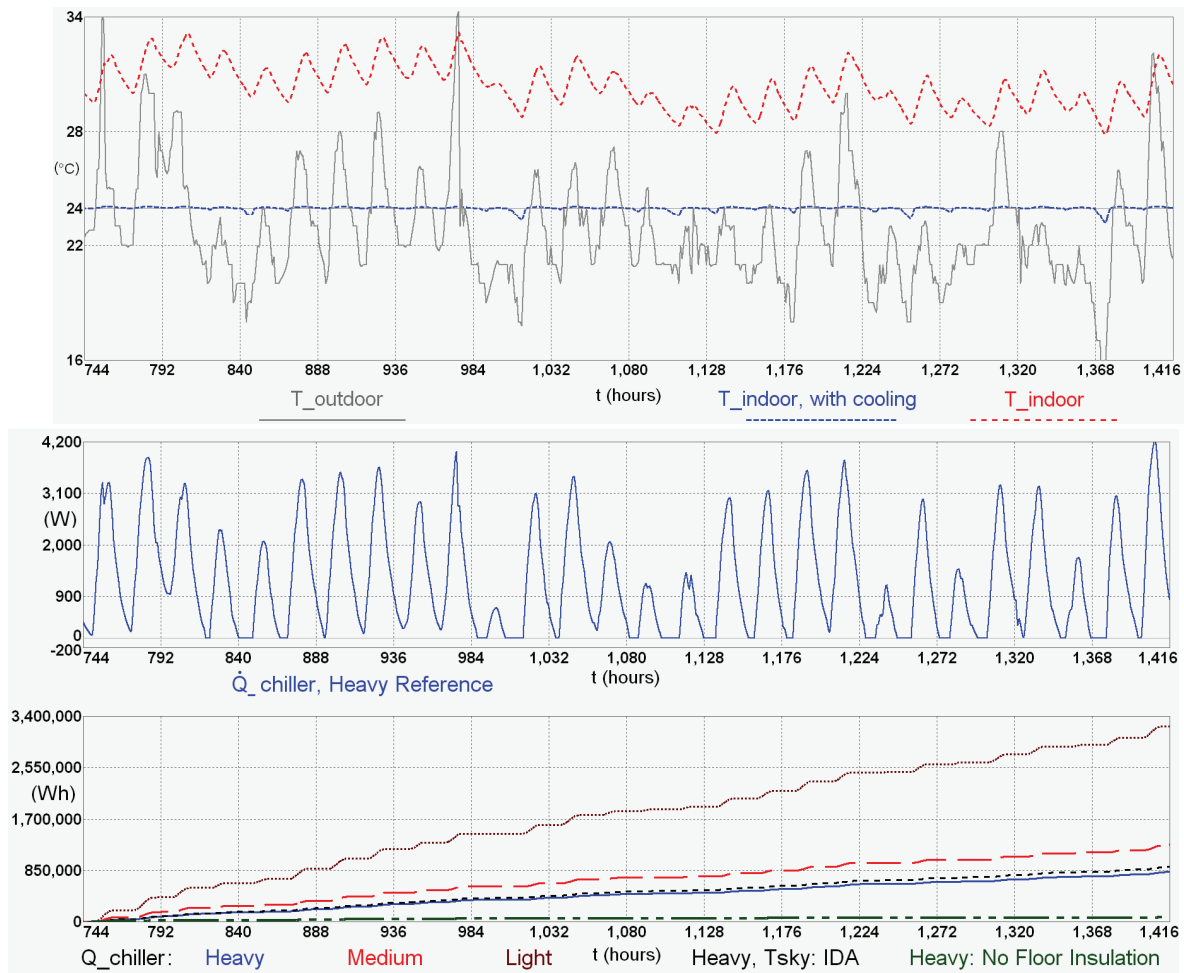
Figure 5.8: Feb Indoor Temperatures, Chiller Output and Cumulative Integral of Chiller, $T_{setpoint} = 24°C$, Solar

	Heavy Reference *T_{sky}* : IDA	Heavy Reference No Floor Insulation	Heavy Reference	Medium	Light
Solar	909.7	68.2	825.1	1263.7	3231.4

Table 5.9: February Cooling Load (kWh); Circuit Computations for 0.33 ach Infiltration. *$T_{sky} = T_{outdoor} - 5$.

Discussion

As expected, the cooler sky of the Reference model contributes to a lower cooling load (9.3%).

Even though at 0.33 ach the average February temperature for the Heavy house is 3° and 4.4° higher than the Medium and Light house, the cooling loads for the latter two houses are higher than the Heavy house load (Table 5.5). The increased mass of the Medium and Heavy houses damps the indoor temperature swings (Fig. 5.4b) contributing to the cooling load reduction. More significantly, the reduced envelope resistance (walls, ceiling) of the Medium house and to a greater degree, the Light house, results in these houses being less able to maintain the heat deficit between indoors and outdoors, compared to the Heavy house.

The second and third columns of Table 5.9 above illustrate the very significant effect of harnessing the ground temperature to reduce the summer cooling load. With no floor insulation, this cool temperature source charges the heavy mass at night when no solar input counteracts, providing a storage of cooling energy that is released during the daytime. During the day, the cool ground tempers the direct solar insolation on the mass. In contrast, with the original floor insulation (R-value: 6.5), this cool source is isolated from the house.

5.4.3 Heating and Cooling Observations

• Dropping the sky temperature by approximately 7° ($T_{sky\_IDA} \rightarrow T_{sky\_Bliss}$) resulted in the following monthly load changes: June heating load increased with solar (95 → 178W) and without solar (980 → 1106W) while Feb cooling load decreased with solar (910 → 825W).

• In terms of reduced winter heating and summer cooling loads, a light building will profit more from improved insulation than from improved thermal mass. Increasing thermal mass suitably exposed to solar input will lower heating loads due to heat storage in the mass.

• Thermal mass that is unprotected from solar exposure during the summer increases the cooling load. This again suggests limiting summer solar gain using blinds, shadings or glazing coatings. A night ventilation regime is another possible strategy for cooling mass during the summer.

• The Heavy (Reference) house has a significantly thermally massive floor. With insulation, heat storage in the floor is maintained with all the heat discharge to the indoor air and no discharge to the ground. This is a significant benefit in the winter (heating load reduction) but a weakness in the summer (cooling load increase). Without insulation, heat accumulated in the floor is able to discharge to the cool ground decreasing the amount of heat transferred to the air: a benefit in the summer but not in the winter. Because Sydney is a heating climate, insulating the thermally massive ground is the better choice. In addition, the amount of summer solar heat absorbed by the floor can be minimized by limiting the solar exposure of the house.

5.5 Building Time Constant (τ)

The computation of the Building Time Constant is presented for the Light, Medium and Heavy models of the low energy house using circuit models. A step change of 10˚ C is applied to each of the models shown in Table 5.2 above, with the indoor temperature response presented and discussed.

5.5.1 Computing τ Using Micro-Cap

Determining the Building Time Constant using a circuit model is based on the *Transfer Function* of the circuit: an expression comparing T_{indoor} and $T_{outdoor}$ shown in Eqn. 3.9. As such, the circuit model must be modified so that T_{indoor} is driven only by $T_{outdoor}$. This is done by setting $T_{gnd} = T_{sky} = T_{outdoor}$ (as modelled in the circuit of Fig. 6.1) and disabling solar input. The magnitude Bode plot (transfer function) of each circuit is then generated using *AC Analysis* in Micro-Cap. This is shown in Fig. 5.9 for the Light, Medium and Heavy circuits with 0.33 ach base infiltration rate. The corner frequency (f_B) is determined from either the Bode plot or the numerical output of the transfer function and τ is then calculated using Eqn. 3.9.
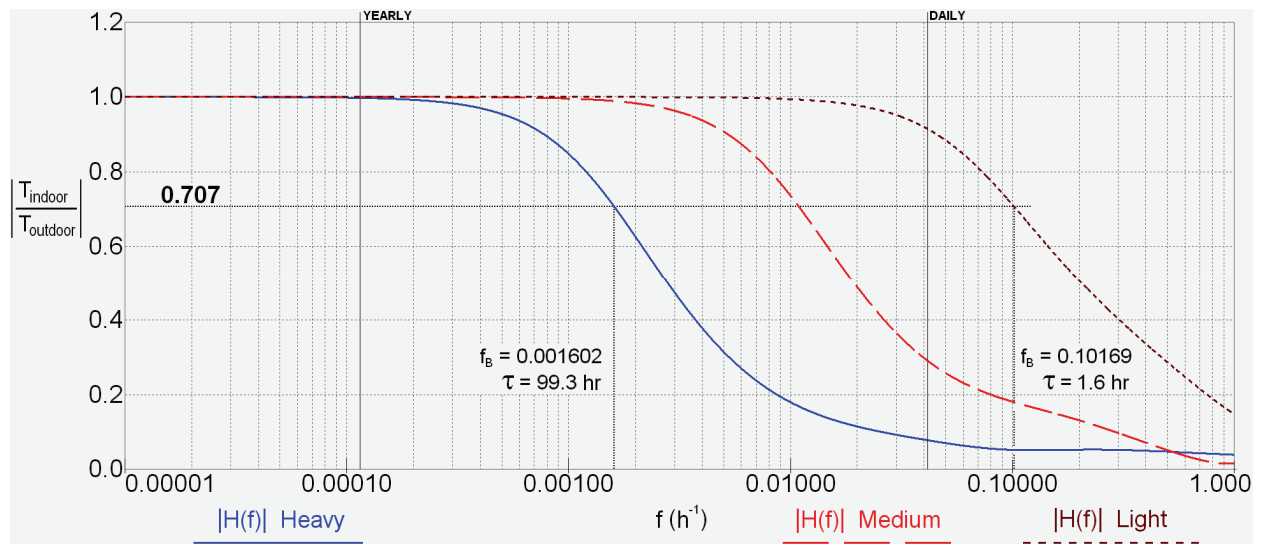
Figure 5.9: Circuit Generated Transfer Functions of the Low Energy House (0.33 ach); Light, Medium, Heavy

ACH	Heavy	Medium	Light
0	142.5	16.8	1.7
0.33	99.3	14.6	1.6
0.5	86.4	13.7	1.5
1	63.2	11.6	1.4
2	42.3	9.0	1.2
3	32.3	7.4	1.1
5	22.2	5.5	0.9
10	11.8	3.3	0.6
15	6.4	2.1	0.4

Table 5.10: Circuit Computed τ (hr) For Heavy, Medium and Light Houses at Varying Infiltration Rates

Discussion

A clear inverse relationship between τ values and infiltration rate can be seen from the data in Table 5.10 for all building weights. The impact that a changing infiltration rate has on τ, increases as the building weight increases: for example, the change from 1 to 2 ach infiltration produced a drop in the time constant $(\varDelta\tau)$ of 19.9, 2.6, and 0.2 h for the Heavy, Medium and Light houses respectively.

From a frequency response curve such as those in Fig. 5.9, it is straightforward to observe that for a building with significant thermal mass such as the Heavy low energy house, at the annual frequency $(f_y = 1/8760\,h = 0.0001141\,h^{-1})$, $|T_{indoor}/T_{outdoor}| = 1.0$, whilst at daily frequencies $(f_d = 1/24\,h = 0.0417\,h^{-1})$, has $|T_{indoor}/T_{outdoor}| < 0.08$. The temperatures inside the house will follow the yearly fundamental temperatures *(Period = 1 yr)* but will not follow the daily outdoor temperature fluctuations. The (Heavy) house acts as a low-pass filter of outdoor daily and hourly temperature fluctuations, allowing the low frequency annual temperature signal to pass while attenuating the high frequency daily temperature signal.

The Light circuit has a similar transfer function value at the annual frequency: $|T_{indoor}/T_{outdoor}| = 1.0$, but not at daily frequencies: $|T_{indoor}/T_{outdoor}| \approx 0.91$. The indoor temperature will follow daily outdoor temperature fluctuations with little attenuation. Higher frequency temperature fluctuations up to $f = 1/5\,h = 0.2\,h^{-1}$ are only attenuated by a maximum of 0.5. Compared to the Heavy building, it is clear that the Light building is thermally a less effective low-pass filter, resulting in more indoor temperature variation due to daily and hourly outdoor temperature variations.

The Medium building lies in between the Heavy and the Light with $|T_{indoor}/T_{outdoor}| = 0.29$ for daily frequencies $(f_d = 1/24\,h = 0.0417\,h^{-1})$ and $\tau_{medium} = 14.6\,h$. Clearly, the Micro-Cap computed τ values correctly order the three buildings in terms of increasing thermal inertia: Light, Medium and Heavy.

5.5.2 Indoor Air Response to a Cold Snap

A sudden 10˚ drop in outdoor temperature is applied to the Light, Medium and Heavy low energy house models with all circuit nodes, including the indoor temperature initialized to 21˚C $(T_0 = 21˚C)$. The same circuits and conditions used for the τ computations of the previous section are used here: $T_{gnd} = T_{sky} = T_{outdoor}$, infiltration rate is 0.33 ach and solar input is disabled. The indoor temperature response to the cold snap for these circuits and the Heavy model with 10 ach infiltration are shown in Figure 5.5 below.
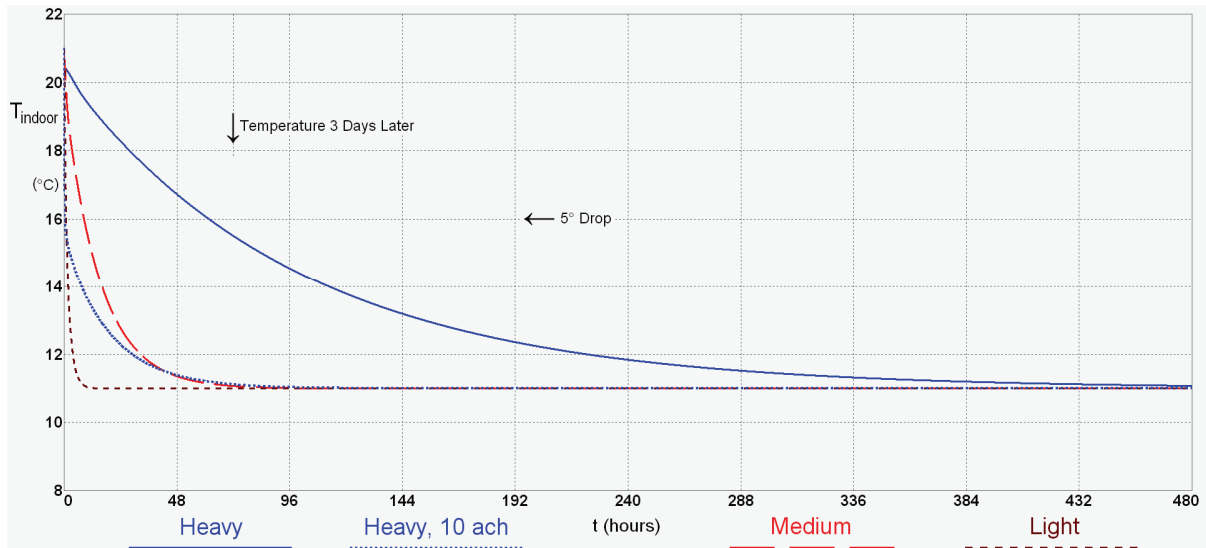
Figure 5.10: Circuit Model Responses to a 10° Drop for $ach = 0.33$, except as indicated; $T_{indoor}(0) = 21˚C$

The responses of the Heavy and Light circuits reflect the difference in magnitude of the building time constants shown in Table 5.2: at 0.33 ach they differ by 2 orders of magnitude. The relative steepness of the Light building decay curve clearly illustrates this. Again, the Medium circuit response lies between the Light and Heavy responses. The time required for the indoor temperature to reach 16˚C (5˚ drop) in the Heavy, Medium and Light buildings are 60 hours, 8 hours and 30 minutes, respectively.

Figure 5.10 illustrates the effect that a high infiltration rate has on the Heavy circuit response: the response is approximately between the Medium and Light circuit responses. It takes 21 minutes for the Heavy building with 10 ach infiltration to reach 16˚C. This is *less* than the time required for the Light building to reach the same temperature.

5.5.3 Building Time Constant Observations

• Micro-Cap enables the simple computation of the Building Time Constant (τ) from the circuit model of a building. This computation correctly ordered the Light, Medium and Heavy versions of the low energy house in terms of increasing thermal mass indicating increasing thermal inertia. The indoor air temperature response to a sudden drop in temperature also indicated this ordering of increasing thermal inertia. As the infiltration rate increases, τ and the thermal inertia of the building decrease. The time constant of a heavier building is impacted by infiltration rate changes more so than a lighter building.

75

• Although both measures are based on Thermal Capacitance *(C)*, τ is a better measure of thermal inertia than Szokolay's Specific Mass *(sM)*. τ is a function of both *C* and the net resistance between the indoor and outdoor air *(R_T)* while *sM* is a function of the mass of the envelope *(kg)* and the floor area *(m^2)* (Eqn. 2). τ is directly impacted by ventilation and infiltration rates while *sM* is not impacted at all.

For the Heavy house with 10 ach infiltration, the circuit response to a 10° drop in outdoor temperature lies between the responses of the Light and Medium buildings with 0.33 ach infiltration. This shows the direct impact of infiltration on the thermal inertia of the house and is also reflected in the building time constant values: $\tau_{medium\_0.33ach} = 14.6\ h$, $\tau_{heavy\_10ach} = 11.8\ h$, $\tau_{light\_0.33ach} = 1.6\ h$.

• A weakness of τ is that the same τ can be computed for very different buildings. For example: the Heavy Reference house with 0.33 ach infiltration and the same house with the thickness of the concrete floor increased by a factor of 10 (1500 mm) and with 5.3 ach ventilation ("*Heavy,10x_C-Flr*"). For these two very different buildings, the same τ value is computed when using the corresponding circuits as shown in Figure 5.11 below. In terms of τ, the decrease in R_T due to the increased infiltration rate of 5.3 ach is counterbalanced by the 9-fold increase in C_T.

From Fig. 5.11, it is clear that the thermal performance of these two buildings is very different: for daily frequencies of outdoor temperature fluctuations, $|T_{indoor}/T_{outdoor}| < 0.08$ for the Heavy Reference house and $|T_{indoor}/T_{outdoor}| \approx 0.45$ for the *Heavy,10x_C-Flr* house. Without artificial heating, the temperatures inside the *Heavy,10x_C-Flr* house will vary significantly more than the Heavy house due to daily and hourly outdoor temperature variations.
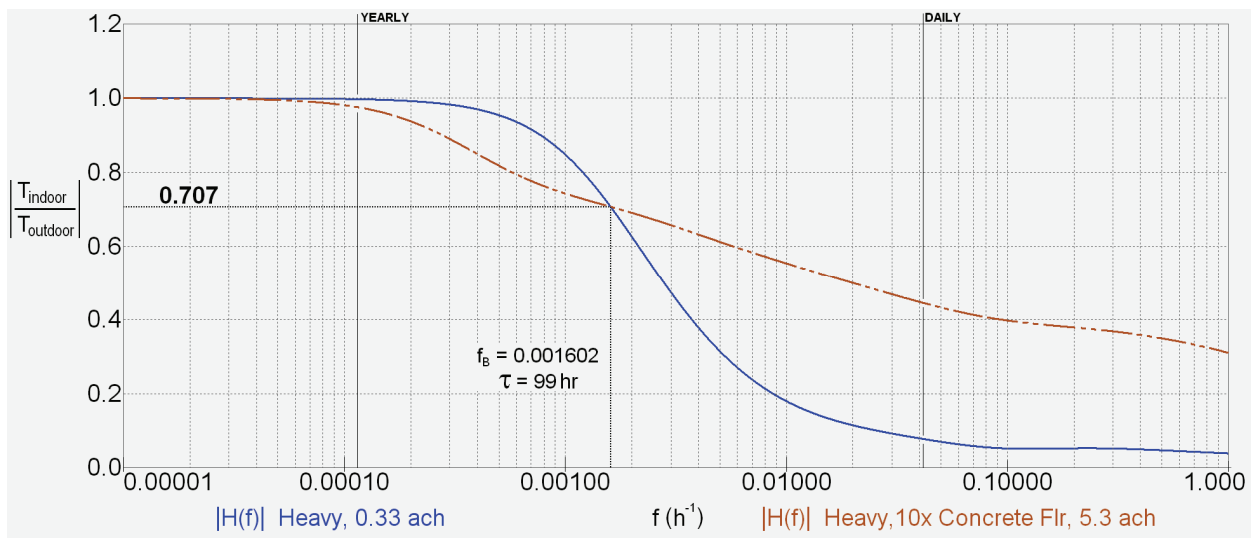

Figure 5.11: Equal τ Computed from Transfer Functions *|H(f)|*; Heavy Reference (0.33 ach); Thick Floor, 5.3 ach

The differing thermal inertia of these two buildings can also be seen in the corresponding circuit responses to an outdoor temperature drop of 10° shown in Figure 5.12 below. The *Heavy,10x_C-Flr* house experiences a faster initial drop in indoor temperature than the Heavy house due to the fast heat transfer between the cooler air and the indoor air resulting from a much higher infiltration rate. At a later time, when the response is dominated by heat transfer between the thermal mass and the indoor air, the *Heavy,10x_C-Flr* house decays at a slower rate toward the 11° C steady-state temperature due to the ten-fold thermal mass in the floor, compared to the Heavy house.
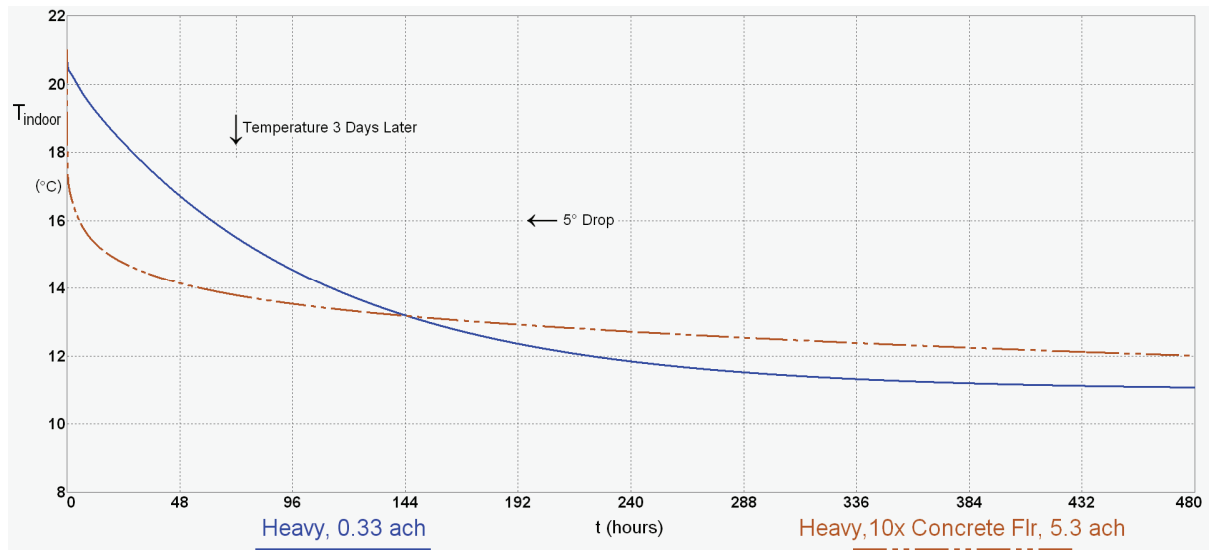
Figure 5.12: Circuit Model Responses to a 10° Outdoor Drop for Two Houses with Equal τ; $T_{indoor}(0) = 21°C$

• Micro-Cap can generate the magnitude Bode plot (transfer function) of a building circuit model. This is a useful tool to illustrate a building's response to a frequency spectrum of outdoor temperature variations, including daily and yearly variations. As illustrated in Fig. 5.11, the Bode plot provides more information and a better indication of the thermal inertia of a building than τ alone, enabling the divergent thermal responses of different buildings with the same τ-value to be easily distinguished.

5.6 Chapter Summary

In this chapter, the thermal inertia of the low energy house, average indoor temperatures and heating/cooling loads were investigated through simulations using RC circuit models and Micro-Cap. Variations of the house construction (infiltration rate, thermal mass and envelope resistance) and climatic variables (solar input, sky temperature) were modelled to investigate their significance. The following observations are drawn from simulation output:

• The low energy house is fully exposed to the sun and has significant thermal mass providing beneficial heat storage in the winter but also results in unwanted heat retention in the summer. During the summer, the house would benefit from limiting solar input and implementing a ventilation scheme such as night ventilation. This significance of solar input is also seen in the contribution to meeting winter heating loads.

• Reducing the sky temperature by 7 degrees $(T_{sky\_IDA} \rightarrow T_{sky\_Bliss})$ results in a winter monthly average temperature drop of 1°C. During other months, the averages drops by a smaller margin and for all months, this drop decreases as the rate of infiltration increases. The June heating load and February cooling load increases and decreases by approximately 84W respectively. The required modelling accuracy would dictate the significance of these effects.

• Increasing the thermal mass of a house decreases indoor temperature variation and increases the monthly average temperature. The increase diminishes as the rate of infiltration increases.

• For a light uninsulated building, adding insulation alone compared to adding thermal mass alone, reduces the heating and cooling loads more. Increasing thermal mass suitably exposed to solar input will lower heating loads due to heat storage in the mass.

• Significant thermal mass needs to be managed in terms of solar exposure with winter exposure maximized and summer exposure minimized.

Thermal Inertia

A simple procedure for computing the building time constant from a circuit model $(\tau_{circuit})$ was presented. τ is a better measure of thermal inertia than Szokolay's *Specific Mass (sM)* as the latter does not include envelope resistance and infiltration/ventilation whereas τ does. Regardless, using computations based on τ to predict the indoor temperature response to outdoor temperature step changes has two limitations when infiltration or ventilation is present.

Firstly, the response is not governed by a single time constant assumed by the common usage of τ but rather two: τ_1, due to indoor and outdoor air mixing and τ_2, due to heat transfer between the mass and indoor air. The circuit response under Micro-Cap correctly reflects this: the response curve suggests a lower τ value than τ computed using the circuit-based procedure described in section 5.5.1. The effects of τ_1 and τ_2 can be easily seen in a response where a high infiltration rate is involved (Figs. 5.10, 5.12).

Secondly, using the circuit-based procedure, two buildings with very different constructions can produce the same τ value and divergent thermal responses as shown in the Figs. 5.11 and 5.12. In contrast, the bode plot distiguishes two such buildings: for each, the thermal inertia is illustrated by displaying the differing responses to a frequency spectrum of outdoor temperature variations (e.g.: daily, yearly).

6 Comparing Circuit Model Computations with Manual Calculations

In Chapter 4, the simulation results produced by two implementations of a thermal model of the low energy house were compared and presented: the IDA ICE model and the equivalent circuit model utilising Micro-Cap. The comparison was limited to computed hourly indoor air temperature sequences and the comparison was not transparent since the physical assumptions and computation details forming the basis of the IDA modelling of infiltration and solar radiation, where not fully known.

In this chapter, a simple thermal model is presented and applied to the low energy house. This *Manual* model is grounded in basic thermal principles such as energy balance and established physical laws governing the relationships between energy, heat transfer and temperature. The model falls into the *Lumped Model* category (described in Ch. 2) and includes assumptions about physical characteristics of the house and climate that simplify its development and use, but also limit its accuracy under certain circumstances. The low energy house has a well insulated envelope and contains significant thermal mass in the floor. When the outdoor temperature is assumed to be the only active thermal force, then the house maintains a steady indoor temperature that follows the yearly outdoor temperature harmonic. Under these conditions the Manual lumped model produces good predictions of temperature and heating/cooling loads. When dynamic thermal phenomina are included in a modelling scenario (e.g. hourly solar radiation), then the Manual model becomes less accurate.

Even though the Manual lumped model is less accurate than a transient model (e.g. the IDA model of Ch 4), it is transparent: the grounding, assumptions and limitations of this model are known and therefore it provides a reliable reference. In addition, with the model limitations known, discrepancies between circuit and Manual model preditions can be explained and highlight the accuracy of the circuit model. For example circuit models incorporate dynamic thermal phenomina more accurately than the Manual model.

The aim of the comparison of this chapter is to supplement the circuit modelling verification of Ch. 4 based on a more transparent comparison than presented in Ch. 4. In order to ensure an unbiased comparison, most of the simplifications and assumptions entailed in the Manual model are applied to the Reference circuit model of Ch. 5. The resulting circuit model as well as the assumptions, limitations and derivation of the Manual model are presented in section 6.1 that follows.

The simulation computations compared in this chapter are a subset of those presented in Chapter 5:

(i)   monthly average indoor temperatures
(ii) monthly heating loads
(iii) the building time constant

6.1 The Simple Manual Model

This model is based on an energy balance of a house as a lumped system with five simplifications:

(i) All thermal mass is summed into one capacitance and all thermal resistance is summed into one resistance and these lumped values completely represent the house (including the indoor air) as a single node.

(ii) Both ground and sky temperatures are modelled using the outdoor temperature directly:
$$T_{gnd} = T_{sky} = T_{outdoor}.$$

(iii) All outer surface resistances are approximated using one *static* value. This contrasts the modelling of outer surfaces of the Reference circuit that is based on 3 parallel *dynamic* heat transfer paths: radiative heat transfer between outer surfaces and sky/ground and convective heat transfer (a function of surface orientation and hourly wind speed/direction).

(iv) Only solar gain through glazing is considered. Solar radiation absorbed by the opaque envelope is ignored.

(v) Both the circuit model and the manual calculations use outdoor temperature and irradiance data from IWEC Sydney weather file as input. The manual calculations use monthly *averages* of this data while the circuit model uses the original hourly data values of the weather file.

These simplifications impact the accuracy of the Manual model. Assumptions (ii) through (iv) simplify the physical interpretation of the modelling scenario. A sensitivity analysis of each assumption could be performed in order to determine the significance of each assumption. This is not necessary for the purposes of the comparison of this chapter since these assumptions are reproduced in the circuit model (Fig. 6.1).

Assumptions (i) and (v) are not reproduced in the circuit model, although the data that underpins these assumptions is used in the equivalent circuit modelling. Lumping all of the thermal capacitance into a single node limits the accuracy of the Manual model when dynamic temperatures occur in the house in response to dynamic outdoor temperatures. If the house is in steady-state during a simulation period, then this limitation vanishes and the accuracy of the Manual model can assumed. Using monthly averages for solar and temperature inputs to the Manual model limits temperature predictions to monthly or lengthier averages: specific daily or hourly temperature prediction is not possible. The equivalent circuit model is driven by hourly solar and temperature input with nodal temperatures and heat transfer rates computed on a sub-hourly basis. The equivalent circuit model does not lump capacitance into a single node. The modelling of thermal capacitance

described throughout this thesis accurately models the diffusion of heat through thermal capacitance over time.

6.1.1 Derivation of the Manual Model

The starting point is a balance of the energy gains and losses of the house during a time interval dt:

Change in Energy Stored = Energy Gains − Energy Losses

$$C_T dT_{in} = dQ_{inputs} - dQ_{outputs}, \qquad\qquad C_T = \sum_{i=1}^{n} m_i c_i \qquad (1)$$

Where: C_T is the total *lumped apparent* thermal capacitance of the house (J/°C) [53]

m_i is the mass of element i (kg)

c_i is the specific heat of element i (J/kg·°C)

T_{in} is the (*spatial*) average temperature of the mass and indoor air of the house (°C)

dQ_{inputs} is the average heat gain into the house: envelope gains, solar i/p, heating, etc

$dQ_{outputs}$ is the average heat loss out of the house: envelope losses, cooling, etc

Here, a *positive dQ* indicates heat *into* the house. Gains are taken to consist of solar gains and artificial heating. Gains due to occupants and appliances are not considered. These latter gains can easily be included and incorporated in a circuit model, but are not specifically analysed in this thesis.

This results in:

$$C_T dT_{in} = G_{incident} \cdot A_w \cdot SHGC \cdot dt + dQ_{heating} - dQ_{cooling} - dQ_{envelope} \qquad (2)$$

Where: $G_{incident}$ is the average irradiance incident on the glazing over dt (W/m^2).

dt is the time period in seconds, over which the heat gains/losses take place.

A_w is the total glazing area of the house (m^2)

$SHGC$ is the solar heat gain coefficient

$dQ_{envelope}$ is positive or negative based on heat flow direction through the envelope

SHGC is the areal average of the *SHGC*s for the different types of glazing of the envelope. The low energy house analysed in this thesis uses one type of glazing and therefore averaging is not necessary. Including the equation for the heat transfer rate through the house envelope gives:

$$C_T dT_{in} = G_{incident} \cdot A_w \cdot SHGC \cdot dt + dQ_{heating} - dQ_{cooling} - \frac{(T_{in} - T_{out\_avg})}{R_T} dt \qquad (3)$$

Where T_{in} is the varying indoor temperature, T_{out_avg} is the average outdoor temperature over the time period dt and R_T is the *net* thermal resistance between the inside and outside air (°C/W). The calculation of R_T (Eqn. 4) takes into account all thermal paths between inside

and outside air and includes a resistance term derived from infiltration rates as described in section 3.2 (see Appendix E for a summary of this calculation for three infiltration rates). A similar ventilation resistance term would appear in Eqn. 4 if ventilation were being modelled.

$$\frac{1}{R_T} = \frac{1}{R_{wf}} + \frac{1}{R_g} + \frac{1}{R_{sip}} + \frac{1}{R_{floor}} + \frac{1}{R_{infiltration}} \qquad (4)$$

Here, the subscripts are *wf*: window frames, *g*: glazing, and *sip*: structural insulated panels. In Eqn. 3, *dt* can be a time span during which there is no solar insolation (e.g. during the evening). In this case, $G_{incident} = 0$.

Manual Calculation of Heating/Cooling Loads and Average Indoor Temperatures

Heating and cooling load calculations assume the house is in steady-state. Over the considered time period *dt*, the indoor temperature is assumed to remain constant *(dT_in = 0)* at an average temperature *(T_in(t) = T_{in_avg})* at or near the setpoint temperature.

The average heating and cooling rates $(\dot{Q}_{heating}, \dot{Q}_{cooling})$ (W) over *dt* are defined implicitly as

$$dQ_{heating} = \dot{Q}_{heating} \cdot dt, \qquad dQ_{cooling} = \dot{Q}_{cooling} \cdot dt$$

and with *dT_in = 0*, Eqn. 3 becomes

$$G_{incident} \cdot A_w \cdot SHGC \cdot dt + \dot{Q}_{heating} \cdot dt = \dot{Q}_{cooling} \cdot dt + \frac{(T_{in\_avg} - T_{out\_avg})}{R_T} \cdot dt \qquad (5)$$

and

$$G_{incident} \cdot A_w \cdot SHGC + \dot{Q}_{heating} = \dot{Q}_{cooling} + \frac{(T_{in\_avg} - T_{out\_avg})}{R_T} \qquad (6)$$

The four heat transfer rates of Eqn. 6 are in Watts. If other internal gains (occupants, appliances, etc) were being considered, then equivalent terms to $\dot{Q}_{heating}$ such as $\dot{Q}_{occupants}$ would appear on the left-hand side of Eqns. 5, 6. In addition to heating and cooling load calculations, Eqn. 6 is used to calculate average indoor temperature by solving for T_{in_avg} when the other variable values are known.

Manual Calculation of Building Time Constant (τ)

The treatment of the Building Time Constant in the literature is presented in section 2.2. The approach adopted here for verifying circuit computations of *τ* is the simplest of the three approaches presented by Antonopoulos [47] which treats the house as a single lumped mass:

$$\tau_{manual} = R_T C_T \qquad \text{where } R_T \text{ is defined by Eqn. 4 and } C_T \text{ is defined by Eqn 1.} \qquad (7)$$

Eqn. 7 does not require empirical temperature data and is the formulation adopted by the ISO [51]. Antonopoulos points out that the use of C_T (*apparent* thermal capacitance) *can* lead to significant over estimates of τ [47, 53]. Herein, C_T is referred to as the *lumped* thermal capacitance of a building.

With $G_{incident} = 0$, $dQ_{heating} = 0$, $dQ_{cooling} = 0$ and $\tau = R_T\,C_T$, an explicit expression for $T_{in}(t)$ is derived from Eqn. 2 as shown in Appendix H:

$$T_{in}(t) = T_{out\_avg} + (T_{in\_0} - T_{out\_avg})e^{-\frac{t}{\tau}} \qquad\qquad T_{in\_0} = T_{in}(0) \qquad\qquad (8)$$

This is a variant of Newton's law of cooling, with the indoor temperature tending towards T_{out_avg} : as $t \to \infty$, $T_{in} \to T_{out\_avg}$. Eqn. 8 is useful for estimating the indoor temperature response to an outdoor temperature step change to T_{out_avg}. (see section 6.4.1).

The manual calculation of the building time constant of the low energy house (Eqn. 7) with four infiltration rates is shown in Appendix E. Eqns. 6, 7 and 8 are used to make calculations that are compared to the corresponding circuit model computations in the sections that follow.

6.1.2 Verification Circuit Model

The Manual model includes five simplifications listed at the start of this section (6.1). Of these, the three simplifications impacting the physical parameters of the low energy house assumed by the Reference circuit model are: static outer surface resistances, $T_{gnd} = T_{sky} = T_{outdoor}$ and ignoring solar radiation absorbed by the opaque envelope. In order to make a fair comparison between Manual and circuit models results, these simplifications are applied to the Reference Model (Fig. 5.3) resulting in the Verification circuit model shown in Fig. 6.1 below.
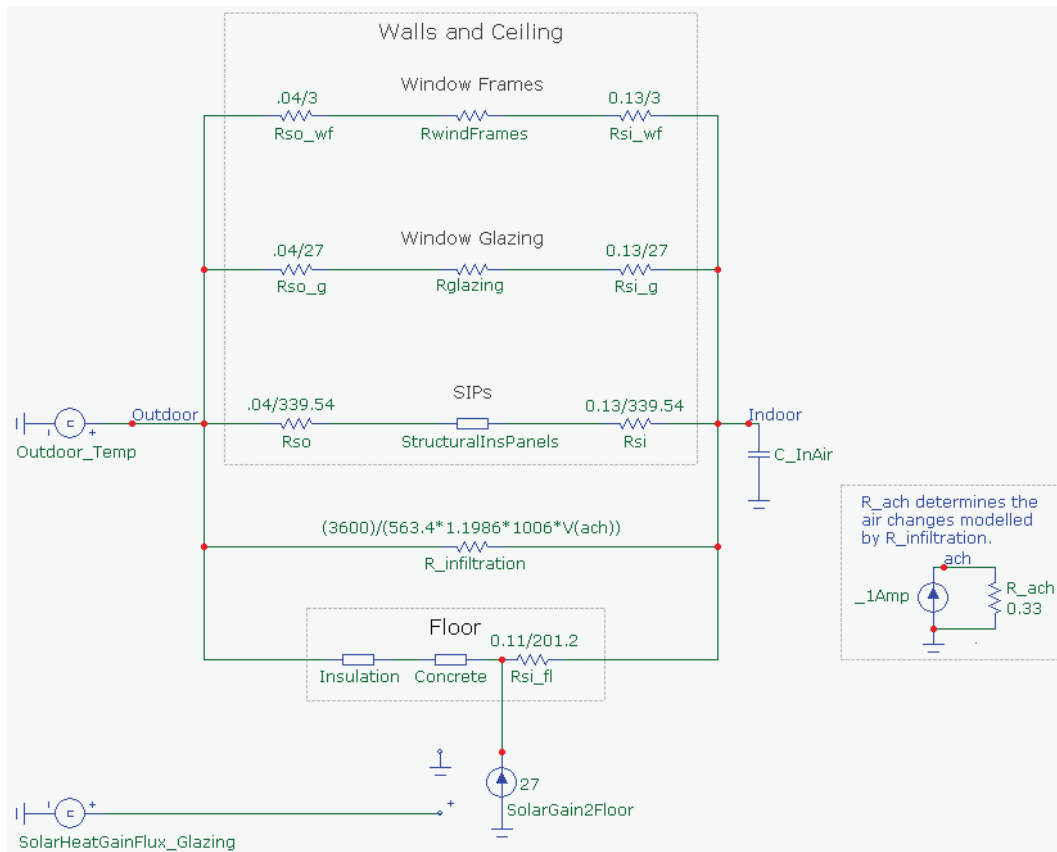
Figure 6.1: (Heavy) Verification Circuit Model Incorporating Equivalent Assumptions of the Manual Model

This circuit is used to produce output for simulations with and without solar input: to run a simulation without solar input, the circuit component modelling solar gain *(SolarGain2Floor)* is first disabled.

Being a simplification of the "Heavy" Reference circuit, this circuit is referred to as the "Heavy" Verification circuit. The same thermal mass variations to the low energy house applied to the Reference Circuit of Ch. 5 are here applied to the Verification circuit to compare building time constant estimates for varying building weights, to the corresponding Manual model estimates.

6.2 Monthly Average Indoor Temperature

In this section, monthly average indoor temperatures as computed by the (Heavy) Verification circuit (Fig. 6.1) with and without solar input are compared to the corresponding Manual model calculations. The equations used to calculate indoor temperature averages using the Manual model are presented followed by a table of differences between monthly indoor average temperatures calculated by the Manual model and computed by the Verification circuit *without* solar input. This is repeated *with* solar input included and is followed by a brief discussion of these results.

Verification Without Solar Input

Assuming steady-state conditions and with no solar, heating and cooling inputs $(G_{incident} = \dot{Q}_{heating} = \dot{Q}_{cooling} = 0)$, Eqn. 6 of the Manual model becomes:

$$T_{in\_avg\_Man} = T_{out\_avg} \qquad (9)$$

Regardless of the infiltration rate, the Manual model estimates the monthly average indoor temperature ($T_{in\_avg\_Man}$) to be equal to the monthly average outdoor temperature. The difference between the manual calculation and the Verification circuit computation of monthly averages is:

$$\Delta = |T_{in\_avg\_Man} - T_{in\_avg\_Ver}| = |T_{out\_avg} - T_{in\_avg\_Ver}| \qquad (10)$$

Table 6.1 below lists the monthly average indoor temperature manually calculated directly from the IWEC weather data and computed by the Verification circuit with no solar input and 0.33 infiltration rate. Also shown are the differences between the manual calculation and circuit computation for various infiltration rates. All nodes of the Verification circuit were initialized to 21˚C.

Month	$T_{in\_avg\_Man}$	$T_{in\_avg\_Ver}$	$\Delta = |T_{in\ avg\ Man} - T_{in\ avg\ Ver}|$					
ACH →		0.33	0	0.33	1	3	5	10
Jan	22.03	21.86	0.224	0.173	0.120	0.059	0.037	0.019
Feb	22.86	22.85	0.046	0.019	0.013	0.025	0.027	0.021
Mar	21.30	21.52	0.290	0.219	0.170	0.121	0.095	0.060
Apr	18.66	18.93	0.435	0.268	0.131	0.042	0.025	0.014
May	15.93	16.22	0.456	0.286	0.155	0.056	0.030	0.012
June	13.37	13.87	0.646	0.502	0.352	0.180	0.117	0.061
July	12.29	12.40	0.168	0.114	0.059	0.008	0.002	0.005
Aug	13.57	13.30	0.363	0.268	0.178	0.086	0.055	0.029
Sep	15.27	14.77	0.609	0.504	0.374	0.207	0.141	0.077
Oct	18.37	18.41	0.114	0.036	0.120	0.116	0.090	0.056
Nov	19.75	19.39	0.441	0.361	0.271	0.153	0.107	0.062
Dec	21.19	20.93	0.411	0.256	0.131	0.047	0.027	0.013
Yearly	17.85	17.84	0.018	0.013	0.008	0.004	0.003	0.002

Table 6.1: Average Indoor Temperature Comparison; Manual Model vs Circuit Model (˚C), no Solar Input

Verification with Solar Input

The above monthly average indoor temperature comparison is repeated with solar input included. With solar input, but no heating and cooling inputs included ($\dot{Q}_{heating} = \dot{Q}_{cooling} = 0$), Eqn. 6 becomes:

$$T_{in\_avg\_Man} = T_{out\_avg} + G_{incident} \cdot A_w \cdot SHGC \cdot R_T \qquad (11)$$

This results in the Manual model estimate of monthly average indoor temperature decreasing as the infiltration rate increases, since $R_T \downarrow$ as $ACH \uparrow$.

A summary of the differences (Δ) in monthly average indoor temperature estimates made by the two models when solar radiation is included, is given in Table 6.2 below. The monthly average temperatures (Manual and Verification circuit models) are shown for 0.33 ach infiltration only. For circuit computations, all nodes of the Verification circuit were initialized to just below the average January indoor temperature which varied with infiltration rate, for example, 0.33 ach: $T_0 = 29\,°C$; 3 ach: $T_0 = 24\,°C$.

Month	$T_{in\_avg\_Man}$	$T_{in\_avg\_Ver}$	$\Delta = |T_{in\ avg\ Man} - T_{in\ avg\ Ver}|$					
ACH →	0.33	0.33	0	0.33	1	3	5	10
Jan	29.57	29.31	0.420	0.260	0.183	0.074	0.054	0.032
Feb	30.32	30.09	0.346	0.227	0.144	0.083	0.063	0.039
Mar	29.54	29.78	0.238	0.241	0.203	0.132	0.098	0.059
Apr	27.16	27.11	0.035	0.050	0.050	0.027	0.015	0.005
May	23.16	23.69	0.959	0.530	0.239	0.064	0.027	0.007
June	20.11	20.29	0.117	0.182	0.190	0.121	0.084	0.046
July	20.11	19.91	0.296	0.196	0.131	0.072	0.049	0.027
Aug	22.93	22.31	0.971	0.618	0.351	0.148	0.092	0.047
Sep	24.04	23.45	0.817	0.589	0.397	0.218	0.152	0.085
Oct	26.58	26.73	0.174	0.150	0.136	0.101	0.077	0.047
Nov	27.10	26.75	0.335	0.344	0.295	0.180	0.127	0.073
Dec	28.09	27.63	0.668	0.467	0.264	0.099	0.057	0.027
Yearly	25.726	25.565	0.221	0.172	0.113	0.067	0.054	0.043

Table 6.2: Average Indoor Temperature Comparison; Manually Calculated vs Circuit Computed (°C); Solar

Discussion

With and without solar input, as the infiltration rate increases, the discrepancy (Δ) between the monthly average indoor temperature estimates made by the two models decreases. In general, the discrepancy is low and there is very good correspondence between the monthly average indoor temperatures determined by the two models. With solar input included, all monthly averages are within 1° of each other. With 0.33 ach infiltration, this error margin decreases to less than 2/3 of a degree.

Because the circuit based averages are based on a single continuous year-length simulation, computed monthly averages are affected by the previous month's temperatures. This effect does not take place with the manual calculations which are made independently for each month. For example, in the second and third columns of Table 6.1, the March circuit average is 21.52°C, significantly above the April manual average of 18.66°C. This contributes to the higher April circuit average of 18.93°C. This effect can be seen, to a less consistent degree, for the comparison of the averages with solar input (Table 6.2).

6.3 Monthly Heating Loads

In Chapter 5, monthly heating and cooling load estimates were made using versions of the Reference circuit model of the low energy house. In this section heating load estimates are made using the Verification circuit and Manual model with and without solar input for June with a setpoint temperature of 20°C. Verification of a cooling load computation is not presented since the same circuit computation technique is employed for both cooling and heating load computations.

Verification Without Solar Input

Recall that the steady-state version of the heat balance Eqn. 3, with the assumption that $C_T dT_{in} = 0$, results in Eqn. 6 shown here again:

$$G_{incident} \cdot A_w \cdot SHGC + \dot{Q}_{heating} = \dot{Q}_{cooling} + \frac{(T_{in\_avg} - T_{out\_avg})}{R_T} \qquad (6)$$

With no solar input and no artificial cooling this becomes:

$$\dot{Q}_{heating} = \frac{(T_{in\_avg} - T_{out\_avg})}{R_T} = \frac{(T_{in\_avg} - T_{out\_avg})}{0.00514408} \qquad (12)$$

where the R_T is the total resistance between the indoors and outdoors for 0.33 ach infiltration (calculated in Appendix E). For June, we have $T_{out\_avg} = 13.37°C$, based on Sydney IWEC data and $T_{in\_avg} = 20°C$ giving:

$$0.00514408 \cdot \dot{Q}_{heating} = 20 - 13.37$$

$$\dot{Q}_{heating} = 1289.1\,W$$

$$Q_{heating} = 1289.1 \times 30 \times 24 = 928.15\,kWh$$

With the solar gain circuit component disabled, the Verification circuit computed the June heating load to be 921.56 kwh using the same circuit computation strategy illustrated in Fig. 5.6. The discrepancy between the manual calculation and the Verification circuit computation as a percentage of the latter is 0.7%.

Verification With Solar Input

With solar input and no artificial cooling, Eqn. 6 becomes:

$$\dot{Q}_{heating} = \frac{(T_{in\_avg} - T_{out\_avg})}{0.00514408} - G_{incident} \cdot A_w \cdot SHGC \qquad (13)$$

The solar gain term "$G_{incident} \cdot A_w \cdot SHGC$" is implemented in the circuit models as a current source component *(SolarGain2Floor*, Fig. 6.1*)* producing the hourly varying solar gain (W)

sequence described as $\dot{Q}_{solar,gain}(t)$ in section 4.3.6 and Appendix C. The average value of this hourly sequence between June 1 and June 30 is 1309.77 W. This average value was calculated using a spreadsheet but could have been determined by performing an average computation on the output of the current source component during the Micro-Cap simulation.

From the June simulation output of the Verification circuit with heating active, the average indoor temperature is 21.02°C. Also, for June, $T_{out\_avg} = 13.37\ °C$. The above equation becomes:

$$\dot{Q}_{heating} = \frac{(21.02-13.37)}{0.00514408} - 1309.77 = 177.05\,W$$

$$Q_{heating} = 177.05 \times 30 \times 24 = 128.05\,kWh$$

With the solar components active, the Verification circuit computed the June heating load to be 113.12 kwh. The discrepancy between the manual calculation and the Verification circuit computation as a percentage of the latter is 13.2%.

Discussion

Table 6.3 below summarizes the heating load computations using the (Heavy) Verification circuit as well as the manual June heating load calculations of the Heavy house with an infiltration rate of 0.33 ach.

	Verification Circuit	Manual Calculation	Discrepancy
No Solar	921.56	928.15	0.7%
Solar	113.12	128.05	13.2%

Table 6.3: June Heating Load Comparisons; Manually Calculated vs Verification Circuit Computed (kWh)

Comparing Verification Circuit Model computations and Manual Model calculations suggests that the circuit computation strategy is sound. The discrepancy between these two techniques illustrates that thermal mass helps to reduce the heating load proportional to the degree of indoor temperature variation (the Manual model calculation assumes *no* indoor temperature variation).

This discrepancy also indicates the inaccuracy of the Manual model proportional to indoor temperature variation. In the case of the heating load calculation with *no* solar input included, the Manual model calculation is accurate, with a very low discrepancy compared to the Verification circuit computation. This is due to the fact that the steady-state assumption $(C_T dT_{in} = 0)$ is maintained throughout the simulation $(T_{in}(t) \approx T_{in\_avg} \approx T_{setpoint})$, see Fig. 5.6 for the same result using the Reference circuit). This assumption is the basis of the Manual model.

In contrast, when solar input *is* included in the calculation and circuit simulation:

$$T_{in}(t) \neq T_{in\_avg}, \quad T_{in}(t) \text{ varies about } T_{in\_avg} = 21.02°C, \text{ and} \qquad (14)$$
(illustrated in Fig. 5.7a for the Reference circuit with $T_{in\_avg} = 20.85°C$)

$$C_T \, dT_{in} \neq 0 \qquad (15)$$

This results in an over-estimation of the manual heating load calculation and the relatively high discrepancy with the circuit based heating load computation. This illustrates that the circuit based computation manages transient heat transfer and temperature inputs significantly more accurately than the manual calculation.

6.4 Building Time Constant (τ)

The computation of the Building Time Constant using circuit models was presented for the Light, Medium and Heavy Reference versions of the low energy house in Ch. 5. The same physical modifications to the Heavy Reference house producing the Light and Medium versions listed in Table 5.2 are applied to the Heavy Verification circuit of Fig. 6.1 producing Light and Medium Verification circuits. After disabling the one circuit component modelling solar gain (*SolarGain2Floor* in Fig. 6.1*)*, $\tau_{circuit}$ is computed using these 3 Verification circuits configured at varying infiltration rates using the procedure described in section 5.5.1. Using the Manual model, τ_{manual} is calculated using Eqn. 7 for the same three houses at the same infiltration rates. Examples of calculations of τ_{manual} for the Light and Heavy models at various infiltration rates are shown in Appendix E. Table 6.4 below contains a comparison of τ_{manual} and $\tau_{circuit}$ determined at various infiltration rates for the Light, Medium and Heavy Verification circuits. Δ is taken as a percentage of $\tau_{circuit}$ computation, assumed to be the more accurate of the two τ values.

| | HEAVY Verification | | | MEDIUM Verification | | | LIGHT Verification | | |
ACH	Manual	Circuit	$\lvert\Delta\rvert$ (%)	Manual	Circuit	$\lvert\Delta\rvert$ (%)	Manual	Circuit	$\lvert\Delta\rvert$ (%)
0	145.0	139.5	3.9	17.5	16.3	7.0	2.31	1.44	59.8
0.33	98.5	97.9	0.6	15.0	14.3	5.0	2.18	1.37	59.1
0.5	84.6	85.3	0.9	13.9	13.4	4.0	2.12	1.34	58.8
1	59.7	62.7	4.8	11.6	11.4	1.4	1.97	1.24	57.9
2	37.6	42.1	10.7	8.6	8.9	2.8	1.71	1.09	56.9
3	27.4	32.2	14.8	6.9	7.3	5.9	1.52	0.97	56.6
5	17.8	22.2	19.7	4.9	5.5	10.0	1.24	0.79	57.4
10	9.5	11.8	19.4	2.9	3.2	11.2	0.85	0.52	63.2
15	6.5	6.3	2.2	2.0	2.0	0.5	0.64	0.38	70.3

Table 6.4: Comparing Manually Calculated and Circuit Computed τ (hr), For Varying Infiltration Rates

Observations

As described in section 6.1.1, the manual calculation of τ is based on the *lumped* thermal capacitance [53] of the house (Eqn. 1) which can result in overestimations of τ exceeding 100% [47]. For the Verification circuit models, the maximum discrepancy is 70% for the Light circuit with 15 ach infiltration. The discrepancy for the Heavy and Medium circuits is significantly less: the manual τ values correspond to the circuit computed τ values more significantly. A possible explanation for the varying degree of discrepancy is that the thermal capacitance of these houses are less distributed than the Light version with the majority of the capacitance located in the concrete floor as shown below in Table 6.5.

Circuit	Floor	Ceiling, Walls	Air
Heavy	90.4%	8.6%	1.0%
Medium	78.9%	18.2%	2.9%
Light	43.1%	49.4%	7.5%

Table 6.5: Thermal Capacitance Distribution as a % of Total; Heavy, Medium and Light Models

As presented in section 2.2, Antonopoulos claims that the distribution of thermal capacitance is significant when determining the building time constant due to the resulting divergence of apparent (C_T) versus effective thermal capacitance (C_{eff}) of a building.

The calculation of τ_{manual} (Eqn. 7) is directly based on the lumped apparent thermal capacitance defined here as C_T. It is doubtful that $\tau_{circuit}$ is based on C_{eff} as defined by Antonopoulos. For single story Greek houses, Antonopoulos found the range of the ratio C_T/C_{eff} to be 2.2-3.1 for well-insulated buildings and increasing toward 4.5 for uninsulated houses [53]. If $\tau_{circuit}$ were based on C_{eff}, it would be expected that the ratios of $\tau_{manual}/\tau_{circuit}$ derived from the values in Table 6.4 would approximate these ratios. The ratios do increase moving from Heavy and Medium to Light buildings but to a maximum ratio of $\tau_{manual}/\tau_{circuit} = 1.7$ for the Light (poorly insulated) building at 15 ach.

For the Heavy and Medium Verification Models, the ratio $\tau_{manual}/\tau_{circuit}$ varies within the range of 0.79 to 1.04 and within 0.88 to 1.07 respectively for infiltration rates between 0 and 15 ach. For the Light Verification Model the range is (1.57, 1.70). The manual calculation of τ generally confirms the circuit computation of τ but less so for the Light house. The divergence of these two methods of determining τ varies with infiltration rate and thermal mass distribution.

6.4.1 Indoor Air Response to a Cold Snap

In section 5.5.2 a sudden 10˚ drop in outdoor temperature was applied to the Light, Medium and Heavy low energy house models with solar input disabled and with all circuit nodes, including the indoor temperature initialized to 21˚C ($T_0 = 21˚C$). In this section, the response to the same configuration of the Heavy Verification circuit (Fig. 6.1) is compared to the decay equation of the Manual model for the Heavy model (Eqn. 8) over the same time period. For the 10˚ drop the decay equation becomes:

$$T_{in}(t) = 11 + 10e^{-\frac{t}{\tau}} \quad \text{where } t = 1 \text{ is 1 am of day 1} \tag{16}$$

Where $\tau = \tau_{manual} = R_T C_T$ is the manually calculated building time constant based on the *lumped* thermal capacitance of the house (C_T) and various infiltration rates.

In Figure 6.2, indoor temperature responses to a 10° drop in outdoor temperature as computed by the Heavy Verification circuit model and manually calculated using the decay Eqn. 16, are shown for various infiltration rates.
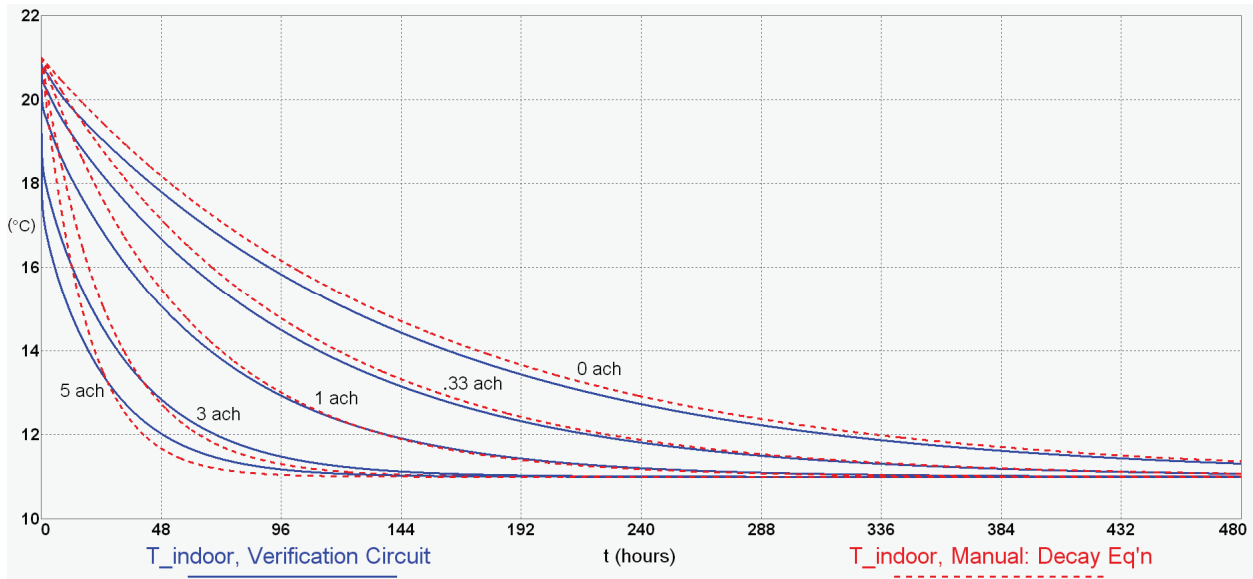
Figure 6.2: Heavy Verification Circuit Response to 10° Drop and Corresponding Decay Equation; $T_{indoor}(0)\ 21°C$

Observations

The response comparisons shown in Fig. 6.2 echo the τ-comparisons of the Heavy Verification circuit shown in Table 6.4. As the infiltration rate increases the discrepancy between the manual calculated τ and the circuit computed τ increases. On first inspection, these curves appear to confirm that the Heavy Verification circuit model responds thermally like a single lumped capacitance. A closer view of the decay curves illustrates the effect of infiltration and other non-capacitive heat flow paths that distort the indoor temperature response away from a simple RC-based (single-τ) decay equation (Eqn. 16) response. Figure 6.3 is a magnified view of the first four days of the decay curves for the Heavy Verification circuit with 0.33 ach and 5 ach infiltration. Also shown are the decay equations (Eqn. 16) using $\tau_{circuit}$ and τ_{manual} for 0.33 ach and 5 ach infiltration.
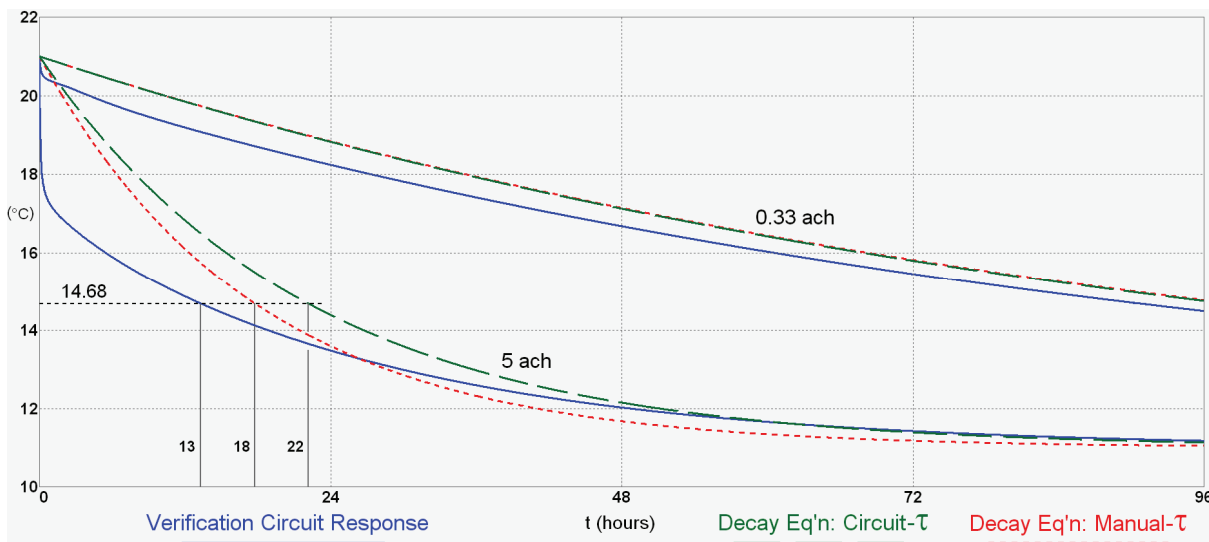

Figure 6.3: Circuit Response and Decay Eqn Predictions; First 4 Days of 10° Drop; Heavy Verification

For 0.33 ach, both decay equation curves using $\tau_{circuit}$ and τ_{manual} equally differ from the actual circuit response. At 5 ach, for approximately the first 40 h, the decay curve using τ_{manual} is significantly different but closer to the circuit response than the decay curve using $\tau_{circuit}$. After 40 h ($\approx 2\tau_{circuit}$), the decay curve using $\tau_{circuit}$ corresponds well with the circuit response. In general, both decay curves are *not* good approximations to the initial circuit response for 5 ach. These decay curves become good approximations to the circuit response after approximately 20 h. *(τ_{manual})* and 40 h. *($\tau_{circuit}$)*: approximately $1\tau_{circuit}$ and $2\tau_{circuit}$ respectively.

The circuit response includes an immediate indoor temperature drop of approximately 0.5° for 0.33 ach and 3° for 5 ach due to the fast heat transfer between the cooler outdoor air and the indoor air through the thermal paths that contain no capacitance: windows, window frames and infiltration. This drop increases as the infiltration rate increases because the infiltration heat transfer is due to the direct mixing of an increasing volume of cooler outdoor air with warmer indoor air. At 10 ach, the drop is 5°. The heat transfer between the thermal mass and the indoor air which mediates the cooling due to infiltration occurs at a slower rate but eventually becomes significant and pulls the indoor response curve towards the decay equation.

The circuit response is made up of two time constants: τ_1, the fast decay in air temperature due to direct mixing with cool outdoor air and τ_2, the slower decay in mass temperature that eventually counteracts and therefore tempers the fast decay. The simple decay equation based on one time constant (either $\tau_{circuit}$ or τ_{manual}) does not model these dynamics.

Figure 6.3 also contains the prediction of when the temperature reaches: *$11 + 10/e = 14.68°C$*, for 5 ach infiltration. Solving for *t* using the single time constant decay Eqn. 16:

$$11 + \frac{1}{e} \cdot 10 = 11 + 10e^{-\frac{t}{\tau}} \rightarrow 10\,e^{-1} = 10e^{-\frac{t}{\tau}} \rightarrow t = \tau.$$

If the building response were governed by one time constant, then it would take τ hours for the indoor temperature to reach 14.68°C (within *$\tau_{manual} = 18$* and *$\tau_{circuit} = 22$* hours). The indoor air temperature reaches 14.68°C after 13 hours which is outside of this range.

6.4.2 Discussion

• Micro-Cap enables the simple computation of the Building Time Constant from a building circuit model *($\tau_{circuit}$)*. Across various infiltration rates and building weights, $\tau_{circuit}$ was found to be both larger and smaller than $\tau_{manual} = R_T\,C_T$ to varying degrees, where τ_{manual} is the commonly used manual calculation of the building time constant [47] [51] [48] based on the *apparent* lumped Thermal Capacitance *(C_T)* of a building. Across varying infiltration rates, the discrepancy between $\tau_{circuit}$ and τ_{manual} was found to be less than 20% for a Heavy building and less than 12% for a Medium building; 12 out of 18 τ-comparisons of Heavy and Medium buildings varied within 7%. There was no apparent ordering of $\tau_{circuit}$ and τ_{manual}. For

the Light building, at all infiltration rates considered, the discrepancy between $\tau_{circuit}$ and τ_{manual} was found to be consistently between 56% and 70% and $\tau_{circuit} < \tau_{manual}$. Although the Light building discrepancies as a percentage are significantly higher, the absolute difference in τ values varies between 0.4 and 0.9 h.

From this data (Table 6.4), it is concluded that both $\tau_{circuit}$ and τ_{manual} are equally valid approximations of the building time constant and the Manual model confirms the circuit approximation of τ.

• The building response to a step drop of 10° was (i) computed by the Verification circuit and (ii) calculated by the decay equation (Eqn. 8) of the Manual model. The two responses show good correspondence, with some discrepancies, for various infiltration rates as shown in Fig. 6.2 above. These results provide evidence that the circuit model response is a sound estimate of the building response.

Looking closer at these two estimates of the building response, it can be seen that the circuit response is modelling more thermal dynamics than the single time constant decay equation of Eqn. 8 and this is the cause of the discrepancy between the Verification circuit and Manual models. The discrepancy is highest at the start of the response period due to the impact of τ_1, the *fast* time constant associated with the mixing of outdoor and indoor air from infiltration. The discrepancy decreases with time as τ_2, the time constant associated with the heat transfer between thermal mass and indoor air, gradually dominates the circuit response. The Verification circuit models *both* τ_1 and τ_2 while in the case of the Manual model, the decay equation models *only* τ_2 when either $\tau_{circuit}$ or τ_{manual} is used in the decay equation (illustrated in Fig. 6.3). Again, for both corresponding decay equations, the Manual model does *not* model the fast time constant τ_1, which dominates the early circuit response.

6.5 Chapter Summary

A Manual model of the low energy house was derived from physical principles and presented in equation form. This lumped steady-state model includes simplifications to the original transient IDA and circuit models of Chs. 4 and 5. The Reference circuit model of Ch. 5 was modified to incorporate most of these simplifications to form a Verification circuit model (Fig. 6.1). The simulation results of the Verification model were compared to the corresponding calculations of the Manual model with the aim of supplementing the circuit model validation of Ch. 4 (e.g: verification of heating load computations is included). Compared to the validation of Ch. 4, the validation of this chapter is more transparent.

Average monthly temperatures and heating loads predicted by the Manual and Verification circuit models compared favourably. All predicted monthly average temperatures were within 1° of each other with the discrepancy decreasing as the infiltration rate increased. The discrepancies for a monthly heating load prediction were 13.2% and 0.7%, with and without solar input. The significantly larger former discrepancy is attributed to the

innaccuracy of the Manual model due to its steady-state assumptions. When solar radiation is included, the resulting modelled indoor temperature is dynamic and often above the setpoint.

The building time constant (τ) was computed for Light, Medium and Heavy versions of the Verification circuit using the procedure presented in section 5.5.1. These computations $(\tau_{circuit})$ were compared to the corresponding calculation using the Manual model: $\tau_{manual} = R_T\,C_T$. It was found that $\tau_{circuit} \approx \tau_{manual}$, with no consistent ordering. For houses with varying infiltration rates, thermal capacitance and envelope resistance, both $\tau_{circuit} < \tau_{manual}$ and $\tau_{circuit} > \tau_{manual}$ were found except for the very light building where consistently, $\tau_{circuit} < \tau_{manual}$ (Table 6.4). From this data, it is concluded that both $\tau_{circuit}$ and τ_{manual} are equally *valid approximations* of the building time constant (τ).

The predicted responses of the Heavy house models (Manual and Verification circuit) to a sudden drop of 10° compared favourably across infiltration rates, with some discrepancy; pairs of curves are easily discernable (Fig. 6.2). The discrepancy between the two model responses is attributed to the Verification model modelling *both τ_1 (fast τ due to mixing of outdoor and indoor air from infiltration)* and τ_2 (associated with the heat transfer between thermal mass and indoor air) while the Manual model (Eqn. 8) models *only τ_2. τ_1* dominates the Verification circuit response immediately after the step drop, coinciding with the time when the discrepancy between the two responses is highest and the discrepancy increases with the infiltration rate. This comparison between the Verification and Manual model responses highlights the accuracy of the circuit response.

Compared to the circuit response, τ is a single approximate measure of building thermal inertia becoming more inaccurate as infiltration increases. In addition, a circuit model can incorporate solar insolation whereas τ provides little indication of how a building responds to solar insolation.

The verification of circuit model computations presented in this chapter provides addition evidence that the circuit modelling methodology is sound. The discrepenacies (due to manual model deficiencies) of the comparisons presented in this chapter, highlight strengths of this methodology.

7 Conclusion

A single zone low energy house was modelled using both a commercial building simulation program (IDA ICE) and electric circuits utilising Micro-Cap, a commercial circuit solving program. Simulation output in the form of year-length spans of hourly indoor temperature sequences were compared with the two sequences showing excellent agreement for the case of no solar radiation and no infiltration/ventilation. For the cases involving solar radiation and/or infiltration, the two resulting temperature sequences did not agree to the same degree. The source of this disagreement could not be determined since the physical assumptions and computation details forming the basis of the IDA modelling of infiltration and solar radiation were not fully known.

A simple Manual model for performing thermal calculations was presented in detail for the low energy house. This model included simplifications to the physical parameters such as static outer surface resistances and the lumping of all thermal mass into one capacitance node. The model assumed steady-state conditions and was used as a reliable computation reference to compare circuit simulation output due to its grounding in basic thermal principles such as energy balance. The circuit model of the low energy house was simplified to match the assumptions of the Manual model and the two models were used to perform various thermal computations. The two models agreed well with discrepancies attributed to the steady-state assumptions and poor transient heat transfer modelling capabilities of the Manual model.

Based on these two sets of simulation output comparisons, it is concluded there is good evidence that building thermal modelling using electric circuits is sound and accurate. There are opportunities of future work in this regard. The IEA publishes a suite of "simulation test cases for evaluating, diagnosing and correcting building energy simulation software" called *BESTEST* [91]. One would assume that all construction properties and climate data required to implement a circuit model would be specified for the tests to be implementable in a range of building simulation programs. It would be prudent to perform this verification in stages, with each test designed to exercise one thermal dynamic process such as heat conduction through a wall. The aim would be to build up the testing scenario to a complete multi-zone building and generate test results confirming the expected accuracy of this methodology.

At the time of writing, the U.S. Department of Energy listed "406 building software tools for evaluating energy efficiency, renewable energy and sustainability in buildings" [92]. The obvious question that follows is why present yet another building simulation program to add to this large collection. One characteristic that distinguishes this methodology is that throughout the modelling process, the user is in close proximity to the Building Physics. Firstly, there is no need for the user to deal with differential equations or other mathematics besides the equations that govern heat transfer at surfaces and other equations defining energy sources: solar radiation, artificial heating/cooling, etc. Secondly, the main user interface is the thermal circuit, a standard thermal modelling diagram and useful for

96

illustrating heat flow paths and thermal relationships. Thirdly, while building a thermal circuit model, the user is manipulating thermal resistance, thermal capacitance, temperature and heat transfer components of a thermal circuit as opposed to entering building construction parameter values into screen dialog boxes. Fourthly, the Electrical Analogy governs the modelling process: the user must map quantities between the thermal and electrical domain at the start and end of the modelling process.

This methodology makes no assumptions or decisions for the user in terms of thermal modelling. The user has complete control over the accuracy and detail of the thermal model and must decide how each building and environmental component is modelled. Simple thermal models can be implemented and simulation results generated quickly. In terms of simulation engine accuracy, the simulation time step size is the one programatic parameter the user may need to modify. The methodology is direct, transparent and ammenable to understanding Building Physics.

References

1. Lovins, A., *Stanford Energy Lectures, , in Advanced Energy Efficiency: Concepts and Practice*. 2007, Rockey Mountain Institute.

2. King, D., *Engineering a low carbon built environment, The discipline of Building Engineering Physics*. 2010, The Royal Academy of Engineering: London, England. p. 1-50.

3. The Centre for International Economics. *The buidings sector and greenhouse: key facts*. 2007 [cited 2012 Mar 28]; Available from: http://www.yourbuilding.org/library/carbonfootprint.pdf.

4. Australian Academy of Science, *Australia's renewable energy future*, M. Dopita and R. Williamson, Editors. 2010, Australian Academy of Science.

5. EES, *Energy use in the Australian residential sector 1986-2020 [electronic resource] /* 2008, Canberra, A.C.T. : Department of the Environment, Water, Heritage and the Arts, Commonwealth of Australia.

6. Australian Government - Department of Climate Change and Energy Efficiency. *Commerical buildings in Australia*. 2012, Dec 13, 2011 [cited 2012 March 28]; Available from: http://www.climatechange.gov.au/what-you-need-to-know/buildings/commercial.

7. EECS Dept - University of California. *The SPICE Page*. [cited 2012 Mar 29]; SPICE3:[Electric Circuit Simulator Program]. Available from: http://bwrc.eecs.berkeley.edu/classes/icbook/spice/.

8. Spectrum Software, *Micro-Cap, Version 10*. 2010, Spectrum: Sunnyvale, Ca, USA. p. SPICE circuit simulator.

9. Davies, M.G., *Building Heat Transfer*. 2004, Chichester, England: John Wiley & Sons, Ltd.

10. Urbikain, M.K. and M.G. Davies, *Determination of wall decay times by use of a polynomial equation*. International Journal of Heat and Mass Transfer, 2010. **53**(19-20): p. 3692-3701.

11. Shavit, G., *Short-time step analysis and simulation of homes and buildings during the last 100 years*. ASHRAE Transactions, 1995. **101(1)**(242): p. 856-867.

12. Paschkis, V., *Periodic Heat Flow in Building Walls Determined by Electrical Analogy Method*. ASHVE Transactions, 1942. **48**.

13. Cengel, Y.A., *Heat and mass transfer: a practical approach*. 3rd ed. 2007, New York, NY: McGraw-Hill.

14. Fraisse, G., et al., *Development of a simplified and accurate building model based on electrical analogy*. Energy and Buildings, 2002. **34**(10): p. 1017-1031.

15. Peng, C. and Z. Wu, *Thermoelectricity analogy method for computing the periodic heat transfer in external building envelopes*. Applied Energy, 2008. **85**(8): p. 735-754.

16. Nottage, H.B., Parmelee, G.V., *Circuit analysis applied to load estimating (part 1)*. ASHVE Trans., 1954(60): p. 59-102.

17. Nottage, H.B. and G.V. Parmelee, *Circuit analysis applied to load estimating (part 2)*. ASHVE Trans., 1955(61): p. 125-150.

18. Nielsen, T.R., *Simple tool to evaluate energy demand and indoor environment in the early stages of building design*. Solar Energy, 2005. **78**(1): p. 73-83.

19. Crabb, J.A., N. Murdoch, and J.M. Penman, *A simplified thermal response model*. Building Services Engineers. Research and Technology, 1987. **8**(1): p. 13-19.

20. Clarke, J.A., *Energy Simulation in Building Design*. 2nd ed. 2002, Glasgow: Butterworth-Heinemann.

21. Gouda, M.M., S. Danaher, and C.P. Underwood, *Building thermal model reduction using nonlinear constrained optimization*. Building and Environment, 2002. **37**(12): p. 1255-1265.

22. Beccali, G., et al., *Is the transfer function method reliable in a European building context? A theoretical analysis and a case study in the south of Italy*. Applied Thermal Engineering, 2005. **25**(2-3): p. 341-357.

23. Stephenson, D.G. and G.P. Mitalas, *Calculation of heat conduction transfer functions for multi-layer slabs*. ASHRAE Transactions, 1971. **77**(2): p. 117-126.

24. Urbikain, M.K. and M.G. Davies, *One-dimensional solutions to Fourier's equation and measures of heat transmission through walls: The role of wall decay times*. Building and Environment, 2008. **43**(9): p. 1433-1445.

25. Iu, I. and D.E. Fisher. *Application of conduction transfer functions and periodic response factors in cooling load calculation procedures*. 2004. Nashville, TX.

26. Hittle, D.C. and R. Bishop, *An improved root-finding procedure for use in calculating transient heat flow through multilayered slabs*. International Journal of Heat and Mass Transfer, 1983. **26**(11): p. 1685-1693.

27. Achterbosch, G.G.J., et al., *The development of a convenient thermal dynamic building model*. Energy and Buildings, 1985. **8**(3): p. 183-196.

28. Davies, M.G., *Solutions to Fourier's equation and unsteady heat flow through structures*. Building and Environment, 1995. **30**(3): p. 309-321.

29. Eunilkim, D.H., *Wall-response factors to estimate the conduction heat gains with time-varying thermal coefficients.* Energy, 1991. **16**(6): p. 933-939.

30. Ouyang, K. and F. Haghighat, *A procedure for calculating thermal response factors of multi-layer walls--State space method.* Building and Environment, 1991. **26**(2): p. 173-177.

31. Mitalas, G.P. and D.G. Stephenson, *Room thermal response factors.* Journal Name: ASHRAE Trans.; (United States); Journal Volume: 73, 1967. **73**(2): p. 1-10.

32. Wang, S. and Y. Chen, *A novel and simple building load calculation model for building and system dynamic simulation.* Applied Thermal Engineering, 2001. **21**(6): p. 683-702.

33. Spitler, J.D. and D.E. Fisher, *On the relationship between the radiant time series and transfer function methods for design cooling load calculations.* HVAC and R Research, 1999. **5**(2): p. 123-136.

34. Duska, M., et al. *Analytical approach to transient heat conduction in cooling load calculations.* in *17th Int. Air-conditioning and Ventilation Conference.* 2006. Prague: Society of Environmental Engineering.

35. Chen, Y. and S. Wang, *A new procedure for calculating periodic response factors based on frequency domain regression method.* International Journal of Thermal Sciences, 2005. **44**(4): p. 382-392.

36. Athienitis, A.K., M. Stylianou, and J. Shou, *A Methodology for Building Thermal Dynamics Studies and Control Applications.* ASHRAE Transactions, 1990. **96**(Part 2): p. 839-848.

37. Athienitis, A.K., H.F. Sullivan, and K.G.T. Hollands, *Discrete fourier series models for building auxiliary energy loads based on network formulation techniques.* Solar Energy, 1987. **39**(3): p. 203-210.

38. Tindale, A., *Third Order Lumped-Parameter Simulation Method.* Building Services Engineering Research and Technology, 1993. **14**(3): p. 87-97.

39. Hudson, G., Underwood, C.P., *A Simple Building Modelling Procedure For Matlab/Simulink.* Proceedings Of Building Simulation '99, 1999. **2**: p. 777-783.

40. Lombard, C. and E.H. Mathews, *Efficient, steady state solution of a time variable RC network, for building thermal analysis.* Building and Environment, 1992. **27**(3): p. 279-287.

41. Mathews, E.H. and P.G. Richards, *A tool for predicting hourly air temperatures and sensibles energy loads in buildings at sketch design stage.* Energy and Buildings, 1989. **14**(1): p. 61-80.

42. Lorenz, F., Masy, G., *Methode d'evaluation de l'economie d'energie apporttee par l'intermittence de chauffage dans les batiments. Traitment par differences finies d'un model a deux constates de temps.* , in *Facuite de Sciences Appliquees.* 1982, Universite de Liege: Liege, Belgium.

43. Dewson, T., B. Day, and A.D. Irving, *Least squares parameter estimation of a reduced order thermal model of an experimental building.* Building and Environment, 1993. **28**(2): p. 127-137.

44. Penman, J.M., *Second order system identification in the thermal response of a working school.* Building and Environment, 1990. **25**(2): p. 105-110.

45. Underwood, C.P., *Personal Communication: Solution Method of 21R20C network.* 2013: Sydney, Australia.

46. Francois, C., J.C. Visier, and E. Hutter. *Simplified Building Dynamic Models: Choice, Formalisms and Parmeters Catalogues.* in *System Simulation in Buildings: Proceedings of the 3rd International Conference.* 1990.

47. Antonopoulos, K.A. and C. Tzivanidis, *Time constant of Greek buildings.* Energy, 1995. **20**(8): p. 785-802.

48. Catalina, T., J. Virgone, and E. Blanco, *Development and validation of regression models to predict monthly heating demand for residential buildings.* Energy and Buildings, 2008. **40**(10): p. 1825-1832.

49. Corrado, V., H.E. Mechri, and E. Fabrizio, *Building energy performance assessment through simplified models: Application of the ISO 13790 quasi-steady state method.* Building Simulation 2007, Vols 1-3, Proceedings, ed. Y. Jiang, et al. 2007, Beijing: Tsinghua University Press. 79-86.

50. Yohanis, Y.G. and B. Norton, *Useful solar heat gains in multi-zone non-domestic buildings as a function of orientation and thermal time constant.* Renewable Energy, 2002. **27**(1): p. 87-95.

51. ISO, *Energy performance of buildings - Calculation of energy use for space heating and cooling.* . 2008, ISO: Switzerland. p. 1-162.

52. Fernández, J.L., M.A. Porta-Gándara, and N. Chargoy, *Rapid on-site evaluation of thermal comfort through heat capacity in buildings.* Energy and Buildings, 2005. **37**(12): p. 1205-1211.

53. Antonopoulos, K.A. and E. Koronaki, *Apparent and effective thermal capacitance of buildings.* Energy, 1998. **23**(3): p. 183-192.

54. Antonopoulos, K.A. and E.P. Koronaki, *Effect of indoor mass on the time constant and thermal delay of buildings.* International Journal of Energy Research, 2000. **24**(5): p. 391-402.

55. US Dept of Energy. *IWEC Weather Data, NSW Sydney 947670.* EnergyPlus Energy Simulation Software 2009, [cited 2009 August 1]; All   Regions:Southwest   Pacific   WMO   Region   5:   Australia:[Available   from:

http://apps1.eere.energy.gov/buildings/energyplus/cfm/weather_data3.cfm/region=5_southwest_pacific_wmo_region_5/country=AUS/cname=Australia.

56. Luther, M.B., *MABEL Air Leakage & Infiltration Testing Demonstration Project*, M.A.B.E. Laboratory, Editor. 2007, Deakin University: Geelong, Victoria. p. 27.

57. Luther, M.B., *Ventilation Research on Australian Residential Construction.* Architectural Science Review, 2009. **52**(2): p. 89-98.

58. Resource Planning and Development Commission. *Air Infiltration Rates of New Housing.* State of the Environment Tasmania 2003, Dec 14, 2006 [cited 2011 June 24]; Available from: http://soer.justice.tas.gov.au/2003/index.php.

59. Kusuda, T. and P.R. Achenbach, *Earth temperature and thermal diffusivity at selected stations in the United States*. 1965, NATIONAL BUREAU OF STANDARDS: GAITHERSBURG MD. p. 233.

60. Heidarinejad, G., V. Khalajzadeh, and S. Delfani, *Performance analysis of a ground-assisted direct evaporative cooling air conditioner.* Building and Environment, 2010. **45**(11): p. 2421-2429.

61. Kalogirou, S.A. and G.A. Florides, *Measurements of Ground Temperature at Various Depths*, in *3rd International Conference on Sustainable Energy Technologies*. 2004: Nottingham, UK.

62. Solar Energy Laboratory, *TRNSYS 16, Mathematical Reference Manual*. 2007-03: University of Wisconsin-Madison.

63. Duffie, J.A. and W.A. Beckman, *Solar engineering of thermal processes*. 2nd ed. 1991, New York John Wiley & Sons, Inc. xvii, 762.

64. Equa Simulation AB, *IDA Indoor Climate and Energy, Version 4*. 2009, Equa Simulation AB: Stockholm, Sweden.

65. Retscreen International, *Clean Energy Project Analysis: RETScreen Engineering & Cases Textbook*, in *Chapter: Solar Water Heating Project Analysis*. 2001-2004, Natural Resources Canada.

66. Bring, A., P. Sahlin, and M. Vuolle, *Models for Building Indoor Climate and Energy Simulation*, in *Task 22: Building Energy Analysis Tools*, I.E. Agency, Editor. 1999, Royal Institute of Technology: Stockholm, Sweden.

67. Zhi-lei, L., G. Gang, and T. Jin-chun1 (2003) *Temperature field simulation of building envelope*. ABAQUS.

68. Al-Sanea, S.A., *Thermal performance of building roof elements.* Building and Environment, 2002. **37**(7): p. 665-675.

69. Pandey, D.K., R.B. Lee, and J. Paden, *Effects of atmospheric emissivity on clear sky temperatures.* Atmospheric Environment, 1995. **29**(16): p. 2201-2204.

70. Bliss, R.W., *Atmospheric radiation near the surface of the ground: A summary for engineers.* Solar Energy, 1961. **5**(3): p. 103-120.

71. Clark, G. and C.P. Allen. *The Estimation of Atmospheric Radiation for Clear and Cloudy Skies*. in *2nd National Passive Solar Conference*. 1978. Philadelphia.

72. Berdahl, P. and R. Fromberg, *The thermal radiance of clear skies.* Solar Energy, 1982. **29**(4): p. 299-314.

73. Berger, X., D. Buriot, and F. Garnier, *About the equivalent radiative temperature for clear skies.* Solar Energy, 1984. **32**(6): p. 725-733.

74. Martin, M. and P. Berdahl, *Characteristics of infrared sky radiation in the United States.* Solar Energy, 1984. **33**(3-4): p. 321-336.

75. Perez, R., et al., *Modeling daylight availability and irradiance components from direct and global irradiance.* Solar Energy, 1990. **44**(5): p. 271-289.

76. Illinois, U.o. and LBNL, *EnergyPlus Engineering Reference: The Reference to EnergyPlus Calculations*. 2010. p. 1105.

77. Karlsson, J. and A. Roos, *Modelling the angular behaviour of the total solar energy transmittance of windows.* Solar Energy, 2000. **69**(4): p. 321-329.

78. Lyons, P., B. Hockings, and C. Reardon, *Your Home Technical Manual, Passive Design*, C. Change, Editor. 2010, Australian Government.

79. Bassett, C.R. and M.D.W. Pritchard, *Heating,*. Environmental Physics Series (Harlow, Essex). 1968, London: Longmans.

80. Van Straaten, J.F., *Thermal Performance of Buildings,*. Elsevier Architectural Science Series, ed. H.J. Cowan. 1967, London: Elsevier.

81. Laret, L. *Use of general models with a small number of parameters: Part 1. theoretical analysis*. in *CLIMA 2000: 7th International Congress of Heating and Air Conditioning*. 1980. Budapest.

82. Hambley, A.R., *Electrical Engineering, Principles and Applications*. 4 ed. 2008: Pearson, Prentice Hall.

83. Bambrook, S.M., A.B. Sproul, and D. Jacob, *Design optimisation for a low energy home in Sydney.* Energy and Buildings, 2011. **43**(7): p. 1702-1711.

84. Bambrook, S., *Personal Communication: Fortran Source Code Files of IDA-ICE Implementation of Low Energy House Model*. 2010: Sydney, Australia.

85. Bambrook, S., *Personal Communication: IDA Summary of Low Energy House Model as Implemented in IDA-ICE*. 2010: Sydney, Australia.

86. DesignBuilder Software Limited, *DesignBuilder, Version 2.1.0.025*. 2009: Stroud, Gloucestershire, UK.

87. Clarke, D.W., *PID algorithms and their computer implementation.* Transactions of the Institute of Measurement and Control, 1984. **6**(6): p. 305-316.

88. FEMP, *M&V Guidelines: Measurement & Verification for Federal Energy Projects, Version 3.0*, U.S.D.O. Energy, Editor. 2008, U.S. Department Of Energy: Washington, DC.

89. Henze, G.P., et al., *Sensitivity Analysis of Optimal Building Thermal Mass Control.* Journal of Solar Energy Engineering, 2007. **129**(4): p. 473-485.

90. Szokolay, S.V., *Introduction to Architectural Science : The Basis of Sustainable Design*. 2nd ed. 2008, Amsterdam; Boston; London: Elsevier/Architectural Press.

91. IEA. *Task 34 - Testing and Validation of Building Energy Simulation Tools (BESTEST)*. Solar Heating & Cooling Programme 2009, June 2009 [cited 2012 March 29]; Available from: http://www.iea-shc.org/publications/category.aspx?CategoryID=39.

92. U.S. Dept of Energy - Energy Efficiency and Renewable Energy. *Building Energy Software Tools Directory*. 2011, Jan 26, 2011 [cited 2012 Mar 29]; Available from: http://apps1.eere.energy.gov/buildings/tools_directory/.

93. Walsh, P.J. and A.E. Delsante, *Calculation of the thermal behaviour of multi-zone buildings.* Energy and Buildings, 1983. **5**(4): p. 231-242.

94. ISO, *Thermal performance of building components - Dynamic thermal characteristics - Calculation methods.* 2007, ISO: Switzerland. p. 1-22.

95. Chen, T. and Z. Yu, *A statistical method for selection of sequences of coincident weather parameters for design cooling load calculations.* Energy Conversion and Management, 2009. **50**(3): p. 813-821.

96. ASHRAE, *ASHRAE Handbook - Fundimentals (SI)*. 2005, Atlanta, GA: American Society of Heating, Refrigerating and Air-Conditioning Engineers, Inc.

Appendix A   Error of an nth Order RC ladder Model of a Wall Layer

The error in representing a wall layer as an n-length RC ladder (n^{th} order representation) decreases as n increases. The error analysis that follows is based on comparing the transmission matrices of the RC ladder circuit and the wall layer (as a homogenous slab) as presented by Davies [9]. A function $err(\ )$ is defined and an example of the reduction in $err(\ )$, as n increases, for a Concrete Floor layer representation is given.

A transmission matrix describes the relationship between the temperatures on either side of a layer and the heat flows on either side of a layer. If T_i, T_e are the internal and external temperatures on either side of a layer and q_i and q_e are the heat flows at the internal and external boundaries of the layer, then the relationship amongst these values can be expressed in matrix form as:

$$\begin{bmatrix} T_i \\ q_i \end{bmatrix} = \begin{bmatrix} f_{11} & f_{12} \\ f_{21} & f_{22} \end{bmatrix} \begin{bmatrix} T_e \\ q_e \end{bmatrix} \tag{1}$$

Davies provides formulas for calculating the 4 complex values of the transmission matrix F^n for an nth order RC representation of a layer shown below.
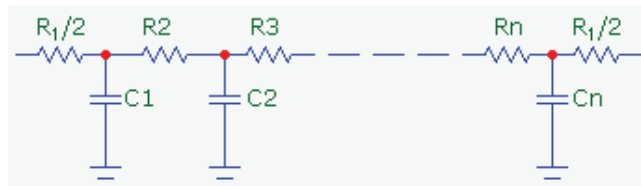
These 4 complex values are calculated from:
- n, the number of resistors and capacitors,
- R_t, the total resistance of the layer,
- C_t, the total capacitance of the layer and
- P, the period of temperature and heat flow fluctuations being considered and are given by Eqn. 2 below.

$$F^n = \begin{bmatrix} f_{111} + jf_{112} & f_{121} + jf_{122} \\ f_{211} + jf_{212} & f_{221} + jf_{222} \end{bmatrix} = \begin{bmatrix} 1 + j2\pi R_t C_t / 2Pn^2 & (R_t/n)[1 + j2\pi R_t C_t / 4Pn^2] \\ j2\pi C_t / Pn & 1 + j2\pi R_t C_t / 2Pn^2 \end{bmatrix}^n \tag{2}$$

Davies shows that each f_{ijk} approaches a value e_{ijk} as $n \to \infty$, where e_{ijk} are elements of E, the transmission matrix of an equivalent homogenous slab given by Equation 3. This formulation of matrix E (Eqn. 3) is common in building thermal research [20, 24, 26, 93] and is presented in European Standard 13786 [94]:

$$E = \begin{bmatrix} e_{111} + je_{112} & e_{121} + je_{122} \\ e_{211} + je_{212} & e_{221} + je_{222} \end{bmatrix}$$

$$= \begin{bmatrix} \cosh\{(\pi R_t C_t / P)^{1/2}(1+j)\} & \sinh\{(\pi R_t C_t / P)^{1/2}(1+j)\}/[(\pi C_t / PR_t)^{1/2}(1+j)] \\ \sinh\{(\pi R_t C_t / P)^{1/2}(1+j)\} \times [(\pi C_t / PR_t)^{1/2}(1+j)] & \cosh\{(\pi R_t C_t / P)^{1/2}(1+j)\} \end{bmatrix} \tag{3}$$

As the length (n) of an RC ladder modelling a wall layer increases, the closer the resulting transmission matrix (F^n) approaches the limiting *analytic* transmission matrix (E) for a given layer resistance (R_t), capacitance (C_t) and period (P). A procedure for choosing an appropriate n based on the resulting matrix F^n (Eqn. 2) is given as follows.

The four elements of F^n and E are complex values. To evaluate the error of using one complex value z_a as an estimate for another z_b, the percentage error of z_a is defined:

$err(z_a, z_b) = |z_b - z_a| / |z_b| \times 100$

where $|z|$ is the modulus (absolute value) of complex value z.

This error measure is extended to the error of using matrix F^n as an estimate of matrix E by taking the maxium $err()$ value of the four matrix elements of F^n. The fourth component of F^n is not considered since $e_{11} = e_{22}$ and $f_{11} = f_{22}$ (see Eqns. 2 and 3).

$$err(F^n) = \max\{\ err(F_{11}^n, E_{11}),\ err(F_{12}^n, E_{12}),\ err(F_{21}^n, E_{21})\ \} \qquad (4)$$

The matrix elements of E and F^n depend on P, the period of the temperature (T) and heat flow (Q) fluctuations used in the model. In general as P decreases (i.e. T and Q frequency increases), a higher n is required to achieve the same err value. For modelling climatic inputs such as ambient temperature and solar-based heat transfer, a *maximum* period of $24\,h$ should be used with $P = 12\,h$ preferable. If internal heat sources such as scheduled artificial heating or internal loads fluctuating with higher frequencies than $1/24\,h$, then a lower P value should be used in the $err(F^n)$ calculation.

$err(F^n)$ was implemented on a standard spread sheet application and used to choose n for wall, roof and floor representations of the low energy house models. Example progressions of matrix values and corresponding err values for an increasing n, are shown for the Floor Concrete Layer ($R_t = 0.0004385\ °C/W$, $C_t = 16968\ J/°C$) for 2 periods: $P = 12\,h$ and $P = 2\,h$ in Tables A.1 below. For $err < 1\%$ and these two periods, 9th and 27th order RC ladder representations are required, respectively.

P = 12 h	Matrix E		
e_{11}	e_{12}	e_{21}	e_{22}
0.373 + j1.866	0.000383 + j0.000280	-5665 + j7766	0.373 + j1.866

P = 12 h				Matrix F^n			
n	f^n_{11}	$err(f^n_{11})$	f^n_{12}	$err(f^n_{12})$	f^n_{21}	$err(f^n_{21})$	$err(F^n)$
1	1 + j1.948	33.2%	0.000439 + j0.000427	33.2%	j8885	60.1%	60.1%
2	0.526 + j1.948	9.1%	0.000387 + j0.000320	8.6%	-4326.9 + j8884	18.1%	18.1%
4	0.409 + j1.890	2.3%	0.000383 + j0.000290	2.1%	-5376.5 + j8094	4.55%	4.55%
6	0.389 + j1.877	1.0%	0.000383 + j0.000284	0.9%	-5541.4 + j7915	2.02%	2.02%
8	0.382 + j1.872	0.56%	0.000383 + j0.000282	0.53%	-5596.4 + j7851	1.13%	1.13%
9	0.380 + j1.871	0.44%	0.000383 + j0.000282	0.42%	-5611.0 + j7833	0.89%	0.89%
12	0.377 + j1.869	0.25%	0.000383 + j0.000281	0.23%	-5634.9 + j7804	0.50%	0.50%
15	0.376 + j1.868	0.16%	0.000383 + j0.000280	0.15%	-5645.8 + j7790	0.32%	0.32%

P = 2 h	Matrix E		
e_{11}	e_{12}	e_{21}	e_{22}
-14.70 - j4.175	-0.001209 + j0.000672	-81739 - j146967	-14.700 - j4.175

P = 2 h				Matrix F^n			
n	f^n_{11}	$err(f^n_{11})$	f^n_{12}	$err(f^n_{12})$	f^n_{21}	$err(f^n_{21})$	$err(F^n)$
1	1 + j11.69	146%	0.000439 + j0.00256	181%	j53306.1	128%	181%
2	-16.08 + j11.69	104%	-0.00144 + j0.00192	91.8%	-155768 + j53306	127%	127%
6	-16.38 - j2.953	13.6%	-0.00131 + j0.000761	9.80%	-115369 - j140690	20.3%	20.3%
10	-15.32 - j3.792	4.77%	-0.00125 + j0.000702	3.42%	-93806 - j146028	7.20%	7.20%
15	-14.98 - j4.013	2.10%	-0.00123 + j0.000685	1.51%	-87072 - j146729	3.17%	3.17%
20	-14.86 - j4.085	1.18%	-0.00122 + j0.000679	0.84%	-84732 - j146868	1.78%	1.78%
27	-14.79 - j4.126	0.65%	-0.00121 + j0.000676	0.46%	-83379 - j146924	0.98%	0.98%

Tables A.1: Progression of *F* Matrix Elements and *err( )* Values as *n* Increases; Concrete Floor Layer, *P = 12, 2* h

Appendix B   Derivation of Orientation-Specific Solar Irradiance Sequences
Methodology Basis: [18]

The raw data from Sydney IWEC file consists of *hourly* Solar Insolation values:

$E(t)$:   Direct Normal Radiation in Wh/m^2
$E_{d\text{-}h}(t)$: Diffuse Horizontal Radiation in Wh/m^2

These values are hourly, resulting in equal hourly Irradiance values:

G :	Direct Normal Irradiance in W/m^2	$G(t) = E(t) / 1\ h$	(5)
$G_{d\text{-}h}$:	Diffuse Horizontal Radiation in W/m^2	$G_{d\text{-}h}(t) = E_{d\text{-}h}(t) / 1\ h$	(6)

For each orientation x, *incident* irradiance is made up of: direct, ground-reflected and diffuse:

1. $\quad G_{direct,x} = \quad G \cdot cos(\theta)$ $\qquad\qquad$ θ :   Angle of Incidence $\qquad$ (7)

2. $\quad G_{gnd\text{-}ref,x} = \quad \alpha_g \cdot (G \cdot cos(Z) + G_{d\text{-}h}) \cdot F_g$ $\quad$ α_g: Ground Albedo (0.2) $\quad$ (8)
    $\qquad\qquad\qquad\qquad\qquad\qquad\qquad\qquad\qquad$ Z: Zenith Angle
    $\qquad\qquad\qquad\qquad\qquad\qquad\qquad\qquad\qquad$ F_g: Ground View Factor

    $\quad F_g = \qquad (1 - cos\,\beta)/2$ $\qquad\qquad\qquad$ β: Surface Tilt $\qquad\qquad$ (9)
    $\qquad\qquad\qquad\qquad\qquad\qquad\qquad\qquad\qquad$ Walls: $F_g = 0.5$, Roof: $F_g = 0$

3. $\quad G_{diffuse,x} = \quad G_{d\text{-}h} \cdot F_2 \cdot sin\,\beta\ +$ $\qquad$ sky horizon   [75, 76] $\qquad$ (10)
    $\qquad\qquad\qquad G_{d\text{-}h} \cdot F_1 \cdot (1 - cos\,\beta)/2\ +$ $\quad$ sky dome
    $\qquad\qquad\qquad G_{d\text{-}h} \cdot F_1 \cdot a/b$ $\qquad\qquad\qquad$ circumsolar region
    $\qquad\qquad\qquad\qquad\qquad\qquad\qquad\qquad\qquad$ F_1, F_2, a, b defined by Perez [75]

These 3 components are calculated for each orientation x (*N: north, E: east, S: south, W: west, H: horizontal*) and at each hour, giving a total hourly incident irradiance stream at each orientation:

$$G_{incident,x}(t) = G_{direct,x}(t) + G_{gnd\text{-}ref,x}(t) + G_{diffuse,x}(t), \quad x \in \{N, E, S, W, H\} \qquad (11)$$

Appendix C   Orientation-Specific Solar Heat Gain Flux Sequences (Glazing)

For the glazing of the low energy house, $SHGC = 0.6$ and this is taken as the maximum value when the angle of incidence (θ) is 0: $SHGC_0 = 0.6$ [78].

For diffuse and ground-reflected components of incident irradiance, the SHGC is slightly less than $SHGC_0$:

$$SHGC_{diff} = SHGC_{gnd\text{-}ref} = SHGC_0 - 0.063 \quad [95, 96]. \tag{12}$$

For direct incident radiation transmitted through glazing, a correction is applied to the static Solar Heat Gain Coefficient ($SHGC_0$: $\theta = 0$). Developed by Karlsson [77], this correction is a polynomial function fitted to empirical data for various window types. The 3 parameters of this function, $karl(\theta, p, q)$, are: the angle of incidence (θ), the number of panes (p) and type of glazing/coatings (q).

$$karl(\theta, p, q) = (1 - a \cdot z^{\alpha} - b \cdot z^2 - c \cdot z^{\gamma}) \tag{13}$$

$$a = 8, \quad b = 0.25/q, \qquad c = 1 - a - b, \ z = \theta/90$$
$$\alpha = 5.2 + 0.7q, \qquad \gamma = 5.26 + 0.06p + q(0.73 + 0.04p)$$

Karlsson [77] defines the category parameter, q for various window coatings. The low energy house has double-pane low-e windows with the coating assumed to be Tin Oxide:
$$p = 2, q = 3.5.$$

The SHGC for direct incident irradiance is θ-dependent and hence time and orientation dependent:

$$SHGC_{direct,x}(t) = SHGC_0 \cdot karl(\theta(t), 2, 4) \tag{14}$$

At each orientation x, the Solar Heat Gain flux (W/m^2) of the window is:

$$\dot{q}_{solar,gain\_orient}(t) = \begin{array}{lll} SHGC_{direct,x}(t) & \cdot G_{direct,x}(t) \ + & \text{direct} \\ SHGC_{gnd\text{-}ref} & \cdot G_{gnd\text{-}ref,x}(t) \ + & \text{ground-reflected} \\ SHGC_{diff} & \cdot G_{diffuse,x}(t) & \text{diffuse} \end{array} \tag{15}$$

where $G_{direct,x}(t)$, $G_{gnd\text{-}ref,x}(t)$ and $G_{diffuse,x}(t)$ are defined above in Appendix B and $x \in \{N, E, S, W, H\}$.

Appendix D   Low Energy House: Construction Element Properties
Source: [85]

Element: Layer	Area	x Thickness	k Conductivity	ρ Density	c_p Specific Heat	R-value	R_t Resistance	C_t Capacitance
	m²	m	W/m.°C	kg/m³	J/kg.°C	m².°C/W	°C/W	kJ/°C
Floor: Concrete	201.2	0.15	1.7	2300	880	0.08824	0.0004385	61084
Floor: Rigid Insulation	201.2	0.26	0.04	32	750	6.50000	0.0323062	1255
Floor: Soil [b]	201.2	0.5	2	2000	1000	0.25000	0.0012425	201200
Floor: Gnd Insulation [b]	201.2	0.1	1.7	1	1	0.05882	0.0002924	0.020
Floor: Timber (Plywood) [c]	201.2	0.02	0.12	545	1210	0.16500	0.0008201	2654
Floor: R$_{SI}$	201.2					0.11000	0.0005467	
Ceiling: Steel (2)	201.2	0.0016	60	7800	460	0.00003	0.0000001	1155
Ceiling: Insulation	201.2	0.25	0.04	32	750	6.25000	0.0310636	1207
Ceiling: R$_{SI}$	201.2					0.10000	0.0004970	
Ceiling: R$_{SO}$ [a]	201.2					0.04000	0.0001988	
North Wall: Steel (2)	41	0.0016	60	7800	460	0.00003	0.0000007	235.4
North Wall: Insulation	41	0.25	0.04	32	750	6.25000	0.1524390	246.0
North Wall: R$_{SI}$	41					0.13000	0.0031707	
North Wall: R$_{SO}$ [a]	41					0.04000	0.0009756	
North Wall: Window Pane	13.5					0.62500	0.0462963	
North Wall: Window Frame	1.5					0.50000	0.3333333	
South Wall: Steel (2)	49	0.0016	60	7800	460	0.00003	0.0000005	281.3
South Wall: Insulation	49	0.25	0.04	32	750	6.25000	0.1275510	294.0
South Wall: R$_{SI}$	49					0.13000	0.0026531	
South Wall: R$_{SO}$ [a]	49					0.04000	0.0008163	
South Wall: Window Pane	6.3					0.62500	0.0992063	
South Wall: Window Frame	0.7					0.50000	0.7142857	
East,West Wall: Steel (2)	24.17	0.0016	60	7800	460	0.00003	0.0000011	138.8
East,West Wall: Insulation	24.17	0.25	0.04	32	750	6.25000	0.2585850	145.0
East,West Wall: R$_{SI}$	24.17					0.13000	0.0053786	
East West Wall: R$_{SO}$ [a]	24.17					0.04000	0.0016549	
E,W Wall: Window Pane	3.6					0.62500	0.1736111	
E,W Wall: Window Frame	0.4					0.50000	1.2500000	
Total Timber Walls, Ceiling [c]	339.5	0.02	0.12	545	1210	0.16500	0.0004860	4478
Inside Air	563.4	m³		1.1986	1006			679.3

[a] Verification circuit models   [b] IDA circuit model   [c] Lightweight model [13]

Envelope Surface Properties [84]

Element: Layer	α Absorptivity	ε Emissivity
Ceiling/Roof and Walls:		
Structurally Insulated Panels	0.4	0.9
Window Frames	0.5	0.9
Window Glazing	---	0.9

Appendix E   Low Energy House: Lumped Model Component Derivations

			Scaling : 3600	Scaled	Order	Component Values		Order Required For
Layer	**Area**	**R-Value**	R_t	C_t	n	R_{comp}	C_{comp}	$err < 1\%$, $P=12$
Floor	m²	m².°C/W	°C/W	kJ/°C	J/°C	n	Ω	F	n
Concrete	201.2	0.08824	0.0004385	61084	16968	15	0.0000292	1131.2	9
Insulation	201.2	6.50000	0.0323062	1255	348.8	15	0.0021537	23.25	11
Soil[b]	201.2	0.25000	0.0012425	201200	55889	26	0.0000478	2149.6	36
Ground[b]	201.2	0.05882	0.0002924	0.020	0.01	--			
Plywood Floor[c]	201.2	0.16500	0.0008201	2654	737.1	6	0.0001367	122.9	3
R_{SI}	201.2	0.11000	0.0005467				0.0005467		
Lumped Ceiling, Walls									
Steel	339.54	0.000027	0.00000008	1949	541.5				
Insulation	339.54	6.25	0.01840726	2037	565.9				
Steel	339.54	0.000027	0.00000008	1949	541.5				
Total w/o Surfaces	339.54	6.250053	0.01840741	5936	1648.8	21	0.00087654	78.51	21
R_{SI}	339.54	0.13	0.00038287				0.00038287		
R_{SO}[a]	339.54	0.04	0.00011781						
Timber Ceiling, Walls									
Total w/o Surfaces[c]	339.54	0.16500	0.00048595	4478	1243.9	6	0.00008099	207.3	3
Lumped Windows									
Glazing	27	0.455	0.01685185						
Glazing R_{SI}	27	0.13	0.00481481						
Glazing R_{SO}[a]	27	0.04	0.00148148						
Frames	3	0.33	0.11						
Frames R_{SI}	3	0.13	0.04333333						
Frames R_{SO}[a]	3	0.04	0.01333333						
Internal Air	563.4	m³		679.3	188.7	1		188.7	

[a] Verification circuit models only   [b] IDA circuit model only   [c] Light Building circuit model only

Low Energy House: Manual Building Time Constant Calculations

Element Totals	**Mass** (kg)	**Mass**[b] (kg)	$R\ (\Omega)^{d}$	$C\ (F)^{a}$		$R\ (\Omega)^{bd}$	$C\ (F)^{bc}$	
Floor (*Insulated*)	71088.0	3867.1	0.0332914	17316.6		0.03367296	1085.9	
Window Glazing	----	----	0.0231482	0.0		0.02314815	0.0	
Window Frames	----	----	0.1666667	0.0		0.16666667	0.0	
Ceiling and Walls	11191.2	3701.0	0.0189081	1648.8		0.00098663	1243.9	
Inside Air	675.3	675.3	----	188.7		----	188.7	
		ach						
Infiltration Resistance		0.33	0.01605830			0.016058296		
		1	0.00529924			0.005299238		
		3	0.00176641			0.001766413		
		5	0.00105985			0.001059848		
			Heavy	**Heavy**	**Heavy**	**Light**	**Light**	**Light**
Building Totals		**ach**	R_T	C_T	τ (hr)	R_T	C_T	τ (hr)
Mass (kg)	82954.5	0	0.0075686	19154.1	144.97	0.0009154	2518.5	2.31
Specific Mass (kg/m²)	412.3	0.33	0.0051441	19154.1	98.53	0.0008660	2518.5	2.18
Light Version		1	0.0031169	19154.1	59.70	0.0007806	2518.5	1.97
Mass (kg)	8243.3	3	0.0014322	19154.1	27.43	0.0006029	2518.5	1.52
Specific Mass (kg/m²)	41.0	5	0.0009297	19154.1	17.81	0.0004912	2518.5	1.24

[a] Scaled, Heavy (Reference) Version   [b] Light Version, [c] Scaled   [d] Includes Surface Resistances

Appendix F   Lumped - Unlumped Circuit Equivalence Proof

1. Parallel Factoring

Common factors of 2 parallel impedances may be factored *before* performing the parallel calculation.

Let Z_1, Z_2 be 2 impedances in parallel with common factor f:

$Z_1 = f{\cdot}r_a + jf{\cdot}s_a$ and $Z_2 = f{\cdot}r_b + jf{\cdot}s_b$ with

$Z_a = r_a + js_a$ and $Z_b = r_b + js_b$ then: $Z_1 // Z_2 = f{\cdot}(Z_a // Z_b)$

Proof.

$Z_1 = f{\cdot}r_a + jf{\cdot}s_a = f{\cdot}(r_a + js_a) = f{\cdot}Z_a$ and

$Z_2 = f{\cdot}r_b + jf{\cdot}s_b = f{\cdot}(r_b + js_b) = f{\cdot}Z_b$

$$Z_1 \| Z_2 = \frac{Z_1 Z_2}{Z_1 + Z_2} = \frac{f \cdot Z_a f \cdot Z_b}{f \cdot Z_a + f \cdot Z_b} = \frac{f^2 \cdot Z_a Z_b}{f \cdot (Z_a + Z_b)} = f \cdot \left(\frac{Z_a Z_b}{Z_a + Z_b} \right) = f \cdot (Z_a \| Z_b)$$

2. Ladder Factoring

The impedance of an RC ladder comprised of R and C component values with common factor f is equal to f times the impedance of the RC ladder comprised of these R and C components with the factor f removed.

Given the following 2 RC ladder circuits with branch impedances and corresponding total impedances shown for any particular angular frequency ω_i:
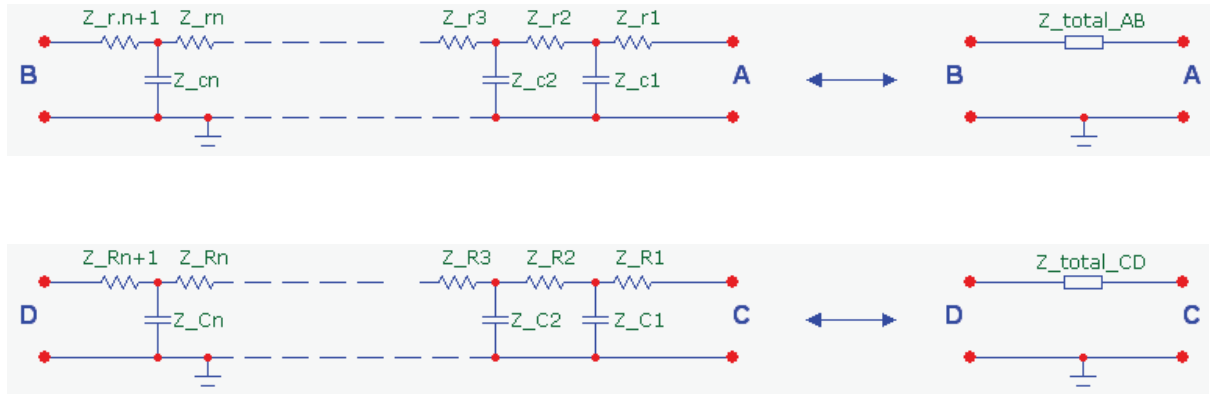
if $\quad Z_{Ri} = f{\cdot}Z_{ri}$ *and* $Z_{Ci} = f{\cdot}Z_{ci}, \;\; i = 1.. \, n{+}1,$ $\hspace{4cm}$ *(16)*

then $\quad Z_{total\_CD} = f{\cdot}Z_{total\_AB}$

Proof by induction on the length of the ladder n.
The impedances are evaluated from left to right.

$n = 1\!: Z_{total\_CD} = Z_{R2} + (\, Z_{C1} \,||\, Z_{R1}\,) = f{\cdot}Z_{r2} + (\,f{\cdot}Z_{c1} \,||\, f{\cdot}Z_{r1}\,) = f{\cdot}Z_{r2} + f{\cdot}(\, Z_{c1} \,||\, Z_{r1}\,) = f{\cdot}Z_{total\_AB}$

Assume Eqn. 16 is true the n-length ladder.

It is shown Eqn. 16 follows for the $n{+}1$-length ladder. Assume ladders A'B' and C'D' are constructed from the above 2 ladders by adding a resistor and capacitor to each ladder (shown below), with the impedances: Z_{r_n+2}, Z_{c_n+1} to ladder AB and Z_{R_n+2}, Z_{C_n+1} to ladder CD and $Z_{R\_n+2} = f{\cdot}Z_{r\_n+2}$ and $Z_{C\_n+1} = f{\cdot}Z_{c\_n+1}$.

$$
\begin{aligned}
Z_{total\_C'D'} &= Z_{R\_n+2} + (\, Z_{C\_n+1} \,||\, Z_{total\_CD}\,) = f{\cdot}Z_{r\_n+2} + (\,f{\cdot}Z_{c\_n+1} \,||\, f{\cdot}Z_{total\_AB}\,)\\
&= f{\cdot}Z_{r\_n+2} + f{\cdot}(\, Z_{c\_n+1} \,||\, Z_{total\_AB}\,) = f{\cdot}Z_{total\_A'B'}
\end{aligned}
$$

Therefore Eqn. 16 holds for the $n{+}1$-length ladder and holds for ladders of *any* length.

3. Equivalence Theorem

The Thevenin equivalent circuits of the lumped and unlumped n-order RC representations of the walls and roof made from the same materials of a single-zone building produce equivalent indoor air temperature responses. The building is assumed to be oriented North and is exposed to an orientation-specific irradiance sequence $G_X(t)$ and outdoor temperature sequence represented as a voltage sequence $V_o(t)$.

Definitions (17)

A_X: opaque area of façade X $\qquad$ $X \in \{\,North, East, South, West, Horizontal\,\}$

$\qquad\qquad\qquad\qquad\qquad\qquad\qquad\qquad$ herein: $\{N, E, S, W, H\}$

A: total opaque surface area $\qquad$ $A = A_N + A_E + A_S + A_W + A_H$

f_X: fraction of total opaque surface area $\qquad$ $f_X = \dfrac{A_X}{A}$, $X \in \{N, E, S, W, H\}$

$\qquad\qquad\qquad\qquad\qquad\qquad\qquad\qquad$ $f_N + f_E + f_S + f_W + f_H = 1$

f_X^{-1}: reciprocal of f_X $\qquad\qquad\qquad\qquad$ $f_X^{-1} = \dfrac{1}{f_X}$

$G_X(t)$: irradiance on surface X (W/m²)

$G_L(t)$: irradiance on the lumped surface

$\qquad$ $G_L(t) = f_N\, G_N(t) + f_E\, G_E(t) + f_S\, G_S(t) + f_W\, G_W(t) + f_H\, G_H(t)$

$\dot{Q}_X(t)$: the heat transfer rate due to solar

$\qquad$ radiation at opaque surface X (W) $\qquad$ $\dot{Q}_X(t) = A_X G_X(t), \quad X \in \{N, E, S, W, H\}$

$I_X(t)$: analogous circuit current sequence $\qquad$ $I_X(t) = \dot{Q}_X(t)$

$I_L(t)$: lumped circuit current sequence $\qquad$ $I_L(t) = \dot{Q}_L(t) = A \cdot G_L(t)$

$\qquad$ $I_L(t) = A \cdot [f_N\, G_N(t) + f_E\, G_E(t) + f_S\, G_S(t) + f_W\, G_W(t) + f_H\, G_H(t)]$

$\qquad$ $I_L(t) = A_N\, G_N(t) + A_E\, G_E(t) + A_S\, G_S(t) + A_W\, G_W(t) + A_H\, G_H(t)$

$\qquad$ $I_L(t) = I_N(t) + I_E(t) + I_S(t) + I_W(t) + I_H(t)$

$V_o(t)$: voltage sequence analogous to the outdoor temperature sequence.

Without loss of generality, assume each wall and roof consists of 1 layer with the following characteristics: R: material R-value, ρ: density, L: thickness, c_p: specific heat, Rsi, Rso: inner, outer surface R-values

n: chosen order of the RC representation of each wall and ceiling used for both lumped and unlumped nets

The n-order ladder representations are built by dividing the total thermal resistance and total capacitance into n equal components. The resulting component values for lumped and unlumped ladders circuits are:

$X \in \{N, E, S, W, H\}$	**Lumped (L)**	**Unlumped**
Resistors:	$R_L = \dfrac{R}{A} \times \dfrac{1}{n}$	$R_X = \dfrac{R}{A_X} \times \dfrac{1}{n} = \dfrac{R}{f_X A} \times \dfrac{1}{n}$
		$R_X = f_X^{-1} R_L$
	$Rso = \dfrac{Rso}{A}$	$Rso_X = f_X^{-1} Rso_L$
	$Rsi +_L = \dfrac{Rsi}{A} + 0.5 R_L$	$Rsi +_X = f_X^{-1} Rsi +_L$
Capacitors:	$C_L = A \times L \times \rho \times c_\rho \times \dfrac{1}{n}$	$C_X = A_X \times L \times \rho \times c_\rho \times \dfrac{1}{n}$
		$C_X = f_X C_L$

Without loss of generality, assume the temperature signal driving the circuits has angular frequency ω. The resulting component impedance values of the circuits are shown below.

$X \in \{N, E, S, W, H\}$	**Lumped (L)**	**Unlumped**	(18)
Resistive:	$Zr_L = R_L$	$Zr_X = R_X = f_X^{-1} Zr_L$	
	$Zrso_L = Rso_L$	$Zrso_X = f_X^{-1} Zrso_L$	
	$Zrsi +_L = Rsi +_L$	$Zrsi +_X = f_X^{-1} Zrsi +_L$	
Capacitive:	$Zc_L = \dfrac{1}{j\omega C_L}$	$Zc_X = \dfrac{1}{j\omega C_X} = \dfrac{1}{j\omega f_X C_L}$	
		$= f_X^{-1} Zc_L$	

3.1 Equivalence of Thevenin Impedance

The Thevenin impedance of the lumped and unlumped circuits are shown to be equal.

The lumped circuit is shown below. The temperature and irradiance sources are shown as voltage (V_o: outside temperature) and a current sources respectively.
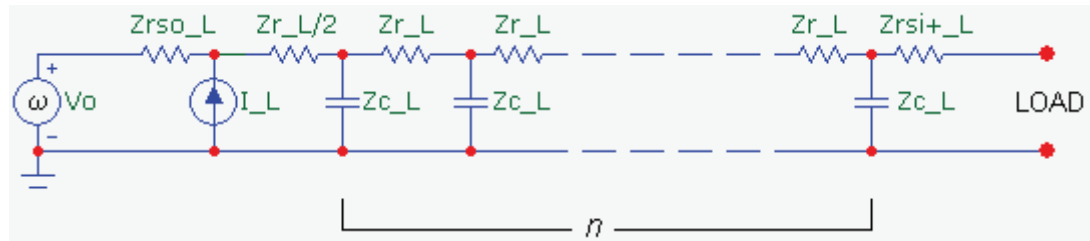
Figure 1: The Complete Lumped Circuit

3.1.1 Z_{th_L} : Thevenin impedance of the lumped circuit

To determine the Thevenin impedance, the voltage source is shorted and the current source is made open circuit. The Thevenin impedance is the impedance between the load terminals.
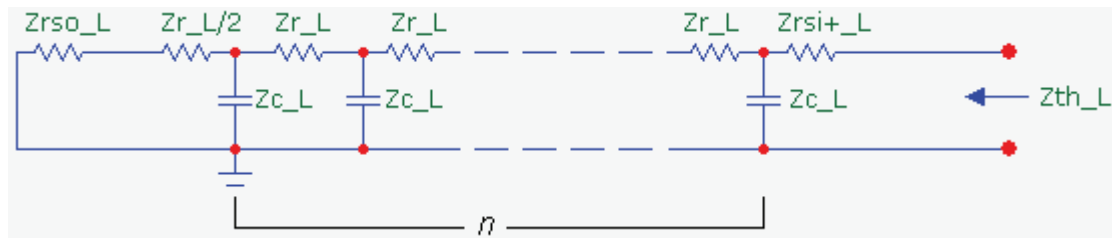
Figure 2: Thevenin Equivalent Impedance of the Lumped Circuit

With Z_{th_L} defined , the n-order RC ladder circuit above can be re-written as:
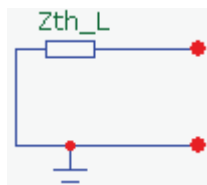
3.1.2 Z_{th_uL} : Thevenin impedance of the unlumped circuit

The complete unlumped circuit is shown below:
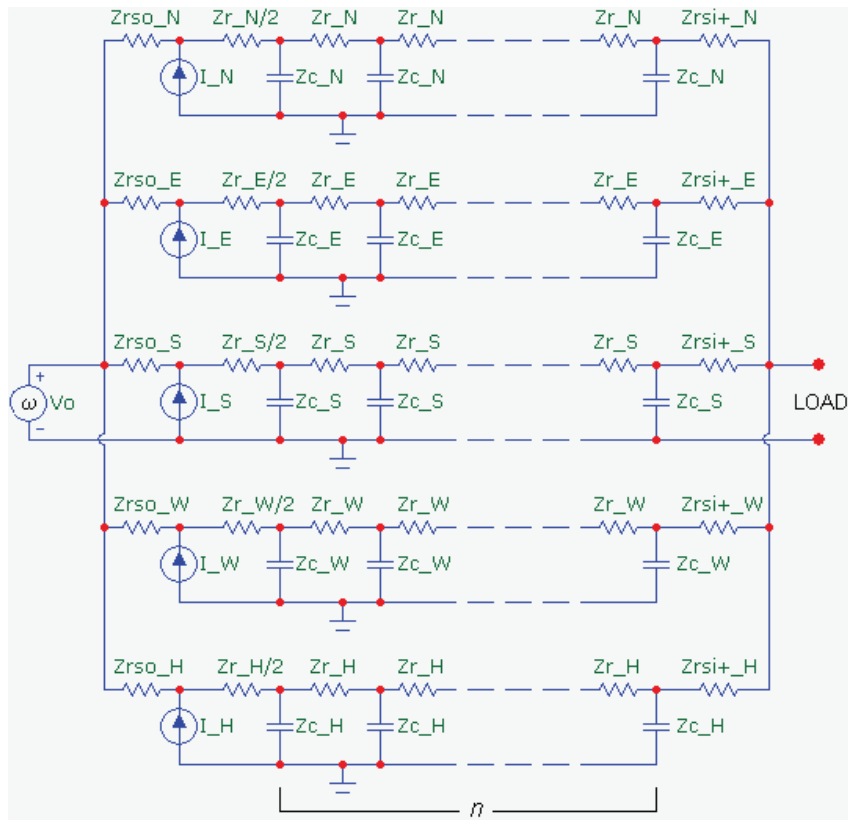
Figure 3: The Complete Unlumped Circuit

The Thevenin impedance is calculated by zeroing voltage and current sources shown below:

114
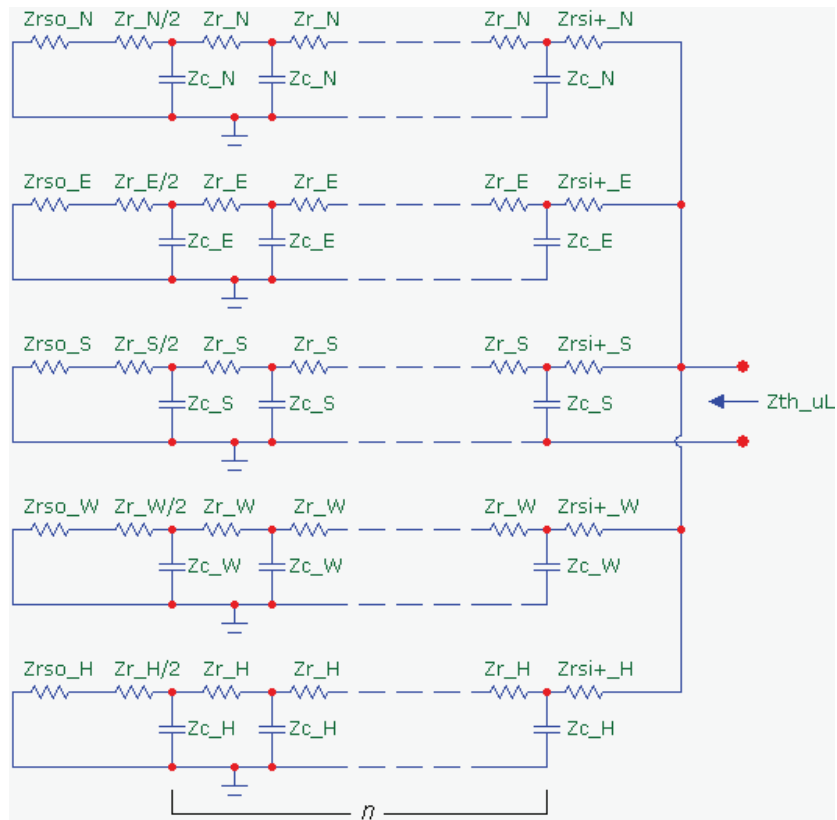
Each impedance is replaced with the equivalent multiple of the lumped impedance value from Eqns. 18:
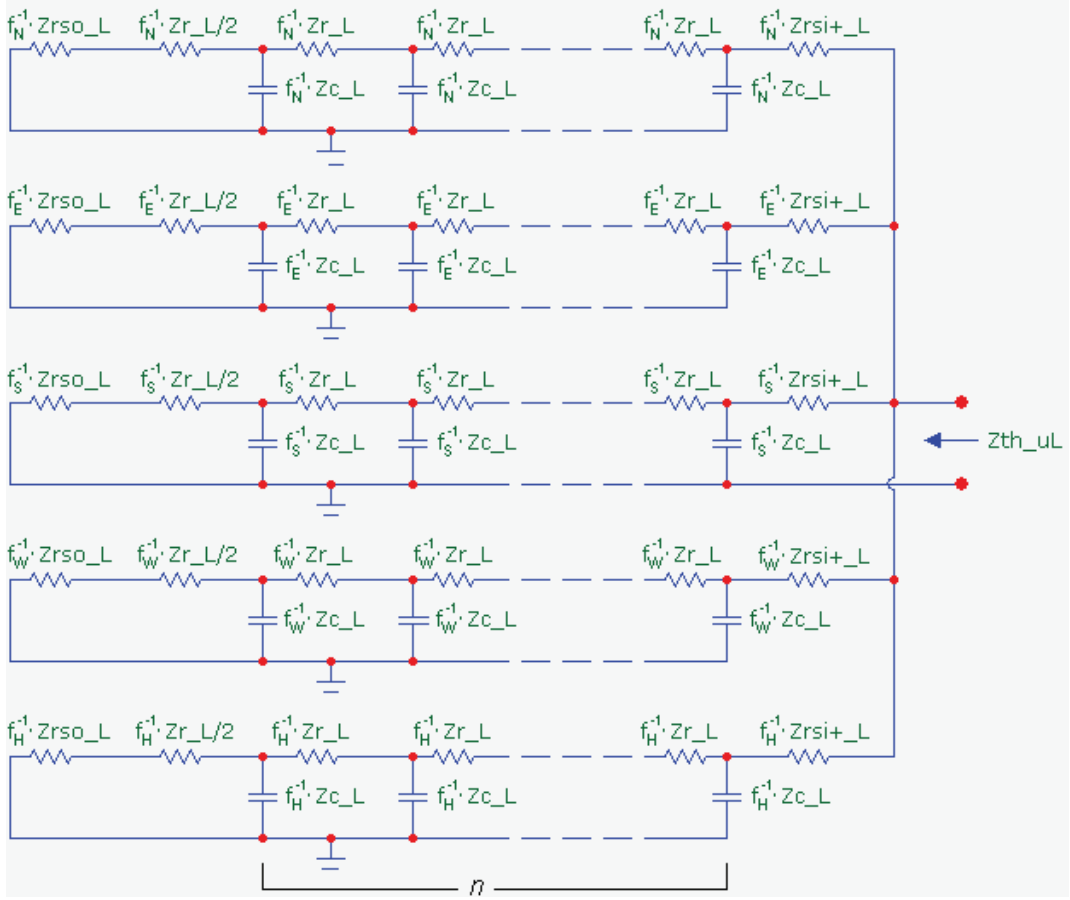
The impedance of all components of each RC ladder contain a common factor: f_X^{-1}.

By applying *Ladder Factoring*, each ladder evaluates to a multiple of the Thevenin equivalent impedance of the lumped circuit as shown below:
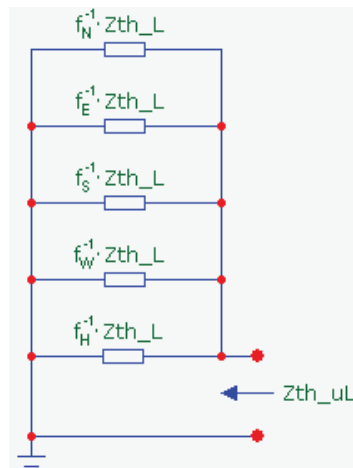
The unlumped circuit Thevenin impedance is found by performing the parallel calculation:

$$Z_{th\_uL} = \frac{1}{(f_N + f_E + f_S + f_W + f_H)\dfrac{1}{Z_{th\_L}}} = Z_{th\_L}$$

The Thevenin impedance of the lumped and unlumped circuits are equal.

115

3.2 Equivalence of Thevenin Voltage

The Thevenin voltage (V_{th}) of the lumped and unlumped circuits are shown to be equal.

The open circuit voltage at load is the voltage across the capacitor adjacent to the load terminals and is calculated by determining this voltage under 2 separate conditions: (a) V_{oc1}: V_o is active and the current sources are inactive and (b) V_{oc2}: V_o is inactive and the current sources are active. Applying the principle of superposition gives:

$$V_{th} = V_{oc1} + V_{oc2}$$

3.2.1 V_{oc1_L} : Open circuit voltage due to V_o of the *lumped* circuit

The complete original lumped circuit is shown below:
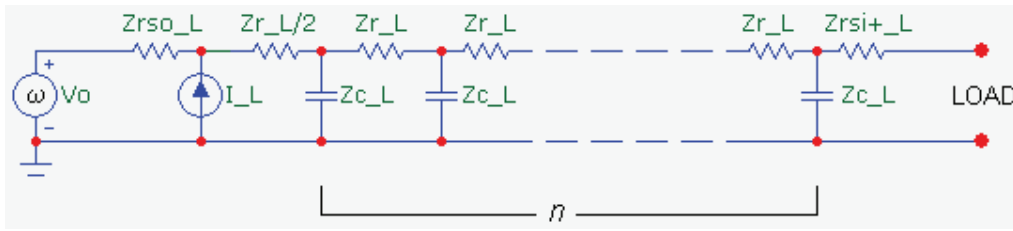
After removing the current source I_L, V_{oc1_L} is shown with the circuit nodes labelled *1..n*:
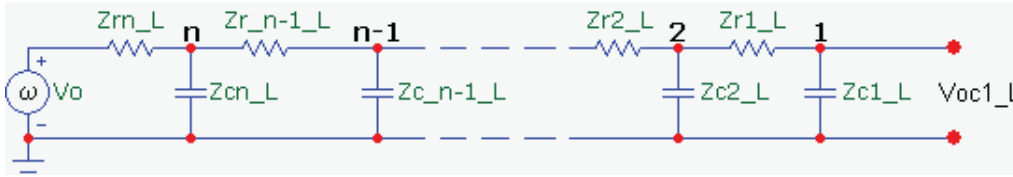
In terms of the original lumped circuit components (Fig. 1) the above component labels are:

$$Zc_{i\_L} = Zc\_L \qquad i = 1..n$$
$$Zr_{i\_L} = Zr\_L \qquad i = 1..n\text{-}1, \qquad\qquad Zr_{n\_L} = Zrso\_L + Zr\_L/2$$

An expression for V_{oc1_L} is formulated based on the following definitions:

z_{i_L}: the total impedance from a node *i* across the open circuit terminals, when only considering Zc_{i_L} and components to the right of node *i*.

Examples: $z_{1\_L} = Zc_{1\_L}$, $\qquad\qquad z_{2\_L} = Zc_{2\_L} // (Zr_{1\_L} + Zc_{1\_L})$

$$z_{1\_L} = Zc_{1\_L}$$
$$z_{i\_L} = Zc_{i\_L} // (Zr_{i\text{-}1\_L} + z_{i\text{-}1\_L}), \quad i = 2..n \tag{19}$$

V_i : the voltage at node *i*, $i=1..n+1$. $V_{n+1} = V_o$.

H_{i_L}: the voltage transfer function from node *i+1* to *i*

$$H_{i\_L} = \frac{V_i}{V_{i+1}} = \frac{z_{i\_L}}{Zr_{i\_L} + z_{i\_L}}, \quad V_i = V_{i+1} \cdot H_{i\_L} \tag{20}$$

$$V_{oc1\_L} = V_1 = V_2 \cdot H_{1\_L} = V_3 \cdot H_{2\_L} \cdot H_{1\_L} = V_{n+1} \cdot H_{n\_L} \cdot \ldots \cdot H_{2\_L} \cdot H_{1\_L} = V_o \cdot \prod_{i=1}^{n} H_{i\_L} \tag{21}$$

116

3.2.2 V_{oc1_uL} : Open circuit voltage due to V_o of the *unlumped* circuit

The original unlumped circuit (Fig. 3) is modified with the current sources I_X removed, V_{oc1_uL} shown, circuit components re-labelled and the circuit nodes on the ladder corresponding to the East facade labelled *1..n*.
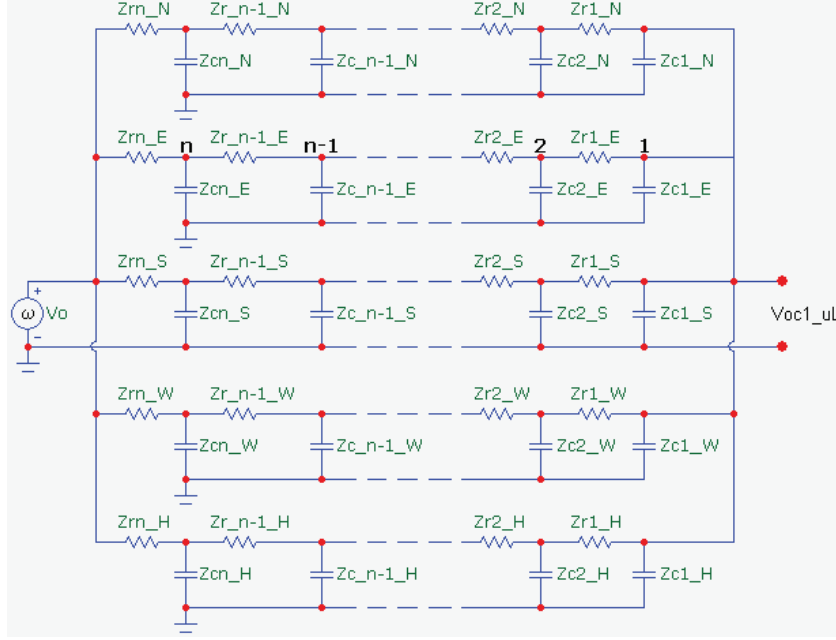
These 5 parallel RC ladders have equal input and output voltages: V_o and V_{oc1_uL}. The previous technique used to evaluate V_{oc1_L} of the lumped circuit is used to evaluate V_{oc1_uL}. Without loss of generality, the East ladder is used to generate equations similar to Eqns. 19-21, to formulate an expression for V_{oc1_uL}.

The correspondence between the values of the above East ladder components and those of the original unlumped circuit (Fig. 3) is:

$$Zc_{i\_E} = Zc\_E \qquad i = 1..n$$
$$Zr_{i\_E} = Zr\_E \qquad i = 1..n-1, \qquad\qquad Zr_{n\_E} = Zrso\_E + Zr\_E/2$$

An expression for V_{oc1_E} is formulated based on the following definitions:

z_{i_E}:   the total impedance from a node i to ground, when considering only Zc_{i_E} and the components to the right of node i.
Examples: $z_{1\_E} = Zc_{1\_E}$, $z_{2\_E} = Zc_{2\_E} // (Zr_{1\_E} + Zc_{1\_E})$

$$z_{1\_E} = Zc_{1\_E}$$
$$z_{i\_E} = Zc_{i\_E} // (Zr_{i\text{-}1\_E} + z_{i\text{-}1\_E}), \quad i = 2..n \tag{22}$$

V_{i_E} :   the voltage at node i, $i=1..n+1$. $V_{n+1\_E} = V_o$
H_{i_E}:   the voltage transfer function from node $i+1$ to i

$$H_{i\_E} = \frac{V_{i\_E}}{V_{i+1\_E}} = \frac{z_{i\_E}}{Zr_{i\_E} + z_{i\_E}} \quad , \quad V_{i\_E} = V_{i+1\_E} \cdot H_{i\_E} \tag{23}$$

$$V_{oc1\_uL} = V_{1\_E} = V_{2\_E} \cdot H_{1\_E} = V_{n+1\_E} \cdot H_{n\_E} \cdot H_{n-1\_E} \cdot \ldots \cdot H_{2\_E} \cdot H_{1\_E} = V_o \cdot \prod_{i=1}^{n} H_{i\_E} \tag{24}$$

117

3.2.3 Proof: V$_{oc1\_L}$ = V$_{oc1\_uL}$

By induction on the node number *(k)*, it is shown that voltage transfer functions at all nodes along the East ladder *(H$_{i\_E}$, i = 1..n)* are equal to the voltage transfer functions at corresponding nodes of the Lumped Circuit ladder *(H$_{i\_L}$)*:

$$z_{i\_E} = f_E^{-1} z_{i\_L} \quad \text{and} \quad H_{i\_E} = H_{i\_L} \qquad \text{for } i = 1..n \tag{25}$$

Proof: Assuming a static ladder size n, consider the voltage transfer function at node k of the East ladder.

Supporting Equations

$$k = 1: \quad z_{1\_E} = Zc_{1\_E} = f_E^{-1} Zc_{1\_L} = f_E^{-1} z_{1\_L} \qquad \text{(19), (18)}$$

$$H_{1\_E} = \frac{z_{1\_E}}{Zr_{1\_E} + z_{1\_E}} = \frac{f_E^{-1} z_{1\_L}}{f_E^{-1} Zr_{1\_L} + f_E^{-1} z_{1\_L}} = \frac{z_{1\_L}}{Zr_{1\_L} + z_{1\_L}} = H_{1\_L} \qquad \text{(23),(18),(20)}$$

Assume (25) is true for all nodes up to and including the kth node: $i = 1.. \, k, \; k < n$

Then

$$z_{k+1\_E} = Zc_{k+1\_E} \| (Zr_{k\_E} + z_{k\_L}) = f_E^{-1} Zc_{k+1\_L} \| (f_E^{-1} Zr_{k\_L} + f_E^{-1} z_{k\_L}) \qquad \text{(19), (18)}$$

$$= f_E^{-1} \left(Zc_{k+1\_L} \| (Zr_{k\_L} + z_{j\_L}) \right) = f_E^{-1} z_{k+1\_L} \qquad \text{Ladder Factoring, (19)}$$

and

$$H_{k+1\_E} = \frac{z_{k+1\_E}}{Zr_{k+1\_E} + z_{k+1\_E}} = \frac{f_E^{-1} z_{k+1\_L}}{f_E^{-1} Zr_{k+1\_L} + f_E^{-1} z_{k+1\_L}} = H_{k+1\_L} \qquad \text{(23), (18), (20)}$$

Therefore Eqn. 25 is true for $i = 1.. \, k+1, \; k < n$

Therefore Eqn. 25 is true for $i = 1..n$.

This argument can be applied to the components of the other ladder branches corresponding to the 4 orientations $\{ N, S, W, H \}$ producing the same result.

Finally, from Eqn. 21 we have:

$$V_{oc1\_uL} = V_o \cdot \prod_{i=1}^{n} H_{i\_E} = V_o \cdot \prod_{i=1}^{n} H_{i\_L} = V_{oc1\_L}$$

The open circuit voltage due to V_o of the lumped and unlumped circuits are equal.

3.2.4 V_{oc2_L} : Open circuit voltage due to I_L of the lumped circuit

The complete original lumped circuit is shown again below.
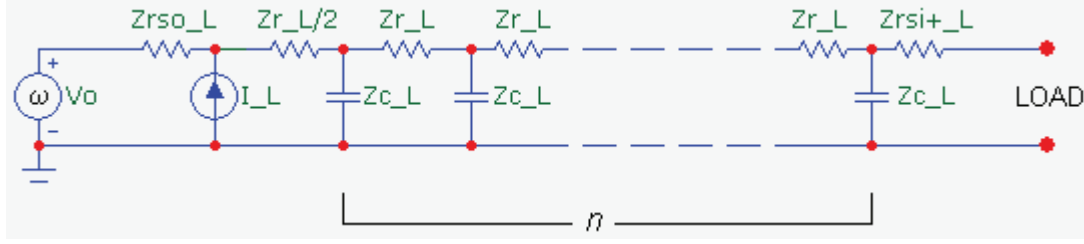
Figure 1: The Complete Lumped Circuit

V_o is shorted and V_{oc2_L}, the voltage across the right-most capacitor, Zc_{1_L} (below) is sought. Nodes are labelled $1..n+1$ and all impedances are relabelled with an index as shown in the circuit below:
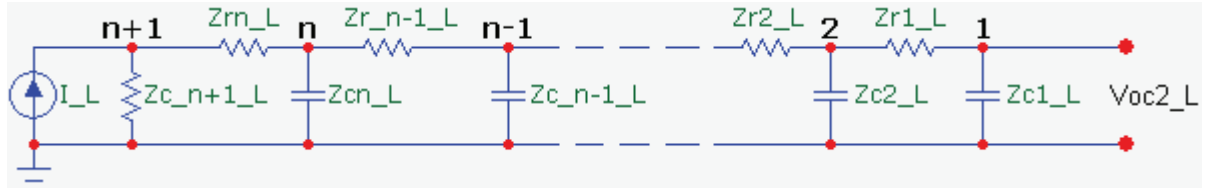

Figure 4: The Lumped Circuit with V_o Removed

The correspondence between this circuit component names of Fig. 4 and the original lumped circuit component names (Fig. 1) is:

$$Zc_{j\_L} = Zc\_L \quad j = 1..n, \qquad Zc_{n+1\_L} = Zrso\_L$$
$$Zr_{j\_L} = Zr\_L \quad j = 1..n-1, \qquad Zr_{n\_L} = Zr\_L/2$$

An expression for V_{oc2_L} is formulated based the following definitions:

z_{j_L}: total impedance from Zr_{j_L} to the right only, across open circuit terminals, $j = 1..n$

Examples: $z_{1\_L} = Zr_{1\_L} + Zc_{1\_L}, \; z_{2\_L} = Zr_{2\_L} + Zc_{2\_L}//(Zr_{1\_L} + Zc_{1\_L})$

$$z_{1\_L} = Zr_{1\_L} + Zc_{1\_L}$$
$$z_{j\_L} = Zr_{j\_L} + Zc_{j\_L}// z_{j-1\_L}, \qquad j = 2..n \tag{26}$$

I_j: the current entering node j from the left side of the node, $j = 1..n+1$
$$I_{n+1} = I_L$$

H_{j_L}: the current transfer function from node $j+1$ to node j, $j = 1..n$

$$H_{j\_L} = \frac{I_j}{I_{j+1}} = \frac{Zc_{j+1\_L}}{Zc_{j+1\_L} + z_{j\_L}}, \quad I_j = I_{j+1} \cdot H_{j\_L} \tag{27}$$

$$V_{oc2\_L} = I_1 \cdot Zc_{1\_L} = I_2 \cdot H_{1\_L} \cdot Zc_{1\_L} = I_3 \cdot H_{2\_L} \cdot H_{1\_L} \cdot Zc_{1\_L} \ldots = I_L \cdot H_{n\_L} \cdot H_{n-1\_L} \cdot \ldots \cdot H_{1\_L} \cdot Zc_{1\_L}$$

$$V_{oc2\_L} = I_L \times \prod_{j=1}^{n} H_{j\_L} \times Zc_{1\_L} \tag{28}$$

119

3.2.5 V$_{oc2\_uL}$: Open circuit voltage due to I$_X$ of the unlumped circuit

After shorting V_o, the unlumped circuit with 5 independent current sources becomes:
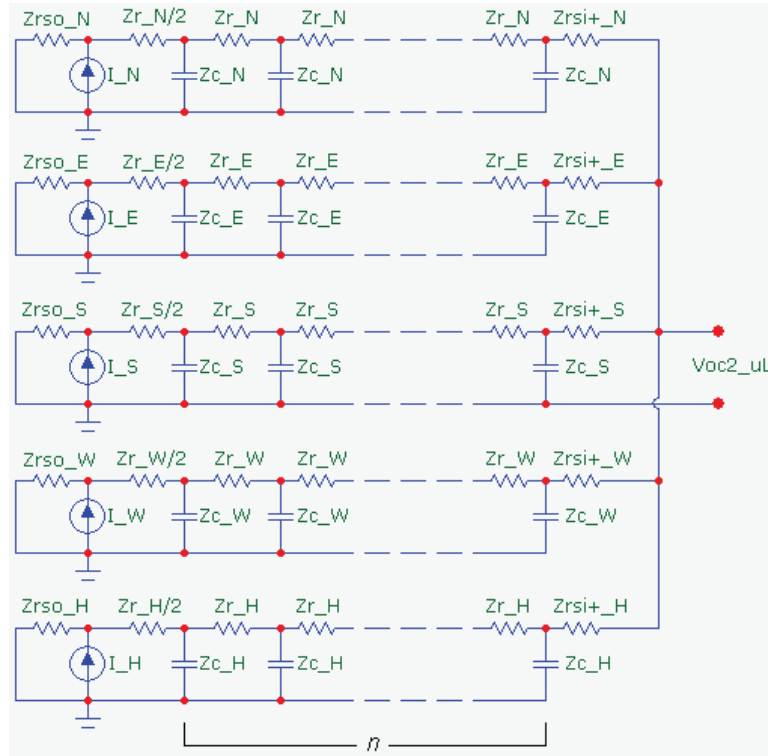
In order to determine V_{oc2_uL}, the contribution that each of the 5 current sources makes to V_{oc2_uL} is considered separately and these contributions are summed using the superposition principle. The technique for determining the contribution of each of the 5 current sources is identical and is presented here for I_N. The contribution that I_N makes to V_{oc2_uL}, is shown as V_{oc2_uLN}, in the circuit below. The 4 other current sources are removed.

120
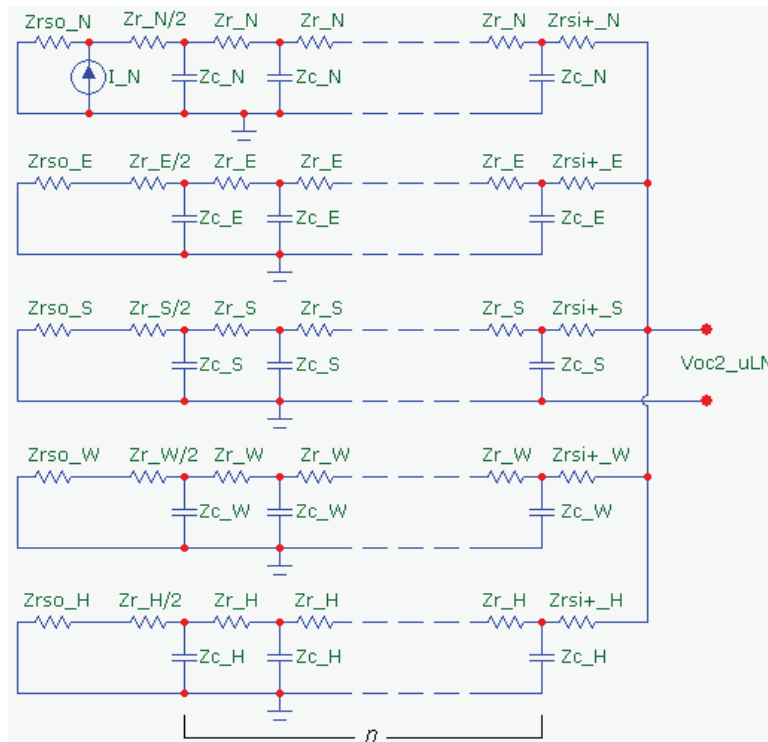
The circuit is first simplified by recognizing that V_{oc2_uLN} is the voltage across 5 impedance ladders in parallel. The lower 4 ladders contain the same sequence of impedance values of the lumped Thevenin impedance ladder (Fig. 2) but differing by the corresponding common multiple: f_E, f_S, f_W, f_H . Repeating the application of ladder factoring of section 3.1.2, the above circuit becomes:
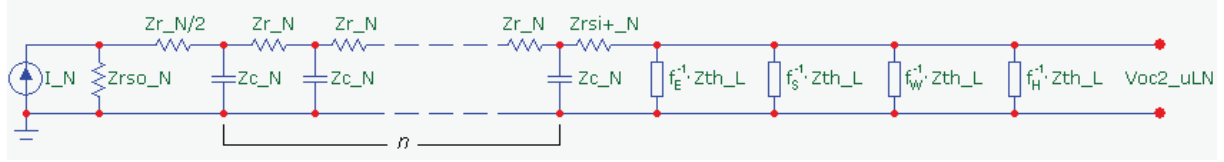
The 4 parallel impedances are reduced to a single impedance:

$$\frac{1}{(f_E + f_S + f_W + f_H)\dfrac{1}{Z_{Th\_L}}} = \frac{1}{(1-f_N)\dfrac{1}{Z_{Th\_L}}} = \frac{1}{(1-f_N)} Z_{Th\_L}$$
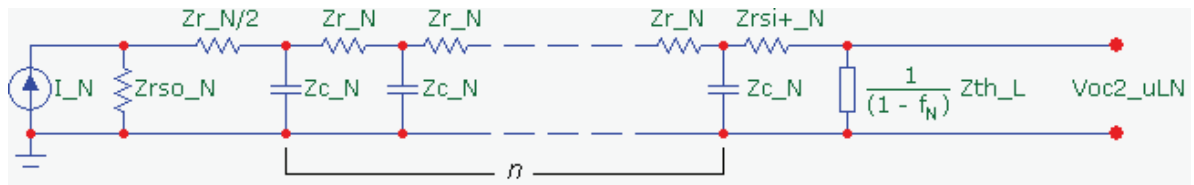
Figure 5: V_{oc2_uLN}, the contribution of the North current source to V_{oc2_uL}

This impedance is then treated as the load of the Thevenin equivalent circuit of the rest of the circuit and V_{oc2_uLN} is the voltage across this load. The Thevenin impedance (Z_{th_N}) is determined by removing the current source I_N and calculating the impedance between the Thevenin load terminals as shown below.
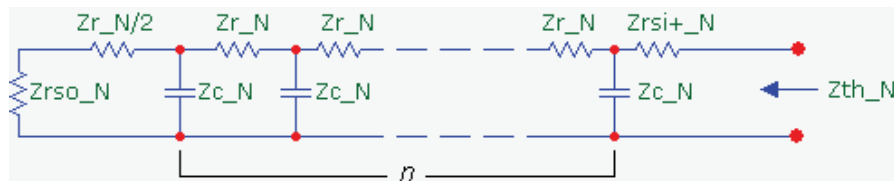
Again this contains the same sequence of impedance values of the lumped Thevenin impedance ladder (Fig. 2) but differing by the common multiple: f_N. Repeating the application of the ladder factoring of section 3.1.2 gives

$$Z_{th\_N} = f_N^{-1} \cdot Z_{th\_L}$$

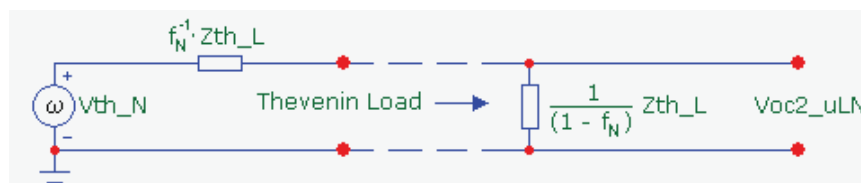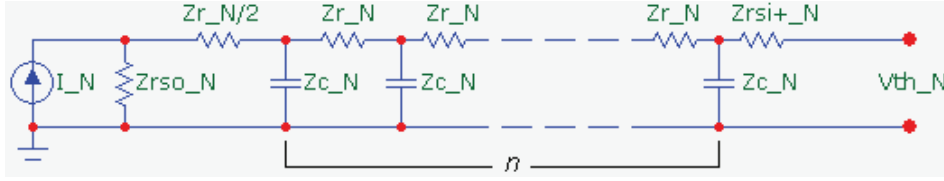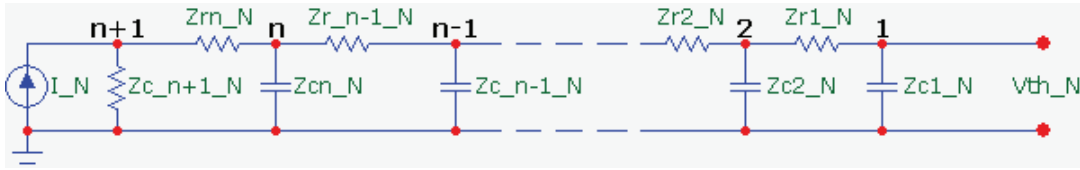and the Thevenin equivalent circuit of the I_N-based circuit (Fig. 5) is:

Figure 6: The Thevenin circuit and load used to calculate V_{oc2_uLN}.

121

To determine V_{th_N}, the open circuit voltage of the I_N-based circuit (Fig. 5) with no load is calculated:

The above circuit is relabelled in the same manner as the circuit of Fig. 4 in section 3.2.4.

The correspondence between the above circuit components and the original lumped circuit values is:

$$Zc_{j\_N} = Z_{c\_N} \qquad j = 1..n, \qquad Zc_{n+1\_N} = Zrso_N$$
$$Zr_{j\_N} = Z_{r\_N} \qquad j = 1..n-1, \qquad Zr_{n\_N} = Zr_N/2$$

An expression for V_{th_N} is formulated as in Eqns. 26-28, based on the following definitions:

z_{j_N}:   total impedance from Zr_{j_N} to the right only, across the open circuit terminals, $j = 1..n$

       Examples: $z_{1\_N} = Zr_{1\_N} + Zc_{1\_N}$, $z_{2\_N} = Zr_{2\_N} + Zc_{2\_N}//(Zr_{1\_N} + Zc_{1\_N})$

$$z_{1\_N} = Zr_{1\_N} + Zc_{1\_N}$$
$$z_{j\_N} = Zr_{j\_N} + (Zc_{j\_N} // z_{j-1\_N}), \quad j = 2..n \tag{29}$$

I_j: the current entering node j from the left side of the node, $j = 1..n+1$
$$I_{n+1} = I_N$$

H_{j_N}:   the current transfer function from node $j+1$ to node j, $j = 1..n$
$$H_{j\_N} = \frac{I_j}{I_{j+1}} = \frac{Zc_{j+1\_N}}{Zc_{j+1\_N} + z_{j\_N}}, \quad I_j = I_{j+1} \cdot H_{j\_N} \tag{30}$$

$$V_{th\_N} = I_1 \cdot Zc_{1\_N} = I_2 \cdot H_{1\_L} \cdot Zc_{1\_N} = I_3 \cdot H_{2\_N} \cdot H_{1\_N} \cdot Zc_{1\_N} = \ldots$$
$$= I_{n+1} \cdot H_{n\_L} \cdot H_{n-1\_N} \cdot \ldots \cdot H_{2\_N} \cdot H_{1\_N} \cdot Zc_{1\_N}$$

$$V_{th\_N} = I_N \times \prod_{j=1}^{n} H_{j\_N} \times Zc_{1\_N} \tag{31}$$

3.2.5.1 Proof: $H_{j\_N} = H_{j\_L}$

By induction on the node number *(k)*, it is shown that current transfer functions at all nodes along the North ladder $(H_{j\_N}, \ j = 1..n)$ are equal to the current transfer functions at corresponding nodes of the Lumped Circuit ladder (H_{j_L}):

$$z_{j\_N} = f_N^{-1} z_{j\_L} \quad \text{and} \quad H_{j\_N} = H_{j\_L} \qquad \text{for } j = 1..n \qquad (32)$$

Proof: Assume ladder size *n*, consider the current transfer function at node *k* of North ladder.

$$k = 1: \quad z_{1\_N} = Zr_{1\_N} + Zc_{1\_N} = f_N^{-1}(Zr_{1\_L} + Zc_{1\_L}) = f_N^{-1} z_{1\_L}$$

$$H_{1\_N} = \frac{I_1}{I_2} = \frac{Zc_{2\_N}}{Zc_{2\_N} + z_{1\_N}} = \frac{f_N^{-1} Zc_{2\_L}}{f_N^{-1}(Zc_{2\_L} + z_{1\_L})} = H_{1\_L}$$

Assume Eqn. 32 is true for all nodes up to and including the kth node: $j = 1.. \ k, \ k < n$

Then $\quad z_{k+1\_N} = Zr_{k+1\_N} + (Zc_{k+1\_N} \| z_{k\_N})$

$$= f_N^{-1} Zr_{k+1\_L} + \left(f_N^{-1} Zc_{k+1\_L} \| f_N^{-1} z_{k\_L} \right) = f_N^{-1} Zr_{k+1\_L} + f_N^{-1}\left(Zc_{k+1\_L} \| z_{k\_L} \right)$$

$$= f_N^{-1} z_{k+1\_L}$$

and $\quad H_{k+1\_N} = \dfrac{I_{k+1}}{I_{k+2}} = \dfrac{Zc_{k+2\_N}}{Zc_{k+2\_N} + z_{k+1\_N}} = \dfrac{f_N^{-1} Zc_{k+2\_L}}{f_N^{-1}(Zc_{k+2\_L} + z_{k+1\_L})} = H_{k+1\_L}$

Therefore Eqn. 32 is true for all nodes up to and including the $k+1^{st}$ node: $j = 1..k+1, \ k < n$
Therefore Eqn. 32 is true for $j = 1..n$.

As a result V_{th_N} from Eqn. 31 may be written as:

$$V_{th\_N} = I_N \times \prod_{j=1}^{n} H_{j\_L} \times Zc_{1\_N} = I_N \times \prod_{j=1}^{n} H_{j\_L} \times f_N^{-1} Zc_{1\_L} \qquad (33)$$

3.2.6 Calculating V_{oc2_uLN}

The contribution that I_N makes to V_{oc2_uL} can now be determined by the simple calculation of the voltage drop across the load of the Thevenin equivalent circuit of Fig. 5:
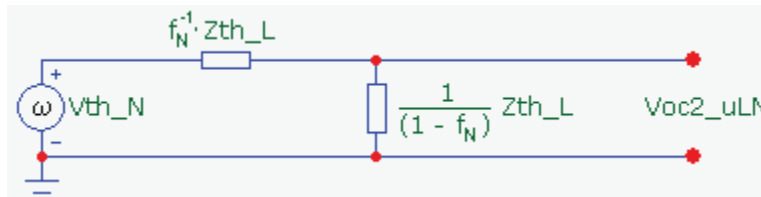
$$V_{oc2\_uLN} = V_{Vth\_N} \times \frac{\dfrac{1}{1-f_N} Z_{th\_L}}{\dfrac{1}{1-f_N} Z_{th\_L} + \dfrac{1}{f_N} Z_{th\_L}} = V_{Vth\_N} \times \frac{1}{1 + \dfrac{1-f_N}{f_N}} = V_{Vth\_N} \times f_N \qquad (34)$$

3.2.7 Calculating V_{oc2_uL}

The argument and circuit manipulations of the previous section can be applied to the each orientation to determine the contribution that I_X makes to V_{oc2_uL} for $X \in \{ N, E, S, W, H \}$. Using the principle of superposition, V_{oc2_uL} is then

$$V_{oc2\_uL} = V_{oc2\_uLN} + V_{oc2\_uLE} + V_{oc2\_uLS} + V_{oc2\_uLW} + V_{oc2\_uLH}$$

Apply Eqn. 34 to the open circuit voltage due to the current source at each orientation giving:

$$V_{oc2\_uL} = V_{Vth\_N} \cdot f_N + V_{Vth\_E} \cdot f_E + V_{Vth\_S} \cdot f_S + V_{Vth\_W} \cdot f_W + V_{Vth\_H} \cdot f_H$$

Substituting the corresponding expression for V_{th_X}, $X \in \{ N, E, S, W, H \}$ from Eqn. 33 gives

$$V_{oc2\_uL} = I_N \times \prod_{j=1}^{n} H_{j\_L} \times \frac{Zc_{1\_L}}{f_N} \cdot f_N \ + \ I_E \times \prod_{j=1}^{n} H_{j\_L} \times \frac{Zc_{1\_L}}{f_E} \cdot f_E \ +$$

$$I_S \times \prod_{j=1}^{n} H_{j\_L} \times \frac{Zc_{1\_L}}{f_S} \cdot f_S \ + \ I_W \times \prod_{j=1}^{n} H_{j\_L} \times \frac{Zc_{1\_L}}{f_W} \cdot f_W \ + \ I_H \times \prod_{j=1}^{n} H_{j\_L} \times \frac{Zc_{1\_L}}{f_H} \cdot f_H$$

$$V_{oc2\_uL} = \left(I_N + I_E + I_S + I_W + I_H \right) \times \prod_{j=1}^{n} H_{j\_L} \times Zc_{1\_L} \ = \ I_L \times \prod_{j=1}^{n} H_{j\_L} \times Zc_{1\_L} = V_{oc2\_L}$$

Therefore the open circuit voltage due to current sources of the lumped and unlumped circuits are equal.

4. Conclusion of the Equivalence Theorem

It has been shown that: $\quad Z_{th} \ = \ Z_{th\_L} \ = \ Z_{th\_uL}$

$V_{th} = V_{oc1} + V_{oc2} \qquad\qquad V_{oc1} \ = \ V_{oc1\_L} \ = \ V_{oc1\_uL} \qquad\qquad V_{oc2} \ = \ V_{oc2\_L} \ = \ V_{oc2\_uL}$

The Thevenin equivalent circuit of the lumped (Fig. 1) and unlumped (Fig. 3) circuits are found to be equal. The circuit and typical capacitive load modelling indoor air of a zone is shown below.
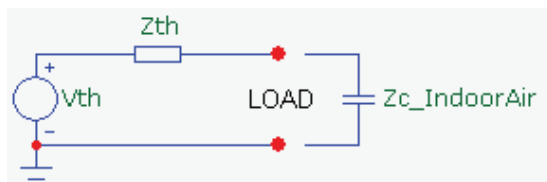
This proof shows that in the case of a single-zoned building with walls and ceiling/roof of equal construction, the inside air temperature response for the lumped and unlumped circuits are identical when the lumped irradiance data sequence and the lumped circuit are constructed according to the specifications of Eqns. 17 and 18.

If other wall-specific responses are required, such as the inner surface temperature response of the Eastern wall, for example, then the lumped circuit is not sufficient. In this case the unlumped circuit is required. Note that for this *specific* example a 3rd circuit is possible, consisting of the Eastern wall ladder circuit in parallel with a 2nd ladder circuit representing the lumping of the North, South, West and Horizontal orientations.
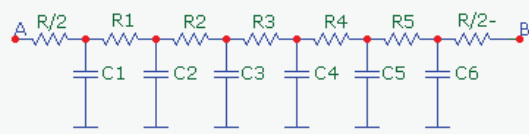
Appendix G   Circuit Model of the Light Weight House
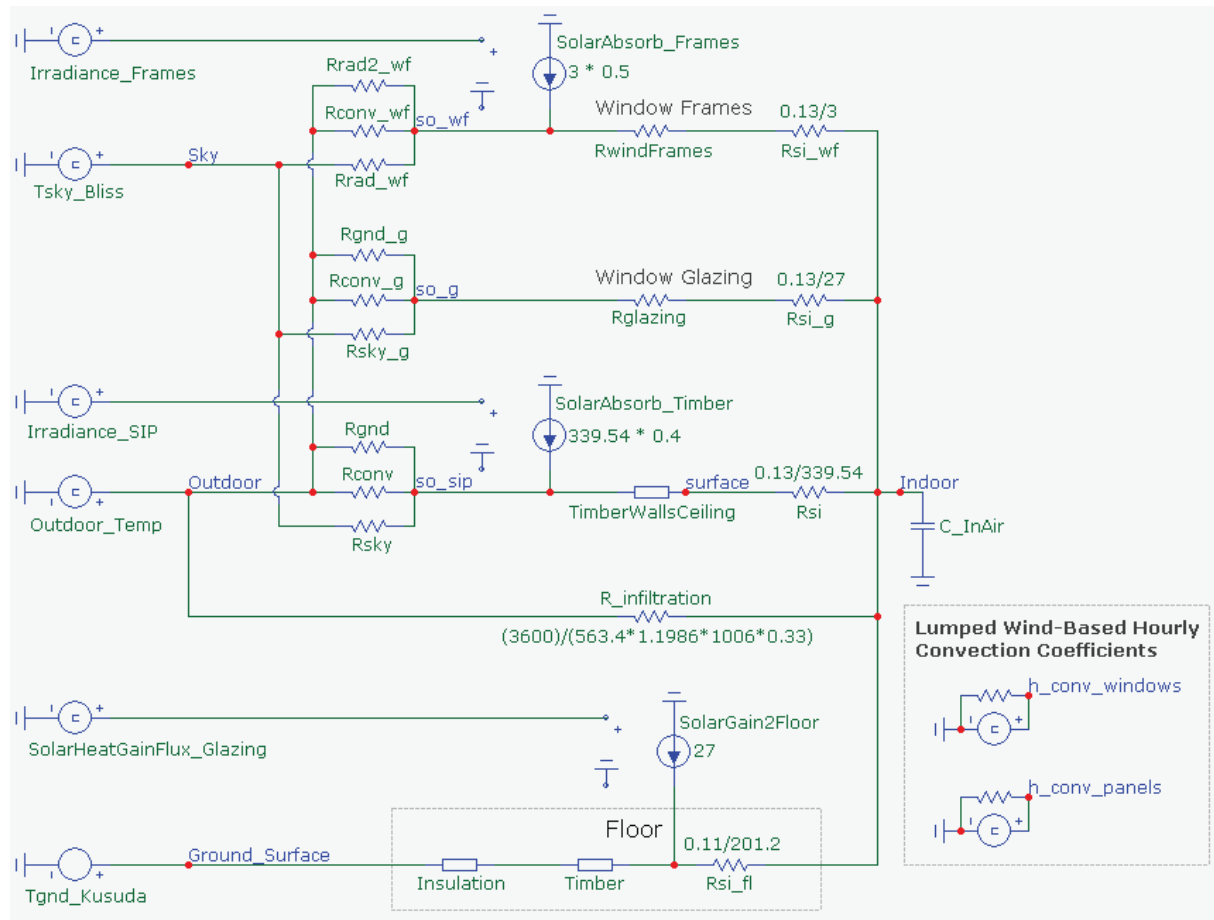
Macro Expansions:
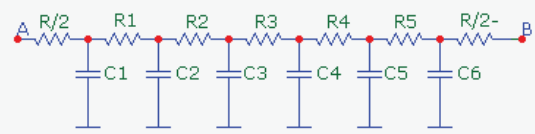
Appendix H   Derivation of $T_{in}(t)$ from Energy Balance Equation - Manual Model

From Chapter 6:

$$C_T dT_{in} = G_{incident} \cdot A_w \cdot SHGC \cdot dt + dQ_{heating} - dQ_{cooling} - \frac{(T_{in} - T_{out\_avg})}{R_T} dt \qquad (6.3)$$

With $G_{incident} \cdot A_w SHGC \cdot dt = dQ_{heating} = dQ_{cooling} = 0$, the above becomes

$$C_T dT_{in} = -\frac{(T_{in} - T_{out\_avg})dt}{R_T} \qquad \text{with } \tau = R_T C_T \text{ and rearranging:}$$

$$\frac{dT_{in}}{(T_{out\_avg} - T_{in})} = \frac{dt}{\tau} \qquad \text{integrating both sides:}$$

$$-\ln(T_{out\_avg} - T_{in}) = \frac{t}{\tau} + c \qquad c: \text{constant of integration,}$$

taking the exponential of both sides:

$$T_{out\_avg} - T_{in} = e^{-\frac{t}{\tau} + c} = ce^{-\frac{t}{\tau}}$$

$$T_{in} = T_{out\_avg} - ce^{-\frac{t}{\tau}} \qquad \text{solving for c by letting } T_{in}(0) = T_{in\_0}$$

$$c = T_{out\_avg} - T_{in\_0}$$

$$T_{in}(t) = T_{out\_avg} + (T_{in\_0} - T_{out\_avg})e^{-\frac{t}{\tau}}$$

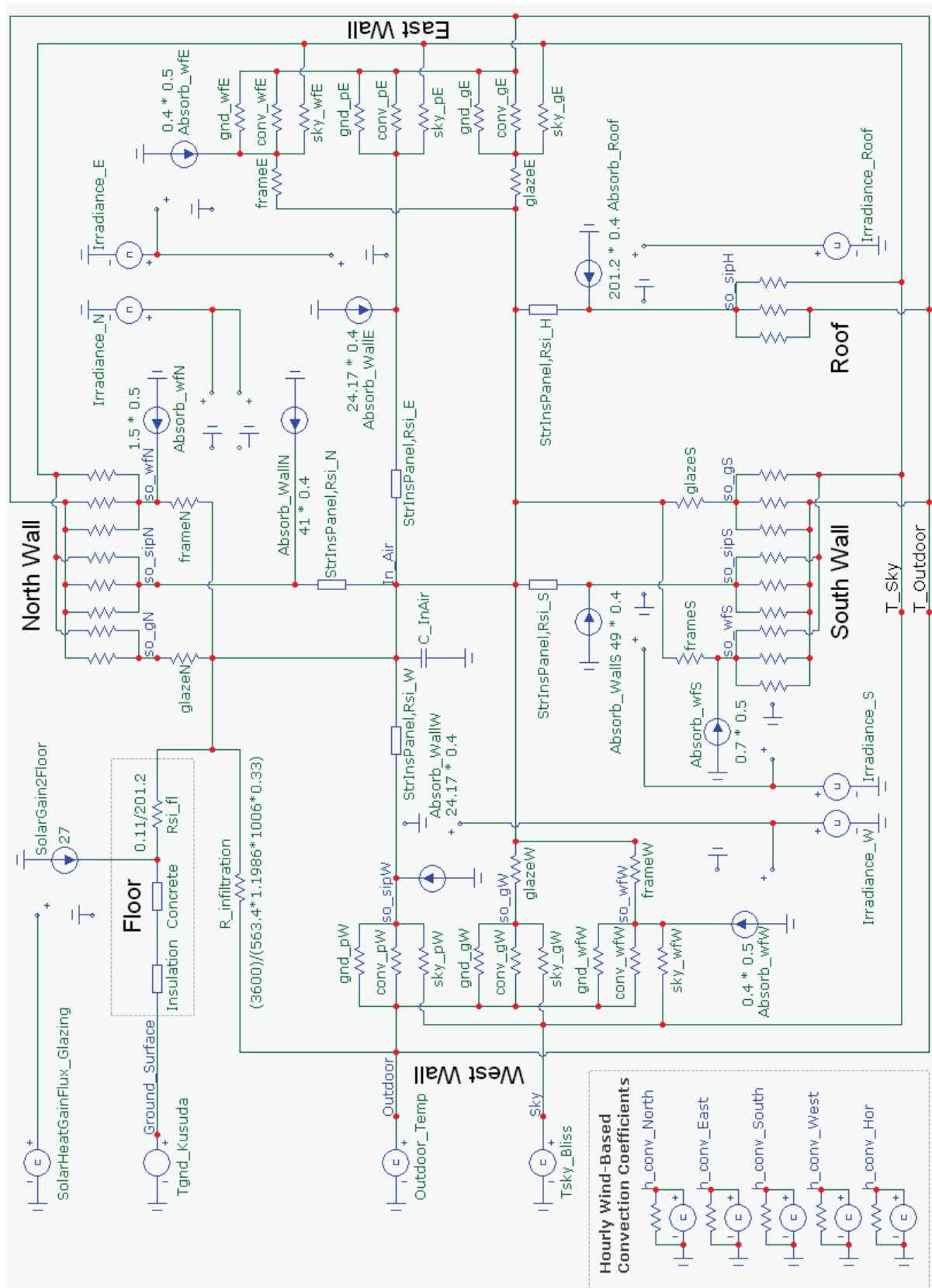# Appendix I The Unlumped Reference Circuit Model

Figure I.1: Reference Circuit Model of the Low Energy House With Solar Insolation Included; *Without Lumping*; Distributed Walls and Ceiling